VNIVERSITAT DE VALÈNCIA

DEPFET: A silicon pixel detector for future colliders. Fundamentals, characterization and performance

Carlos Manuel Mariñas Pardo April 2011

DEPFET: A silicon pixel detector for future colliders. Fundamentals, characterization and performance

Carlos Manuel Mariñas Pardo
Tesis Doctoral
April 2011

VNIVERSITAT DE VALÈNCIA

Facultat de Física
Departament de Física Atòmica, Molecular i Nuclear

DEPFET: A silicon pixel detector for future colliders. Fundamentals, characterization and performance.

Carlos Manuel Mariñas Pardo
Tesis Doctoral

2011

D. Carlos Lacasta Llácer,
Científico Titular del CSIC, y

D. Marcel André Vos
Investigador Ramón y Cajal

CERTIFICAN:

Que la presente memoria que tiene por título *DEPFET: A silicon pixel detector for future colliders. Fundamentals, characterization and performance*, ha sido realizada bajo su dirección en el Instituto de Física Corpuscular (Centro Mixto Universitat de València - CSIC) por D. Carlos Manuel Mariñas Pardo y constituye su trabajo de tesis doctoral en el Departament de Física Atòmica, Mol·lecular i Nuclear de la Universitat de València para optar al grado de Doctor en Física.

Y para que conste, en cumplimiento de la legislación vigente, firman el presente certificado en Burjassot a 1 de Abril de 2011.

Fdo. Carlos Lacasta Llácer

Fdo. Marcel André Vos

V^oB^o del tutor:
D. Emilio Higón Rodriguez

Contents

Introduction

High Energy Physics is one of the most successful branches of contemporary Physics. This field of Science has reached an unprecedented development over the last few decades. The discoveries made with the High Energy Physics experiments since the fifthties of the twentieth century, allowed us to stablish a model of the behaviour of the nature and their smallest constituents. This model is called the Standard Model (SM) and gives us a good description of the particles as well as the interactions between them. Nevertheles, the Standard Model is not a *Theory of Everything* because there are many aspects that this theory can not explain (quantum gravity, hierarchy problem, dark matter, neutrino masses, ...). The LHC (Large Hadron Collider) at CERN (Centre Européen de Physique Nucléaire), the biggest accelerator ever made, will explore during the next years the nature beyond the frontiers of the Standard Model an this machine must discover the only particle of this model undiscovered yet: the Higgs Boson. This particle, if discovered, will solve the problem of the mass generation of the fundamental particles. It is well established in the scientific community that the LHC will discover new non-standard physics (SUSY, Little Higgs, ...) but a lepton collider will be needed to refine the measurements and provide a better description of its properties (mass, couplings, spin,...). This will be the role of the new e^+e^- colliders, like ILC or CLIC, that will cover energies from 500 GeV up to 3 TeV in the center of mass frame. In the meanwhile, a complementary machine (SuperKEKB) will break the luminosity frontier at intermediate energies, to make new discoveries by collecting unprecedented statistics, pushing the limits stablished by the SM. A brief historical overwiew of the High Energy Physics from the early days to the present situation will be covered in chapter 1.

In order to extract all the information that the future colliders will provide, the different subdetectors must meet unprecedented requirements. Concerning the Vertex Detector, excellent vertex reconstruction is required as well as an efficient heavy quark flavour tagging using low momentum tracks. In order to cope with this heavy constraints, high granularity, fast read-out, low material budget and low power consumption are required in the Vertex Detectors. The ILC and SuperKEKB machines description and a brief introduction of the detector concepts (ILD and SiD for the ILC and Belle-II for SuperKEKB) will be covered in chapter 2.

The DEPFET (DEpleted P-channel Field Effect Transistor) active pixel detectors

are based in the integration of amplifying p-channel Field Effect Transistors (FET) into a fully depleted bulk. An aditional n-implant below the transistor's channel creates a minimum of potential (called the internal gate) and collects the electrons created in the substrate by the impinging particles. This technology merges the detection with the first amplification stage and is one of the principal candidates to meet the challenging requirements that the new colliders impose to the detectors. The most important aspects of the DEPFET technology as well as the description of the ILC module developed for testing the sensors will be covered in chapter 3.

In this thesis several aspects of the characterization of ILC DEPFET detector prototypes are covered as well, from individual sensors of two different generations PXD4 and PXD5 tested in lab (chapter 4) to a Telescope made of 5 planes of 128x64 pixels matrices with a device under test (chapter 5) tested on beam.

Finally, one of the best characteristics of the DEPFET technology was tested. One of the main features of this technology is the small amount of power dissipation, that allows to avoid cooling pipes all over the sensor. These thermal studies of a Belle-II PXD ladder are included in chapter 6.

Finally, there is a summary of all the results presented all over the chapters and the conclusions that one can extract using them.

Introducción

La Física de Altas Energías es una de las ramas más exitosas de la Física. Este campo de la Ciencia ha alcanzado un desarrollo sin precedentes a lo largo de las últimas décadas. Los descubrimientos realizados por los experimentos de la Física de Altas Energías desde los años cincuenta del siglo veinte, nos permiten establecer un modelo del comportamiento de la naturaleza y de sus elementos más fundamentales. Este modelo es el denominado Modelo Estándard (SM) y nos proporciona una buena descripción de las partículas así como de las interacciones entre ellas. No obstante, el Modelo Estándard no es una *Teoría del Todo* debido a que existen numerosos aspectos que esta teoría no puede explicar (gravedad cuántica, el problema de la jerarquía, materia oscura, las masas de los neutrinos, ...). El LHC (Gran Colisionador Hadrónico) del CERN (Centro Europeo de la Física de Partículas), el mayor acelerador jamás construído, explorará durante los próximos años la naturaleza más allá del Modelo Estándard y esta máquina deberá descubrir la única partícula predicha por este modelo y que no ha sido descubierta todavía: el Bosón de Higgs. Esta partícula, de ser descubierta, será la encargada de resolver el problema de la generación de la masa de las partículas fundamentales. Es un hecho reconocido por la comunidad científica que el LHC descubrirá nueva física no estándard (SUSY, Little Higgs, ...) pero será necesario un colisionador leptónico para refinar las medidas y proporcionar una mejor descripción de sus propiedades (masa, acoplamientos, espín, ...). Este será el papel de los nuevos colisionadores e^+e^-, como el ILC o CLIC, que cubrirán energías desde los 500 GeV hasta los 3 TeV en centro de masas. Mientras tanto, un acelerador complementario a estos (SuperKEKB) romperá la frontera de la luminosidad a energías intermedias, que permitirá hacer nuevos descubrimientos recolectando mucha estadística, nunca antes alcanzada, contrastando los límites establecidos en el SM. En el capítulo 1 se hará una breve descripción de la Historia de la Física de Altas Energías, desde sus inicios hasta el momento actual.

Para poder extraer toda la información que nos proporcionarán estos nuevos colisionadores, los diferentes subdetectores deberán cumplir con unos requisitos nunca antes alcanzados. Respecto al Detector de Vértices, se requiere una excelente reconstrucción de vértices así como una identificación eficiente de quarks de sabores pesados utilizando para ello trazas de bajo momento. Para poder hacer frente a estos exigentes requisitos, se requerirá que el Detector de Vértices tenga alta granularidad, rápida lectura, poco material y poca potencia disipada por el sensor. En

el capítulo 2 se cubrirá una descripción tanto del ILC como de SuperKEKB así como una rápida introducción de los conceptos de detectores (ILD y SiD para ILC y Belle-II para SuperKEKB) para dichas máquinas.

Los píxeles activos basados en la tecnología DEPFET (DEpleted P-channel Field Effect Transistor) se basan en la integración de un transistor de efecto campo (FET) con un canal tipo p en un sustrato totalmente desertizado. Un implante de tipo n adicional se sitúa bajo el canal del transistor creando un mínimo de potencial (denominado puerta interna) que recolecta los electrones que se crean en el sustrato debido a las partículas incidentes. Esta tecnología mezcla la detección de las partículas y una primera etapa de amplificación y es uno de los principales candidatos a satisfacer los exigentes requisitos que imponen los nuevos colisionadores sobre los detectores. En el capítulo 3 se tratarán los aspectos más importantes de esta tecnología, así como la descripción del sistema de pruebas desarrollado para estudiar las características de los detectores.

En esta tesis se tratan también diferentes aspectos de la caracterización de prototipos de detectores DEPFET para el ILC, desde sensores individuales de dos generaciones diferentes PXD4 y PXD5 testados en laboratorio (capítulo 4) hasta un Telescopio formado por 5 planos de matrices de 128x64 píxeles y un módulo bajo prueba (capítulo 5) caracterizadas en haz.

Finalmente se comprueba una de las mejores características que presenta el detector DEPFET. Uno de los principales rasgos de esta tecnología es la pequeña disipación de potencia, que permite el hecho de no incluir tuberías de refrigeración a lo largo del sensor. Estos estudios térmicos de un módulo del detector de vértices de Belle-II se incluyen en el capítulo 6.

Finalmente, se encuentra un resumen de los resultados presentados a lo largo de los anteriores capítulos y las conclusiones que se pueden extraer de los mismos.

Chapter 1

High Energy Physics historical overview

The history of physics is a long and involving tale, which will not be told here.

Physics is one of the basic branches of Science that started its development a long long time ago. The Ancient Greeks began the development of the basic principles of the modern science, establishing concepts like the conservation of matter, and trying to explain the World in terms of natural causes. They pursued the basic constituents of Nature, trying to find the fundamental blocks that our Universe is made of. Today, we know that there are elements more fundamental that the fire, air, earth and water that they thought, but the search is still open within the scientific community.

Since then, and during hundreds of years, the science passed through a dark period where no big discoveries appeared. This period finished when the revolutionary heliocentric cosmology was proposed by Copernicus, turning upside down the vision of the Universe the mankind had till then. Followed by Galileo Galilei (who established the basis of the modern experimental physics) and Kepler, this scientific revolution reached its splendor when Isaac Newton published the *Principia* [1]. The physics knowledge grew rapidly, and followed by the discoveries of Young, Faraday, Maxwell, Curie and Thompson (among many others), the twentieth century was reached with the idea that almost all the Universe was well understood.

At that time no one suspected that, following the theory raised by Planck five years before, Albert Einstein was about to propose in 1905 his theory of relativity, the biggest turn in our ideas of space and time since the Copernican revolution: the new modern view of the Universe, based on the quantum mechanics was about to start.

The race for understanding the nucleus and its constituents was unstoppable and very soon the proton, neutron, electron and photon were discovered and also

the interactions between them were established. Cosmic rays and radioactive sources were used as first 'microscopes' but was the development by Lawrence of the first accelerator in 1929, which boosted the appearance of new subatomic elements and this way, a new theory called Standard Model [2] [3] [4] was introduced to put some order in this zoo of particles and interactions.

The Standard Model is the most succesfull theory ever created in the history of the High Energy Physics field, and is the most succesfull attempt to create a single theory that could explain the rules of our Universe. The Standard Model describes the particle constituents of ordinary matter as well as three of the four known interactions that govern the Nature and explain the binding matter and how is it transformed. Despite this big success, the Standard Model includes a third component (beyond the particles and forces already mentioned) that has not been proven to exist, and that explain how the electroweak symmetry is broken and particles acquire mass, driven by the Higgs mechanism [5]. The solution to other central physics problems, like the unification of forces including gravity, the connection to cosmology, the imbalance between matter and antimatter in the Universe or the neutrino masses, are neither addressed by this theory.

Universal physics laws govern the World, but some of this principles manifest themselves only at scales of energy and time far beyond of our everyday direct experience. This is the reason why particle physicists, since that time, create experiments using bigger and bigger particle accelerators to transform matter into energy and vice-versa, trying to reveal the basic laws of the Universe. This knowledge allowed our civilization to achieve a level of development never seen in the Human history.

1.1 Physics motivation

The Standard Model is a theory that describes the known particles and three of the four fundamental interactions (apart from gravity). The predictions of this model were tested over the last decades, up to energies of a few hundreds of giga electron-volts (GeV). There are several questions that the Standard Model can not answer and, apart from the neutrino masses, hierarchy problem, gravitation, dark matter or the barion-antibarion asymmetry, one of the most important problems is that this model relies on the unique particle that has not been discovered yet, the Higgs boson. This particle is one of the main targets of the present (LHC [7]) and future colliders (ILC [9], CLIC [8] or SuperKEKB [10]) because if no Higgs boson is finally found or its properties are completely different to the ones predicted in the SM, the whole theory will need of deep revision.

In e^+e^- machines, the main production mechanisms [11] for the SM Higgs boson are the Higgs-strahlung and the WW fusion processes (Fig. 1.1 (a)). In the Higgs-strahlung, the recoiling Z is mono-energetic (and decays into leptons in a clean way) and by knowing the initial center of mass energy, the Higss mass can be extracted independently from its decay. If a Higgs boson is found in the LHC, apart from its mass, the ILC has to determine its properties like the production

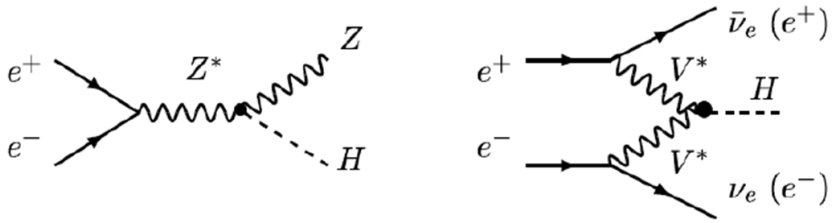

(a)

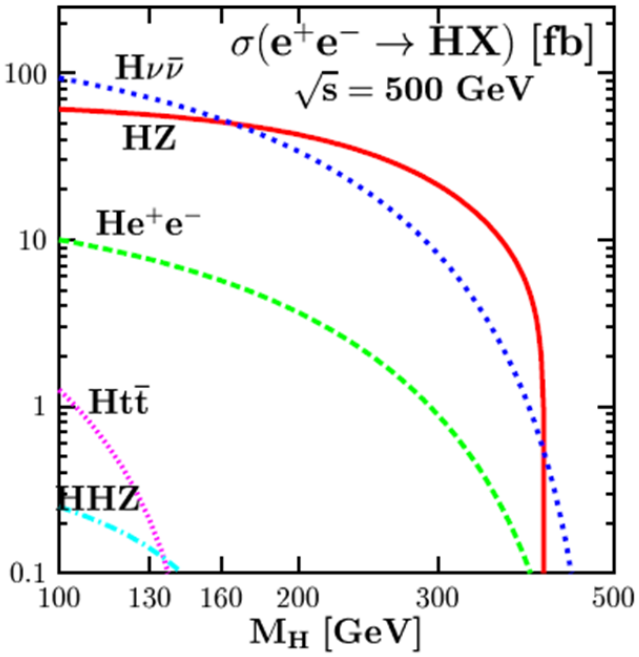

(b)

Figure 1.1: (*a*) *Feynman diagrams for the dominant Higgs production mechanisms at ILC, the Higgs-strahlung* ($e^+e^- \to ZH \to f\bar{f}H$) *and WW fusion* ($e^+e^- \to \overline{\nu_e}\nu_e H$). (*b*) *Production cross-section of the SM Higgs boson at the ILC as a function of the Higgs mass at the center of mass energy of 500 GeV.*

cross-sections, branching ratios, couplings and lifetime.

Even if the Higgs is not discovered in the LHC, a complete set of measurements could be done in an ILC machine with tunable energy from 90 GeV to 500 GeV, like top physics studies, electroweak precision measurements with a high luminosity Z-factory or (at least) partial SUSY [12] (an alternative scenario of the SM) particle spectrum [13].

Apart from the ILC, new physics could be detected through precision measurements of processes involving loop diagrams in the B Factories [14]. Rare decays, forbidden or suppressed in the SM, could receive contributions from new physics effects, revealing a new structure of the Nature. This machines running at intermediate energies, can not direct create Higgs bosons, but can study some of its properties indirectly using processes that could be Higgs mediated (Fig. 1.2), revealing new physics beyond the SM.

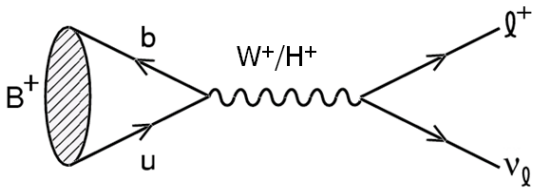

$$BR(B \to l\nu)_{SUSY} = BR(B \to l\nu)_{SM} \cdot \Theta(m_H^{-4})$$

Figure 1.2: *Example of a leptonic B decay with missing energy. This process can be Higgs mediated so, if the BR (Branching Ratio) measured is different of the predicted in the SM, new physics can be revealed (SUSY for example) and a level for the Higgs mass can be estimated.*

High precision CKM (Cabibbo Kobayashi Maskawa matrix) [15] [16] metrology doing as many measurements as possible or LFV (Lepton Flavour Violation) [17] studies, close a complete physics program to be done in the future B Factories.

To summarize, apart from the discoveries that the LHC will clearly do, a complementary counterpart machine will be needed not only to refine the measurements in these new physics processes but also to make high precision studies on the well established ones.

1.2 Particle accelerators

As already mentioned, the use of particle accelerators is essential in the investigation of Nature at its smallest scales. The first attempt to explore the structure of the atom was performed with alfa and beta particles from radioactive sources. Nevertheless, Rutherford discovered soon that the energy scale achievable with

this method was not high enough and urged the scientific community to invent a new accelerator mechanism. Then is when, Lawrence, based on the accelerating scheme proposed by Wideröe, invented the first cyclotron, that could accelerate hydrogen ions up to 80 keV. The importance of the energy can be explained by the de Broglie relation (Eq. 1.1) between the wavelength and the momentum of the particles. This way, the bigger the energy of the particle, the smaller the structures that can resolve.

$$\lambda = \frac{h}{p} \longleftrightarrow f = \frac{E}{h} \tag{1.1}$$

$$E = mc^2 \tag{1.2}$$

Using the famous Einstein's relation (Eq. 1.2), the mass can be transformed into energy and vice-versa, so the higher the energy, the heavier particles (hopefully new) could be produced in our accelerators and the better understanding of the inner structure of such particles can be achieved.

Because of this fact, during the last decades, the scientific community went through the energy frontier on every new collider, as can be seen in the Livingston plot (Fig. 1.3). Since the middle sixties of the last century, several high-energy colliders have been successfully operated on the different factories spread all over the World. Nowadays, the most powerful accelerator ever built by the mankind is called Large Hadron Collider (LHC) at CERN. This machine will accelerate two proton beams to an energy never achieved before of 7 TeV each, opening the study of the Terascale with a maximum center of mass energy of 14 TeV. This machine will provide collisions to the four main detectors placed over its circumference (ATLAS [18], CMS [19], LHCb [20] and ALICE [21]) and it is intended to address the fundamental questions that remain hidden to our scientific knowledge.

Despite the impressive performance of the LHC, the fact that this machine collides protons against protons, make its precision intrinsically limited due to several facts:

- Both, the initial state and the exact kinematics of each collision are unknown. The initial energy is shared between the partons inside the proton, so only a fraction of the center of mass energy of each beam is available for the collision.
- The signal to background ratio is very low and the background is completely dominated by QCD processes [22].
- In order to be able to distinguish the signals, a very clever trigger has to be designed, and therefore, rare processes that were not taken into account can be invisible to the detectors.

These disadvantages are not present in a lepton collider since this machine takes advantage of the point-like nature of the interacting particles. Thus, an

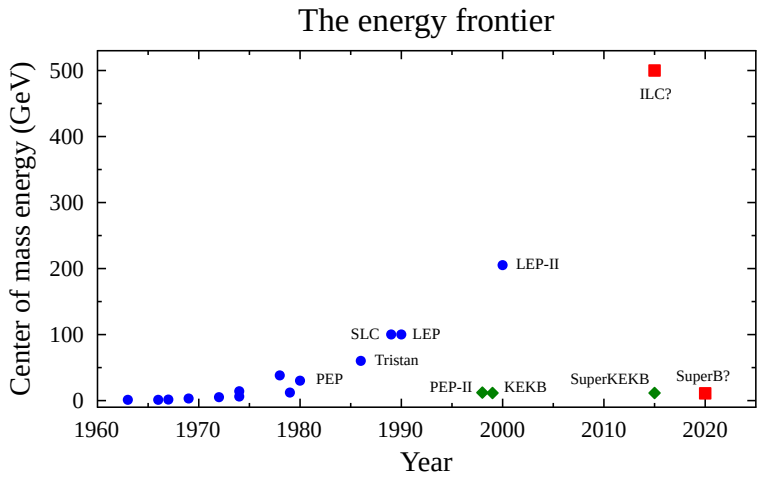

Figure 1.3: *The Livingston plot, showing the growth in the collider center of mass energy over the year of operation, for lepton colliders. The ILC (red square) aims the increase of the energy frontier by a factor two, while the B Factories (green diamonds) will increase not the energy, but the luminosity, in two orders of magnitude, trying to provide another roadway of discovery.*

experiment with moderate backgrounds (orders of magnitude lower than a hadron colliders), clean signals and a well-defined and tunable initial states (energy and polarization) can be built.

1.2.1 Linear colliders

Once that the needs of going for a lepton collider have been discussed, the particle physicist should think on the design of the new machine. It is natural to think that the way to go should be to continue towards an upgraded version (in luminosity and energy) of the old LEP (Large Electron Positron) [23] experiment, but there is one concept that will clarify that this circular machine is not an alternative: the synchrotron radiation.

The synchrotron radiation is the energy that a particle looses in the form of electromagnetic radiation when is accelerated on a circular path. The instantaneous synchrotron radiation power for one charged particle is shown in Eq. 1.3:

$$P = \frac{2}{3} \cdot \frac{1}{4\pi\epsilon_0} \cdot e^2 \cdot \frac{c \cdot \gamma^4}{\rho^2} \tag{1.3}$$

where

$\epsilon_0 = 8.85 \cdot 10^{-12}\ F \cdot m^{-1}$ is the permittivity of the free space

e is the electrical charge of the particle

$c = 3 \cdot 10^8 \ m \cdot s^{-1}$ is the speed of light

$\gamma = \frac{E}{m_0 c^2}$ is the relativistic factor

$\rho \sim \frac{m_0 c \gamma}{eB}$ is the radius of curvature of the particle in a magnetic field B

The energy loss per turn in a circular accelerator can be calculated:

$$\Delta E_{Syn} = P \frac{2\pi\rho}{c} = \frac{2}{3} \cdot \frac{e^2 c}{4\pi\epsilon_0} \cdot \frac{1}{(m_0 c^2)^4} \cdot \frac{E^4}{\rho^2} \tag{1.4}$$

As the energy loss is inversely proportional to the fourth power of the mass, while a proton ($m_{proton} \sim 1836 \cdot m_{electron}$) is almost not affected by this effect, an electron will loose a huge amount of energy in the shape of synchrotron radiation. This fact has to be seriously considered in the design of an electron machine, because this energy loss has to be compensated by the radio-frequency system (RF).

The equation that governs the energy loss per turn (Eq. 1.4) can be simplified for electrons (Eq. 1.5) and protons (Eq. 1.6) as follows:

$$\Delta E^{e^-}_{Syn} = 8.85 \cdot 10^{-2} \cdot \frac{E^4(GeV)}{\rho(km)} keV \tag{1.5}$$

$$\Delta E^{p}_{Syn} = 7.8 \cdot 10^{-3} \cdot \frac{E^4(TeV)}{\rho(km)} keV \tag{1.6}$$

Eq. 1.5 and 1.6 clearly show that the amount of radiation is directly proportional to the fourth power of the particle energy and inversely proportional to the bending radius. As an example, the LEP machine had a length of 26.65 km and while running at 104 GeV it lost around the 0.5% of the energy per turn, so the RF had to continually contribute with an extra energy of 0.4 GeV per turn to deliver the nominal center of mass energy.

The first stage of an accelerator like the ILC, assumes a center-of-mass energy of 500 GeV, so accelerating the electrons and positrons in a ring like LEP is unapproachable because of the looses. An hypothetical circular 'super-LEP' machine running at $\sqrt{s}$=500 GeV will loose several orders of magnitude more than the nominal LEP accelerator ($\Delta E^{super-LEP}_{Syn} \sim 525 \cdot \Delta E^{LEP}_{Syn}$), so the RF would have to replace the 216 GeV lost in the acceleration. The only way out could be the dramatic increase of the radius of the machine, but the cost of such a civil engineering could not be bearable.

Taking all of these elements into account, it is clear within the particle scientific community that the next collider has to be a linear electron-positron accelerator. At the present moment, the leading project that could cope with this requirements is the International Linear Collider (ILC).

Although is expected that the ILC will cover almost all the crucial energy regimes in the high energy physics field, one should not forget that discoveries at the LHC may also point to interesting processes in energies not reachable by this factory and, if so, new multi-TeV facilities (for example, 3 TeV in the case of CLIC) should take cover of the situation.

1.2.2 Super B Factories

The Higgs mechanism that gives mass to the particles is the central role of the energy frontier machines that were presented in the previous sections, but another type of machines reaching lower energies could help to test the SM by using high statistic studies (breaking the luminosity frontier): the Super B Factories.

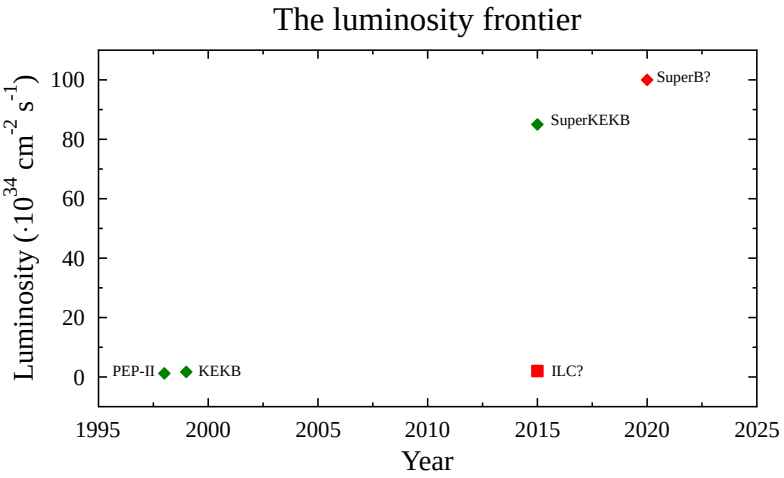

Figure 1.4: *Luminosity as a function of the year of operation for the present and future operational Super B factories. The ILC is also shown, to point out that an energy frontier machine can not compete with the flavour factories in the high luminosity field.*

The two most successful B Factories since the end of the last century were the KEKB collider for the Belle experiment [24] at KEK and the PEP-II collider for the BaBar experiment [25] at SLAC (Fig. 1.4). These asymmetric energy e^+e^- colliders did not try to discover new heavy elementary particles (like the LHC or ILC) but to study heavy flavour physics using high luminosity facilities. The discovery of the charm quark, the third family of quarks and leptons or the prediction of the top quark mass (before its measurement in Tevatron [26]) are examples of the utility of this machines.

The B Factories are high luminosity e^+e^- asymmetric colliders with a center of mass energy tuned ($\sim$10.58 GeV) to create $\Upsilon(4S)$, a $b\bar{b}$ bound state that decays to B meson pairs in a clean environment and with a high signal-to-background ratio:

$$BR(\Upsilon(4S) \longrightarrow B^+B^-) \sim BR(\Upsilon(4S) \longrightarrow B^0\overline{B^0}) \sim 0.5 \tag{1.7}$$

The beam energy asymmetry produces laboratory frame boost that allows the separation of the decays vertices of the two B mesons and the reconstruction of the decay vertices and time.

To continue with the study of this type of physics, larger amount of data is required and two new projects have arisen in the previous years: SuperB [27] in Italy and SuperKEKB in Japan. While the former is a completely new machine, the latter is an upgrade of the successful KEKB machine that will deliver a luminosity 40 times higher than the present factory, and that goes with an upgraded detector (Belle-II) with better performance and new sub-detectors. This new factory and the detector will be explained more in detail in the section 2.3.

As was already said, the center of mass energy ($\sqrt{s}$) is not the only important parameter in the performance of a collider. The second element, that defines the number of collisions per unit of time and area of the overlapping beams is the luminosity, defined in Eq. 1.8. To make precision studies of the physics processes, a large number of events are needed (large statistics), and the luminosity should be as high as possible in order to obtain these events in the shorter time.

$$\mathcal{L} = fk\frac{N_1 N_2}{4\pi\sigma_x\sigma_y}R \tag{1.8}$$

where

f is the repetition rate, i.e. the frequency at which the particles collide

k is the number of colliding bunches. The particles are collected in packets called bunches. Several bunches form a train.

N_1,N_2 are the number of particles on each of the two colliding bunches.

σ_x,σ_y define the beam cross-section at the interaction point (IP). Indicate the widths of the colliding bunches in horizontal and vertical directions, respectively.

R is the enhancement factor (pinch effect) and takes into account the mutual beam-beam interaction. Each bunch is affected by the collective magnetic field created by the other. This way, in a collision between an electron and a positron, they attract each other because of the opposite charge (see Fig. 2.3), resulting in an enhancement of the luminosity. Conversely, the collision between e^- and e^-, will drop the luminosity because of the repulsion between the particles. On the other hand, this deflection in the trajectory of the electrons (or positrons) will cause them to radiate photons (this process is called beamstrahlung, see Sec. 2.1.1) that will increase the background in the detectors. So the balance between the background produced and the beam size has to be optimized.

From Eq. 1.8, in order to enhance the luminosity, the beams have to be squeezed (reducing the transverse sizes) and the number of bunches have to be increased.

Chapter 2

The DEPFET projects: ILC and SuperKEKB

Every event at a lepton collider is physics; every event at a hadron collider is background.

S. Ting

The DEPFET Collaboration, established more than eight years ago, pursues the research and development (R&D) of its high resolution pixel sensors in many scientific fields. Although this technology is being developed also for applications like X-ray astronomy [28] or biomedical radiography [29], in this thesis only the use of these sensors as vertex detectors in future e^+e^- colliders will be treated. As a result of its unique characteristics, this technology is one of the principal candidates to meet the challenging requirements that the ILC vertex detector imposes and, indeed, will be used in the new Belle-II detector.

2.1 The International Linear Collider (ILC)

A linear collider is, in fact, two linear accelerators facing each other. The particles are accelerated following a straight path on each machine and then head on smashed in the center, where the detector is placed, to reveal what happened in the collision. Because of this configuration, a linear collider is a single-pass machine (the particles have to be accelerated in one go), and the accelerating cavities have to cope with very high gradients and to be extremely efficient. The International Linear Collider (ILC) (Figure 2.1) is based on 1.3 GHz superconducting radio-frequency (RF) accelerating cavities working at 2 K, with an average accelerating gradient of 31.5 MV/m to achieve a center of mass energy of 500 GeV/c (increaseable to 1 TeV/c in a second phase). These RF cavities have a low power loss and a high wall-plug to beam transfer efficiency, allowing high power and small emittance beams to achieve a peak luminosity of $2 \cdot 10^{34}$ cm^{-2}s^{-1}.

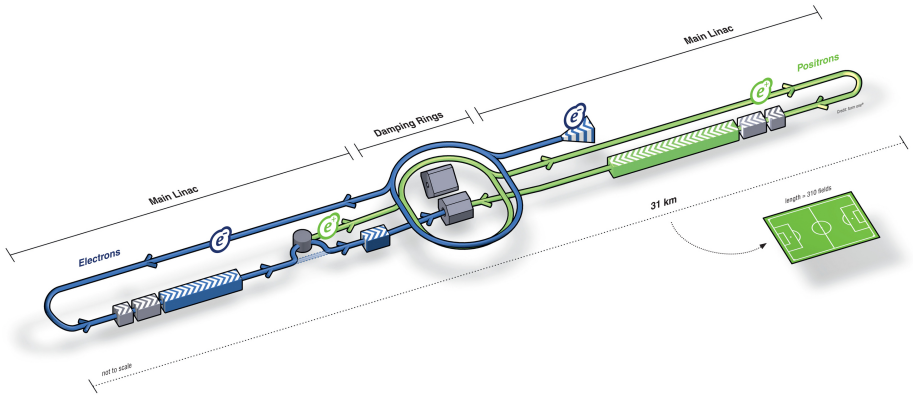

Figure 2.1: *A schematic layout of the ILC accelerator complex. A total length of 31 km (with two linear accelerators of 11 km that facing each other) is expected for a center of mass energy of 500 GeV.*

The particles extracted from the electron source are pre-accelerated in the 5 GeV/c damping rings (with a circumference of 6.7 km) placed in the center of the complex (Fig. 2.1). Then the beams are injected on the main linacs (11 km each), before entering the beam delivery system (4.5 km), which focus the two beams to the Interaction Point (IP), where they collide. The nominal energy for the first accelerator stage is 500 GeV/c, but the machine can be upgraded in a second stage up to 1 TeV/c if needed, just by extending another 11 km each linac (complemented with another modest modifications).

The beam has the structure shown in Fig. 2.2. With a repetition rate of 5 Hz, a bunch train of 1 ms containing 2820 bunches of 337 ns is sent each 200 ms.

This beam structure, as the incoming sections will point out, has major impact in the design of the different subsystems, specially the Vertex Detector. In order to be able to clearly reconstruct the events, the optimal situation would be to read the hole detector every bunch crossing (*time stamping*), but nowadays none of the pixel technologies in the market are able to perform the readout in 337 ns or just identify the time stamping of each bunch crossing (BX). Another approach to reduce the detector occupancy is the *time slicing* within bunch trains; in this case, not a single bunch crossing is read but several belonging to the same train are integrated. As an example, it was demonstrated that, although an overlap of physics events with background will occur, a high granular vertex detector like DEPFET could reconstruct events after the integration of 140 BX [30], together using the information provided by the outer and faster (but with worse spatial resolution) subsystems of the detector.

In the table 2.1, for comparison, the main beam parameters are shown for the ILC and CLIC machines. It is clearly visible that CLIC is much more challenging

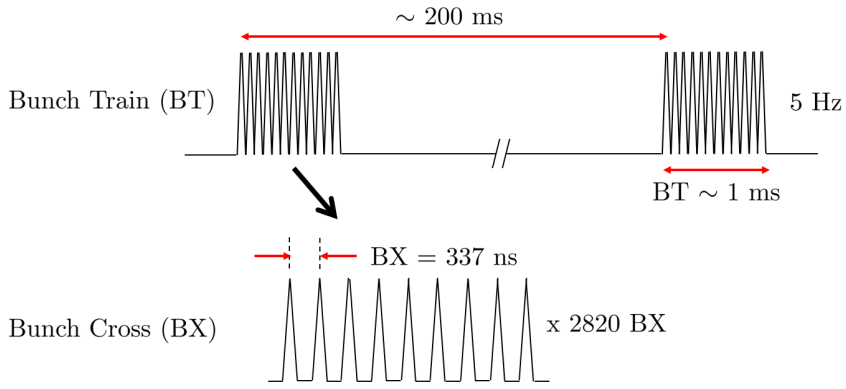

Figure 2.2: *ILC beam structure. A train of 1ms long is sent each 200 ms; this way the duty cycle is 0.5%*

than the ILC not only from the machine, but also from the detector point of view (the detectors designed for the latter can not be directly used in the former proyect). Although this proyect can take advantage of the studies performed by the ILC community, some aspects have to be specifically adapted to such concept.

Beam parameters	ILC (500 GeV/c)	CLIC (3 TeV/c)
Electrons/bunch ($\cdot 10^{10}$)	0.75	0.37
Bunches/train	2820	312
Train Repetition Rate (Hz)	5	50
Bunch separation (ns)	337	0.5
Train length (μs)	950	0.156
Horizontal IP beam size (nm)	655	45
Vertical IP beam size (nm)	6	0.9
Luminosity ($\cdot 10^{34}$ cm^{-2}s^{-1})	2	6

Table 2.1: *Comparison between the nominal ILC and CLIC beams. It is clearly visible that CLIC is not just a minor upgrade of the ILC accelerator, but a step forward in the technology. To achieve the required luminosity tiny beams have to collide, resulting in a big technological challenge.*

This general time structure has also good consequences for pulsed electronics. Because of the detector has to be built with the lowest material budget possible to reduce the multiple Coulomb scattering (as will be explained in the following sections), no active cooling is allowed inside the acceptance region; thus, the cooling system relies on forced cold air, and the detector can be switched on, only during

the necessary time for the readout, using the long time between trains to power it of and cool it down in the meanwhile.

2.1.1 Beam-beam interaction background

The luminosity (Eq 1.8), introduced in the Section 1.2, can be writen as (Eq. 2.1):

$$\mathcal{L} = fk\frac{N_1 N_2}{4\pi\sigma_x\sigma_y}R \propto \frac{P_{beam}}{E_{cm}}\sqrt{\frac{\delta_{BS}}{\epsilon_y}}R \tag{2.1}$$

where

$P_{beam} = \frac{E_{cm}}{2} \cdot fk \cdot N_{bunch}$ is the beam power, proportional to the RF power.

ϵ_y is the vertical emittance, related to the vertical beam size.

δ_{BS} is the beamstrahlung term, defined in Eq. 2.2 and represents the most important source of unwanted machine-induced background.

As discussed in a previous section (Sec. 1.2.1), in order to have a high luminosity, a high frequency and a high number of bunches, together with reduced beam sizes, is needed.

When the two beams approach each other, the individual particles feel the collective electromagnetic field of the incoming bunch, and this way its trajectory is disrupted towards the center of the opposite. Although the pinch effect is appreciated because of the increased luminosity (by reducing the beam sizes in an e^+e^- collider), this bent trajectory will cause the particles to radiate energy in the shape of beamstrahlung, a process like the synchrotron radiation (Fig. 2.3).

The energy loss through beamstrahlung (described in Eq. 2.2) is constrained to a 2-5% [31] but causes serious problems to the physics studies that require the precise determination of the initial conditions, like the center-of-mass energy.

$$\delta_{BS} \approx 0.86\frac{er_0^3}{2m_0c^2}\frac{E_{cm}}{\sigma_z}\left(\frac{N_{bunch}}{\sigma_x+\sigma_y}\right)^2 \tag{2.2}$$

Small beam sizes induce the increase of the beamstrahlung, resulting in energy spread and degraded luminosity spectrum. In addition, the radiated photons (about 2.5 photons per bunch particle with an average photon energy of 2.2 GeV/c [32]) not only hit the detectors directly but also can create electron-positron pairs in the vicinity of the interaction point, being the main background source. A rough estimation assumes that 144000 e^+e^- pairs/BX will reach the innermost layer of the Vertex Detector, placed at a radius of 15 mm and with a magnetic field of 4 T.

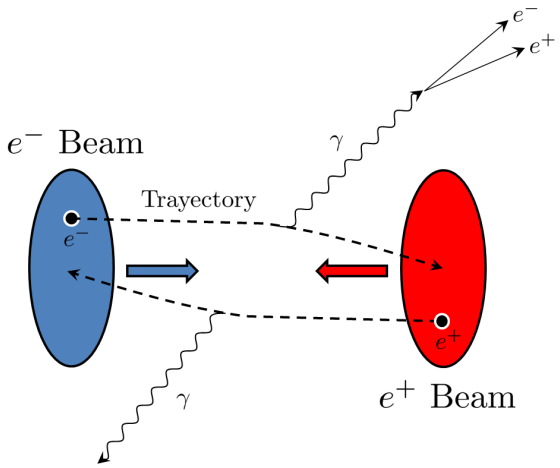

Figure 2.3: *Schematic view of beamstrahlung process. The particles in one bunch are attracted to the center of the opposite incoming one, radiating photons that can convert into electron-positron pairs. This effect represents the main background source expected in the Vertex Detector.*

2.2 The ILC detector concepts

On the ILC design, a single IP (Interaction Point) to be shared by two detectors in a push-pull arrangement, and a dual tunnel configuration for safety is assumed. This way, the detectors will be moved on and off the beam-line several times per year (time-sharing the luminosity), allowing the access to the detector out of the beam to be repaired, if needed. This pull-push configuration was adopted to reduce the costs of the project, because the interaction region is one of the most expensive parts of the accelerator. Because of this configuration, two detectors, based on complementary technologies are being developed: ILD (International Large Detector) [33] and SiD (Silicon Detector) [34] will guarantee that the discoveries make by one of then can be confirmed by the other. Fig. 2.4 shows the two detector prototypes. Both detectors are designed with a common structure: The innermost system is the vertex detector, close to the interaction point, to measure the displaced vertices of the long lived heavy flavour particles and to help in the track reconstruction. Then a tracker (gaseous TPC for ILD and all-Silicon for SiD), to reconstruct the tracks of the particles and measure their momentum. Outside the tracker, the electromagnetic and hadronic calorimeters, whose main task is to measure the energy of, primarily, photons and electrons and neutral hadrons, respectively. Both concepts are also equipped with complementary systems like a muon detector and a forward system of tracking and calorimetry.

The ILC detector concepts work under the assumption that the Particle Flow Algorithm (PFA) [35] will be used to reconstruct every particle in a complicated

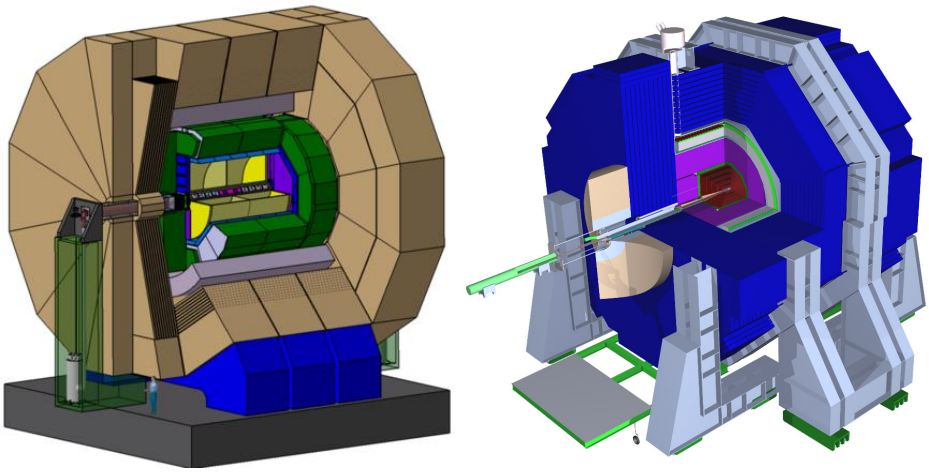

Figure 2.4: *ILD (left) and SiD (right), the two detector prototypes for the future ILC.*

final state (multi jets) and an intense background. The PFA involves the identification of clusters in the calorimeter and the association of these clusters to charged tracks in the tracker. For this purpose, highly efficient and hermetic tracker together with a precise vertex and a high granular calorimeter are needed. The goal is to build detectors with the following resolutions:

- Precise vertexing: $\sigma_{IP} \sim 5\ \mu m$
- Precise tracking: $\delta(\frac{1}{p}) \leq 5 \cdot 10^{-5}(GeV^{-1} \cdot c)$
- High jet energy resolution: $\frac{\Delta E}{E} \leq \frac{30\%}{\sqrt{E(GeV)}}$

The main difference between the two concepts is the choice of the tracker system. The momentum precision is given by the Eq. 2.3:

$$C_{Tracking} = \frac{\sigma_{point}}{0.3 \cdot B(\Delta R)^2}\sqrt{\frac{720}{N+4}} \tag{2.3}$$

where

σ_{point} is the single point resolution of the individual track hit

B is the magnetic field

$\Delta R = R_{Outer} - R_{Inner}$ is the difference between the outer and inner radii of the tracker, respectively

N are the number of measurement points

The tracking system depends strongly on the chosen detector architecture. The SiD concept relies on a 'small' tracker ($\Delta R = 100\ cm$), based on 5 planes ($N = 5$) of silicon microstrips ($\sigma_{point} \sim 14\ \mu m$ if $Pitch = 50\ \mu m$) and a strong magnetic field ($B = 5\ T$). On the other hand, the ILD concept decided to go to a 'large' ($\Delta R = 167\ cm$) Time Projection Chamber (TPC) with a weaker magnetic field ($B = 3.5\ T$). In this case, the worse single point resolution ($\sigma_{point} \sim 100\ \mu m$) is compensated by the continuous tracking ($N = 200$), achieving this way a very similar momentum resolution in both cases:

$$C^{SiD}_{Tracking} = 8.5 \cdot 10^{-5}\ GeV^{-1} \cdot c \tag{2.4}$$

$$C^{ILD}_{Tracking} = 6.4 \cdot 10^{-5}\ GeV^{-1} \cdot c \tag{2.5}$$

To have an idea of how challenging an ILC detector is, the calorimeter granularity has to be a factor 200 better than the LHC detectors (the avant-garde detectors ever made), the tracking resolution a factor 3 better than CMS, the pixel size in the Vertex Detector has to be a factor 20 smaller, and the material budget reduced a factor 10 in the central part and a factor more than 100 in the forward region.

2.2.1 Vertexing system requirements

The Vertex Detector is the innermost system in a particle physics detector. The primary goal of this sub-detector is to detect and measure the displaced vertices of long-lived heavy flavoured quarks inside jets (Fig. 2.5). A typical event that this sub-detector has to reconstruct are the two vertices that appear when a B meson decays into a D meson and thus, the innermost layer has to be as close as possible to the interaction point ($\sim 14\ mm$) together with a small beam pipe radius. If the inner layer can not be close enough to the interaction point, the multiple scattering will degrade the association of tracks to vertices, and hence the physics performance. The typical occupancy in the ILC Vertex Detector will be $\sim 0.04\ hits/mm^2/BX$ (r=15 mm; B=4 T), and to keep it reasonable low to be able to reconstruct tracks in such environment, a small pixel size together with a fast readout (even higher because of the incredibly high number of channels) is needed. The maximum number of bunch crossings that allows the perfect reconstruction of the events is 140 BX (reading out the full train, will produce $\sim 85\ hits/mm^2/BT$, shooting up the occupancy up to intolerable levels), so the full detector has to be read 20 times per bunch train.

The impact parameter precision is defined in Eq. 2.6:

$$\sigma_{IP} = a \oplus \frac{b}{p \sin^{\frac{3}{2}}(\theta)} \tag{2.6}$$

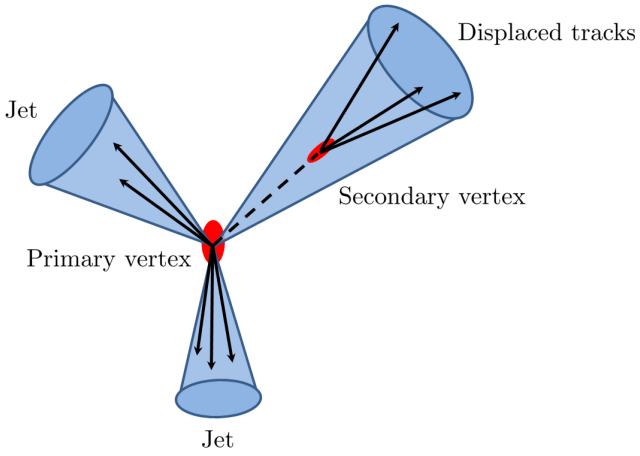

Figure 2.5: *Using the precise track reconstruction of the vertex detector, it is possible to identify jets arising from the b-quark hadronization by reconstructing the decay vertex of long-lived B hadrons within the jet. The decay of a long-lived hadron produces several charged particles coming out from a secondary vertex, displaced from the primary interaction point.*

where a is the single point resolution of the detector and b is the multiple-scattering term. In Table 2.2 both parameters a and b are shown for LEP, LHC and ILC, pointing out the challenging requirements that the ILC detectors have to cope with.

For a system of two detection layers at distances r_1 and r_2 from the interaction point and with intrinsic spatial resolution σ, the first term in Eq. 2.6 can be expressed as:

$$a^2 = \left(\frac{\sigma \cdot r_2}{r_2 - r_1}\right)^2 + \left(\frac{\sigma \cdot r_1}{r_2 - r_1}\right)^2 \tag{2.7}$$

The precision on the impact parameter is optimized by making detectors with a very high spatial resolution; in addition, the first measurement has to be made as close as possible to the interaction point (and thus, small pixels are needed to be able to resolve tracks in such a dense environment), the lever arm $(r_2 - r_1)$ has to be as large as possible and the material budget (multiple-scattering), inversely, reduced to the minimum (including the beam pipe). The inner radius is limited by the beam pipe and at high luminosities the radiation damage is a serious concern, which tends to drive the inner layer to larger radii.

According to what was stated, the baseline requirements for the Vertex Detector of the ILC concepts, independently of the final technology chosen, are:

- almost a full angular coverage ($\cos(\theta)$=0.96)

	a (μm)	b ($\mu m \cdot GeV \cdot c^{-1}$)
LEP	25	70
LHC	12	70
ILC	5	10
SuperKEKB	8.5	9.6

Table 2.2: *Comparison of the a and b parameters for the LEP, LHC, ILC and SuperKEKB vertex detectors. In LEP and LHC, the precision of the impact parameter is clearly dominated by the multiple-scattering term. In the new generation of lepton colliders (like the ILC or SuperKEKB detectors), the b term has to be dramatically reduced.*

- low material budget ($\leq 0.1\% X_0 \sim 100\ \mu m$ of Silicon, per layer) to minimize the multiple Coulomb scattering
- high granularity for good jet separation (pixel pitch $\sim 20 \cdot 20\ \mu m^2$)
- good spatial resolution ($\sigma_{IP} \leq 5(\mu m) \oplus \frac{10(\mu m \cdot GeV \cdot c^{-1})}{p \sin^{\frac{3}{2}}(\theta)}$) and fast readout ($\sim 50\ \mu s$ for the hole detector)
- low mass support structure (if needed)
- low power dissipation to avoid extra material in the shape of active cooling ($\sim 10\ W$)
- radiation hardness ($\leq 100\ krad/year$)

2.3 The SuperKEKB Factory

The SuperKEKB factory will be made up of the upgraded KEKB accelerator and the Belle-II detector. Both elements will be placed at the KEK high energy research facility in Tsukuba, Japan. The KEKB accelerator complex is a double ring collider (3 km in diameter) of e^+e^- beams with asymmetric energies of 4 GeV/c (LER, Low Energy Ring) and 7 GeV/c (HER, High Energy Ring), respectively (Fig. 2.6). As was already said, this Super B Factory is a precission machine, so the proposed upgrade of the current KEKB accelerator intends to increase the luminosity up to $8 \cdot 10^{35}$ cm^{-2}s^{-1}, a factor 40 times greater than the current luminosity of the machine, by squeezing the beams (the so called nano-beam option) and increasing moderately the beam currents (See Table 2.3).

The factory accelerates and collides particles at a center-of-mass energy of 10.58 GeV, which corresponds to the mass peak of the $\Upsilon(4S)$ resonance, that due to the energy asymmetry between the electrons and the positrons, is produced with a Lorentz boost. This resonance has a mass that is just above threshold to produce $B\overline{B}$ pairs and, indeed, decays in this way more than 96% of time.

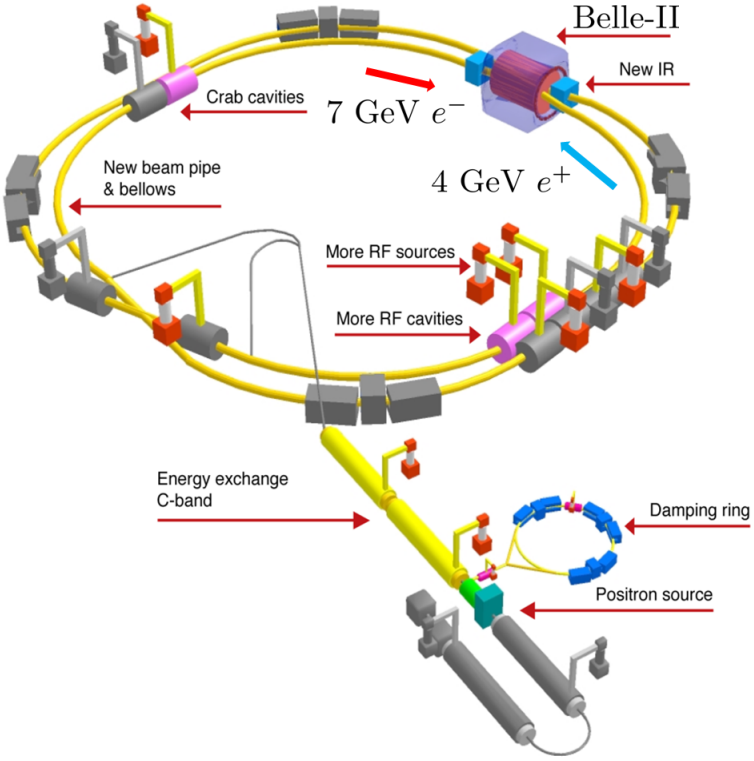

Figure 2.6: *Schematic layout of the SuperKEKB Factory. The 7 GeV/c electrons collide against the 4 GeV/c positrons in the interaction point, where the detector is settled. The upgraded Belle-II detector will be placed in the same place as the old Belle. Some parts of the accelerator will be replaced to achieve the higher luminosity.*

With these conditions an enormous number of B-mesons are created in a clean environment, allowing us to study the CKM matrix elements or the CP violation of the B system in the Standard Model (SM).

Historically, the Japanese Factory competed with the BaBar detector in the PEP-II accelerator at SLAC in USA. The next generation of high-luminosity B factories are in progress; the new SuperKEKB Factory will be finished by the end of 2013 while the SuperB Italian concept has prepared its Conceptual Design Report recently. T. Maskawa and M. Kobayashi were awarded in 2008 with the Nobel Prize for their theory of the CP violation, pointing out the importance of these studies.

2.3.1 Belle-II

Belle-II [36] is an upgrade of the old Belle detector that collected data corresponding to an integrated luminosity of 1000 fb^{-1} since 1999 to November 2009.

	KEKB		**SuperKEKB**		
	LER	HER	LER	HER	
Beam Energy	3.5	8.0	4.0	7.0	GeV/c
Circumference	3016.26		3016.26		m
RF frequency	508.887		508.887		MHz
Vertical beam size at IP	1.9		0.06		μm
Horizontal beam size at IP	80.0		32	25	μm
Beam Current	2.6	1.1	3.6	2.6	A
Number of bunches	5000		2503		
Luminosity	$2 \cdot 10^{34}$		$8 \cdot 10^{35}$		$\mathrm{cm}^{-2}\mathrm{s}^{-1}$

Table 2.3: *Comparison between the beam parameters of the HER and LER for the old (KEKB) and new accelerator (SuperKEKB). By decreasing the beam size at the interaction point and increasing the beam current, a factor 40 more will be achieved in the luminosity of the new machine.*

The main goal is to maintain the performance of the old Belle detector, but since increasing the luminosity translates into more signals but also higher radiation doses, the detector has to be fitted-out. Although no major changes are expected, fast electronics and radiation hardness are the key features of the new design.

The Belle detector is a general purpose 4π hermetic detector around the interaction point. As can be seen in Fig. 2.7, it is made of several sub-detectors in the central and forward-backward regions. From inside out, the detector consists of a pixel detector (PXD), a silicon vertex detector (SVD), the central drift chamber (CDC), a RICH detector, a particle identification detector (PID, Particle ID), called TOP in the central and ARICH in the forward region, an electromagnetic calorimeter (ECL) and the K_L and muon detector (KLM). The detector is complemented by a super conducting coil which provides a 1.5 T magnetic field.

The new PXD detector that replaces two layers of the old SVD detector will be the innermost subsystem and together with the new SVD, that will extend to larger radius than in Belle and will have a new readout chip (with a faster readout time and shorter shaping time), a better vertex resolution will be achieved. The CDC will also extend to bigger radius and together with smaller drift cells than in the previous version, will provide a better tracking performance. The new PID systems, being more compact and with very fast readout electronics, will provide good separation between pions and kaons. The electromagnetic calorimeter will be equipped with new electronics (faster and radiation hard) that will reduce the noise pile up. Finally, the data acquisition system (DAQ) has to be updated to manage the increased number of event rates and data volume.

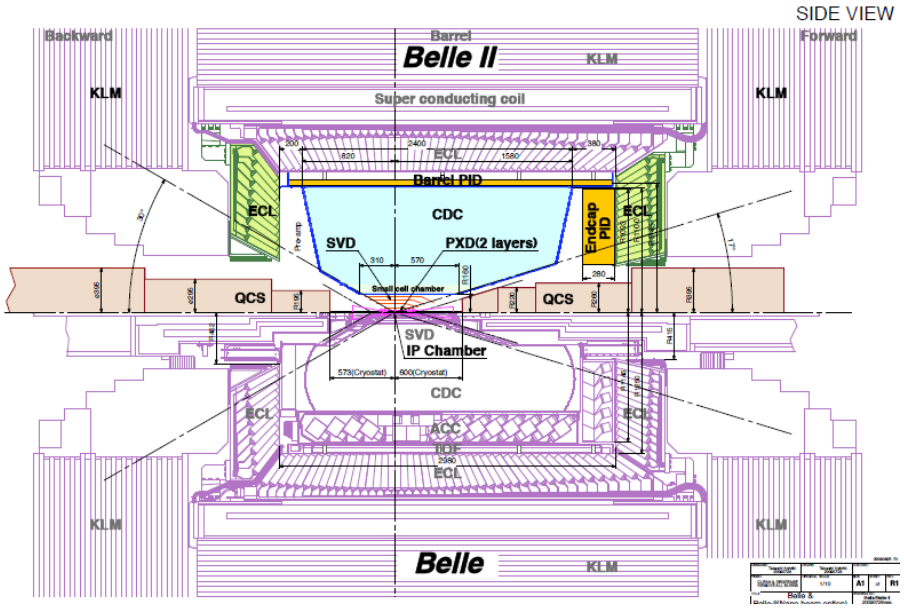

Figure 2.7: *A side schematic view of the old Belle detector (lower part) and the new Belle-II (upper part). Because of the higher energy of the electrons compared with the positrons, the detector is asymmetric. The main difference between the old and the new design is the pixel detector (based in the DEPFET technology), close to the beam pipe.*

Chapter 3

The DEPFET system

Will work if you collect holes, not electrons!

Old comments about the SLC detector. Book of appointments C. Damerell.

There are several technologies available in the market to be used as a vertex detector in the ILC detector concepts, like ISIS [37], MAPS [58] or DEPFET [39]. The DEPFET (DEpleted P-channel Field Effect Transistor) technology was invented by Kemmer and Lutz in the 80's and, because of its detection and amplification properties jointly, is one of the strongest candidates to be used not only in the vertex detectors of the future high energy physics experiments (like the ILC), but indeed is the baseline technology to be used in SuperKEKB, the Japanese B Flavour Factory.

3.1 DEPFET pixel sensors

The DEPFET principle is shown in Figure 3.1. Each pixel consists of a p-channel field effect transistor (FET) integrated on a completely depleted bulk. The substrate is a high resistivity n-type silicon with a p^+ backside contact. By means of side-wards depletion [40] (Figure 3.2), a minimum of potential for majority carriers (electrons in the case of n-type silicon) is created close to the front side, at around $\sim 1\ \mu m$ below it. An additional deep n-doping implantation under each transistor's gate creates a local minimum of potential even closer to the top surface (creating a region called *internal gate*) and achieves the lateral separation between adjacent pixels. An ionizing particle impinging the detector creates electron-hole pairs in the depleted substrate; while the holes drift to the backside (the most negative node), the electrons are driven to the minimum of potential at the internal gate.

The internal gate is capacitive coupled to the transistor's channel, so the signal collected there, will increase the drain current proportionally to the number of

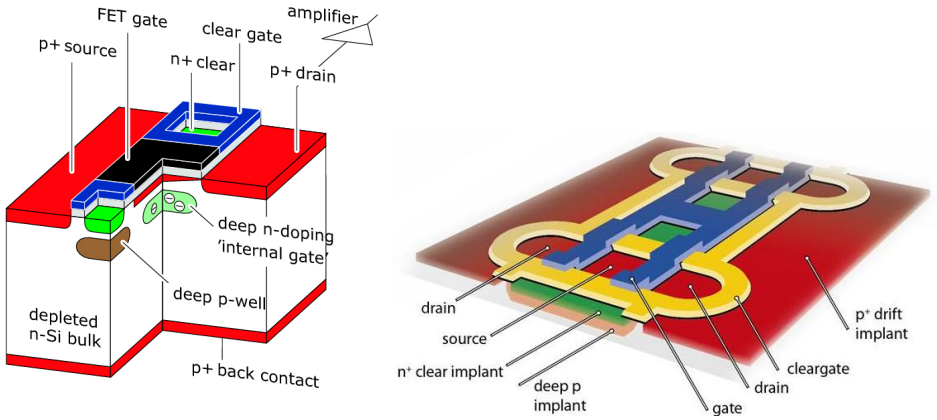

Figure 3.1: *Schematic view of a DEPFET pixel structure. The potential minimum is locally confined to the internal gate region, where the electrons are collected.*

electrons collected. The ratio between the charge (∂Q_{int}) collected in the internal gate and the transistor's current (∂I_{ds}) is the internal amplification of the system, (g_q factor), see Eq. 3.1.

$$g_q = \frac{\partial I_{ds}}{\partial Q_{int}} \propto \frac{g_m}{C_{ox}} \tag{3.1}$$

The internal gain is proportional to the transistor transconductance ($g_m = \frac{\partial I_{ds}}{\partial V_{gs}}$, directly related to the FET's performance) and inversely proportional to the capacity of the internal gate (C_{ox}). The g_q can be expressed also as a function of the geometrical characteristics of the transistor and the drain-source transistor current (Eq. 3.2):

$$g_q = \frac{\partial I_{ds}}{\partial Q_{int}} = \frac{1}{W^{\frac{1}{2}} \cdot L^{\frac{3}{2}}} \cdot I_{ds}^{\frac{1}{2}} \tag{3.2}$$

The internal gain of the system can be raised just by increasing the current or decreasing the width of the transistor (W), although the most effective way is by reducing the gate length (L) as much as possible. In the latest DEPFET productions, the very low capacitance of the internal gate (that transforms into low noise) together with an in situ amplification, lead to the fabrication of sensors with $g_q \sim 400\ pA/e^-$ with $L = 6\ \mu m$ [41].

The accumulated charge in the internal gate, produced by both signal and thermally generated electrons in the substrate (leakage current), can screen the internal gate potential, resulting in an insensitive detector. To avoid this effect, the electrons can be removed by applying a positive voltage pulse to a *clear* contact, placed in the periphery of each pixel. The potential barrier between the clear contact and the internal gate is modulated with an additional implant, called

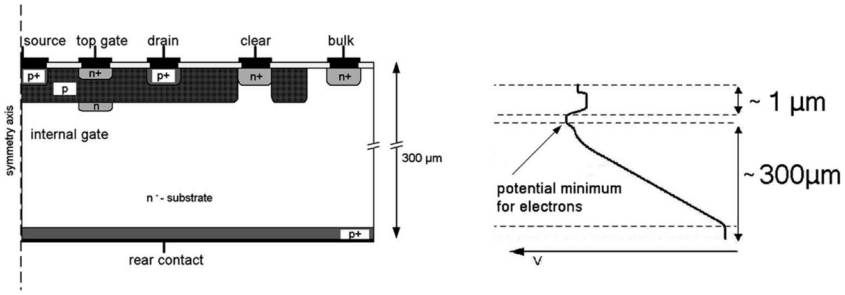

Figure 3.2: (*a*) *Cross section of a DEPFET pixel and* (*b*) *the potential distribution between the top and bottom layers as a function of the depth. This potential distribution, typical in DEPFET, is achieved by joining the side-wards depletion principle with an integrated transistor.*

cleargate. With this configuration, different clear operation modes are possible, as will be explained in Subsection 3.2.1.

3.2 DEPFET sensor operation

The operation mode of a DEPFET matrix (a certain amount of pixels operated together and arranged in a rectangular shape) is the row wise readout or rolling shutter. As shown in Figure 3.3 (*a*), all the pixels laying on the same row have the gates and clear contacts connected to the steering chips (Switchers), while the ones belonging to the same column, have the drains linked up to the readout chip. The source and cleargate contacts are all connected along the matrix.

To read the system starting from the sensor completely in off state, first one pixel row is powered on by applying a voltage to the external gate, provided by the gate switcher. Due to the correlated double sampling (CDS) readout scheme (Figure 3.3 (*b*)), a first measurement of the drain current is taken. This first current is the sum of the signal electrons created by the impinging particles in the detector and the leakage current. Then, a positive voltage is applied to the clear contact, to remove the charge accumulated in the internal gate. After the clear, the pixels are read once again and this second measurement is the pedestal current, coming only from the thermally generated electrons. Subtracting both measurements (Eq. 3.3), the result is the current of the charge produced just by the particles passing through the detector. After the second sample, all the transistors of the row can be powered off (even in this state they are able to collect signal) and the procedure is repeated on the next row.

$$I_{Signal} = I_{Signal+Pedestal} - I_{Pedestal} \tag{3.3}$$

In applications where high speed is needed (like the Belle-II detector), the CDS readout scheme is abandoned for a single sampling with pedestal subtraction

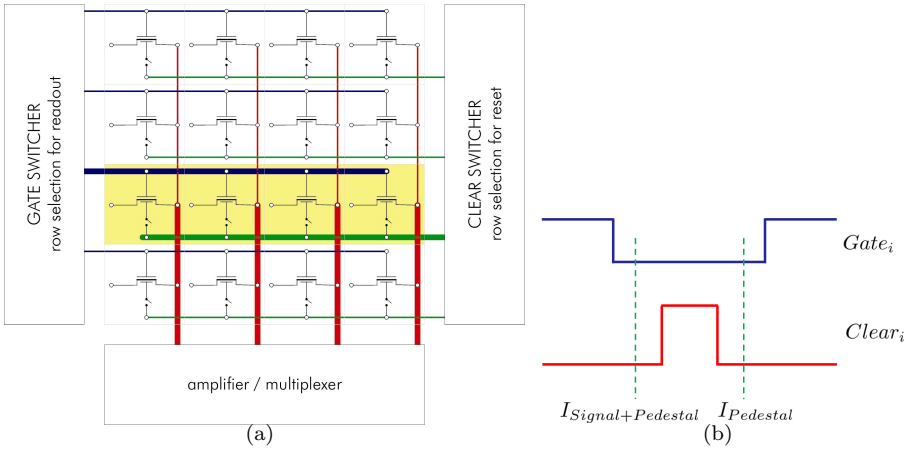

Figure 3.3: (*a*) *The DEPFET operation mode is row wise readout. The switchers (gate and clear) can gate or clear the pixels row by row, while each path of the the readout chip can acquire the drain currents of the pixels laying on the same column.* (*b*) *Correlated Double Sample (CDS) readout scheme. To samples are taken before and after the clear and by subtracting these two quantities, the signal deposited by the impinging particle can be extracted. This scheme can be modified to a single sampling (with pedestal correction afterwards) if high speed is needed.*

afterwards, much more favorable in terms of speed. In CDS scheme, is important to have a complete clear of the device, in order to subtract the real pedestals and not extra charges that remained in the internal gate due to an incomplete clear and that could be considered as leakage current. In case of a single sampling, is important to be sure that the matrix has a constant pedestals over the time, otherwise the signal calculated can be higher or lower of the real deposited in the detector by the particles.

3.2.1 Clear operation

One of the factors that determine the performance of a DEPFET sensor is the clear process [42] and is one of the most crucial aspects of the pixel design. The charges collected in the internal gate, produced by the impinging particles and the leackage current have to be removed periodically. If this does not happen, the accumulated charge make the internal gate less attractive for the signal electrons and even if the amount of collected charge is high enough, the internal gate can be also saturated. The clear process has to be done in a fast and complete way. The clearing process is actually the main stopper of the matrix readout speed and if the clear is not performed completely, the remain charges can contribute to increase the noise levels of the system (Fig. 3.4 (*b*)). The clear process starts when a positive voltage is applied to the clear contact, in the periphery of the pixel. The charges accumulated in the internal gate, drift towards the highly n-doped

implantation, being the most attractive potential for the electrons. Until that time, the clear contact is shielded inside a p-well, to avoid the charge competition between the clear and the internal gate during the charge collection phase. An additional implantation, called cleargate (Fig. 3.4 (a)), was introduced in between the clear contact and the internal gate, to help to the complete removal of all the charges. Controlling the voltages applied in the cleargate, this contact can also help in the charge collection phase, shielding the clear contact.

Since the first production in 2004, new optimized generations of sensors with different clear mechanisms were produced, as can be seen in Figure 3.5. The PXD4 production belongs to the clocked-cleargate (CLG) clear scheme, while for the PXD5 production (the latest one), two new clear mechanisms were introduced, common-cleargate (CCG) and capacitive coupled cleargate (CCCG).

In the CLG scheme, the clear-gate is pulsed in a similar way as the clear is, and different voltage levels are applied during the charge collection and the clear steps. Although with this system a complete clear can be achieved with moderately low voltages, the clear scheme is very complex and slow, and a new clear mechanism was introduced in the CCG PXD5 generation. In the common-cleargate scheme, a simple and fast clear can be done, while keeping the cleargate fixed at a constant potential. Nevertheless, the optimization stage turns out to be more complicated, because the cleargate voltage needs to be a trade-off between a high charge collection together with a complete clear.

A third generation , called CCCG sensors, was then produced, trying to merge the best of the two latest generations: the high charge collection and complete clear of the CLG together with the simplicity and high speed of the CCG generation. The clear is capacitive coupled to the cleargate contact, allowing a good charge collection and a fast and safe clear. While applying a constant voltage to the cleargate contact, the cleargate is lowered when the row selection is applied, confining the charges far from the clear. On the second step, when the reset pulse is applied, the cleargate is increased above its original potential, allowing a better and fast charge removal.

3.2.2 Required electronics

To operate a DEPFET sensor, two types of ASICs are needed. The row control is provided by the steering chips (called Switchers). This chips apply, depending on the generation, up to three suited potentials to the rows of the matrix: clear, gate and cleargate (if pulsed). For the clearing, as was already mentioned, a fast pulse with a relatively high voltage has to be delivered to the matrix.

The readout chip is connected to the drain currents of the pixels laying on the same row. This chip is used to read the transistor currents of the pixels independently. In the front end electronics, the currents are transformed into voltages and digitized by means of ADCs, internally or outside the chip.

All the chips have to cope with the radiation doses expected on each experi-

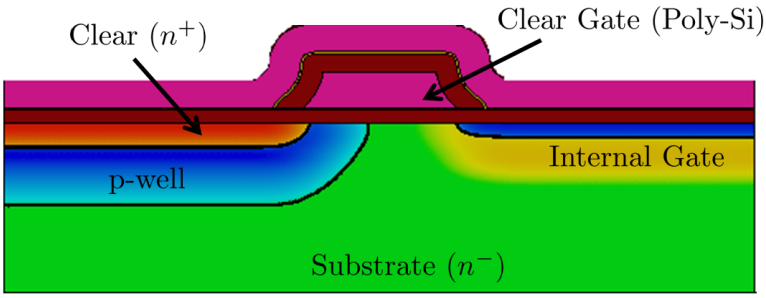

(a)

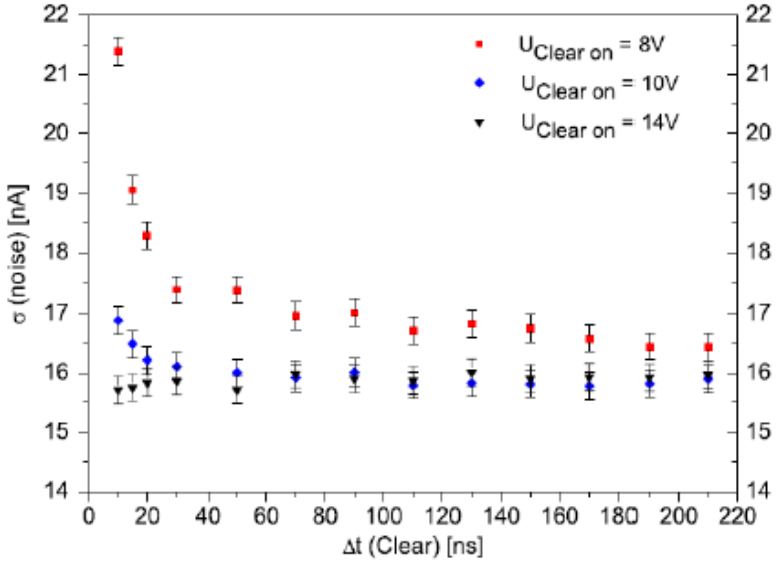

(b)

Figure 3.4: (*a*) *Doping profile of the clear region. In the clear process, the accumulated charges in the internal gate, drift towards the clear contact, helped by the cleargate structure.* (*b*) *Pedestal spread as a function of the clear pulse length [42]. The complete clear can be done in a short time (10 ns) only if the clear voltage is high enough (14 V).*

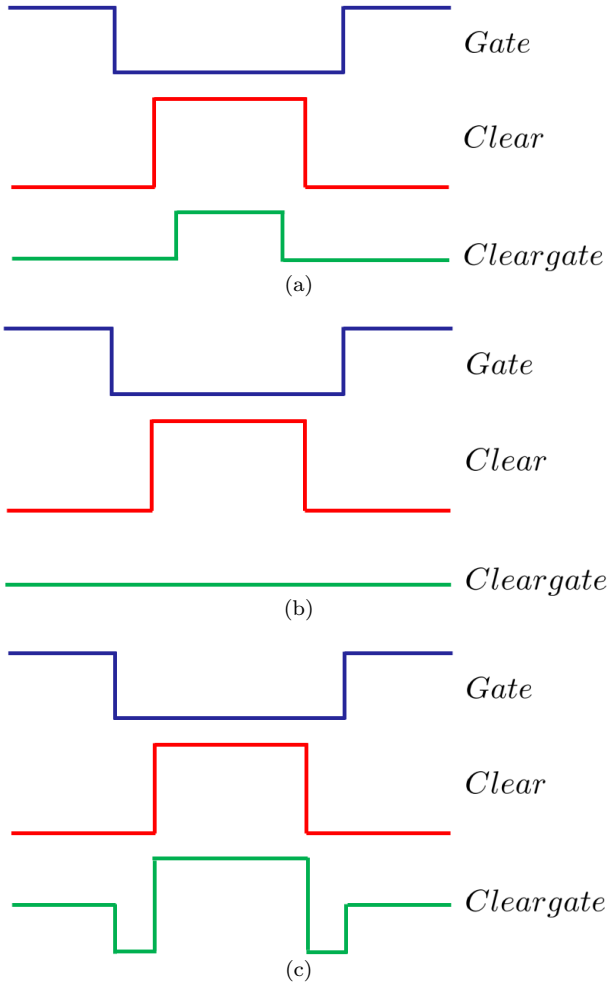

Figure 3.5: *Clear concepts tested in the PXD4 and PXD5 productions. The CLG (a) was abandoned for CCG (b), much favorable in terms of speed and lower complexity. A novel clear concept, (CCCG) (c), was introduced in the latest DEPFET production, and while being fast, a step forward in g_q was achieved.*

ment: 100 krad/year for the ILC and more than 1 Mrad/year in Belle-II (calculated for the nano beam option).

3.3 Prototype module

In order to prove the performance of the DEPFET detectors, a system test has been developed in the collaboration [43]. The main part of the prototype system (Figure 3.6, (a)), the hybrid board, has a sensor (pixel matrix) that is read out by an ASIC (CURO) and controlled by two steering chips (Gate and Clear SWITCHERs), at both sides. The full system is controlled by a FPGA (Figure 3.6, (b)) that synchronizes all the system elements and sends the data to a PC using an USB link.

3.3.1 The DEPFET Matrix

A DEPFET matrix is just an arrangement in a rectangular shape of double pixel cells in a way shown in Fig. 3.3 (a). The drain lines are connected to the readout chip in the bottom part while the gate and clear lines are common for each row and connected to the steering chips, at both sides of the matrix. The first production of DEPFET sensors was made in 2004 and it was called PXD4. Since that time, several different configurations were tested in order to find the optimal configuration for the ILC and Belle-II projects in terms of charge collection time, internal gate depth, pixel sizes, radiation hardness or clear processes. All productions were made in high ohmic unthinned (450 μm) silicon, produced in 6" wafers. While on the first production only matrices with 64x128 pixels were produced, on a second one sensors twice bigger (64x256) were tested. The pixel size was varied in a wide range, from 36x28 μm^2 down to 20x20 μm^2.

3.3.2 The steering chips

As was already pointed out, to operate the DEPFET matrix in the system prototype, two steering chips are needed: gate and clear Switchers. The first generation of chips used in the hybrid board, were fabricated using 0.8 μm HV technology and could generate the high voltage needed for the clear signals in a programmable way up to 25 V in 2x64 channels. The Switchers [44] can be daisy chained to cover longer matrices, and the voltages are sent through wire bonds.

3.3.3 The readout chip

In the system prototype, the readout chip is called CURO (CUrrent ReadOut) [45] and was fabricated using a 0.25 μm deep sub-micron process, radiation tolerant. The architecture of the chip is shown in Fig 3.7. The CDS (Correlated Double Sampling, described in Section 3.2) is the standard method for signal processing of DEPFET sensors, and works by taking the difference of two consecutive current

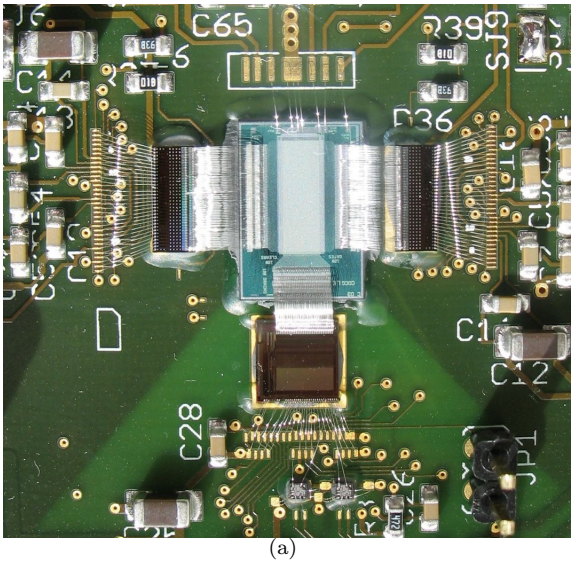

(a)

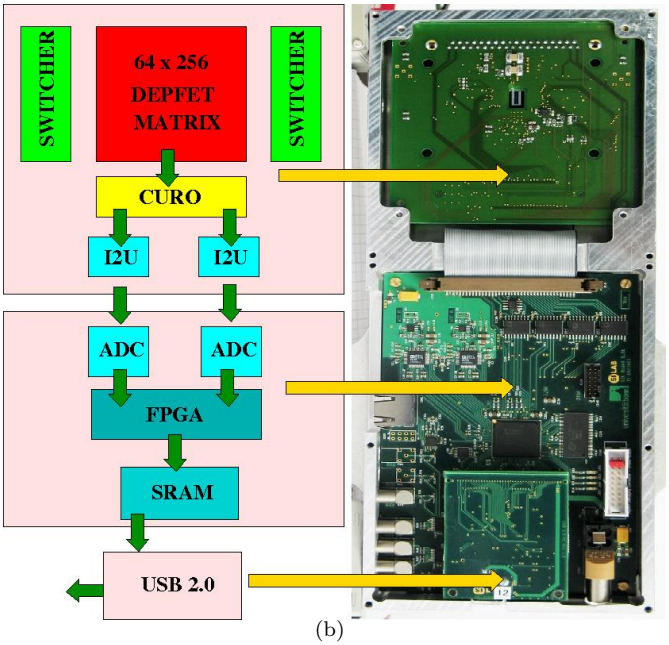

(b)

Figure 3.6: (*a*) *Photograph of the hybrid board developed for the system tests. The steering chips (Clear and Gate Switchers) are on both sides of the sensitive area (central region) and the readout chip is below it.* (*b*) *Photograph of the full S3A testing system. In the upper part, the backside of the hybrid board is visible while the DAQ and USB boards are on the lower part.*

samples before and after the clear step. The first sample in the CDS is stored in a memory cell following the regulated cascode and, when the second current (taken after the clear) arrives to the chip, both measurements are subtracted, obtaining just the signal current. This analog signal is then stored in an analog FIFO. This current is also compared with a trimmable threshold to find the digital hit pattern and the binary result obtained is stored in the digital FIFO. The addresses of the hits are then stored in a RAM memory for further readout and the analog amplitudes are then multiplexed to two externals ADCs.

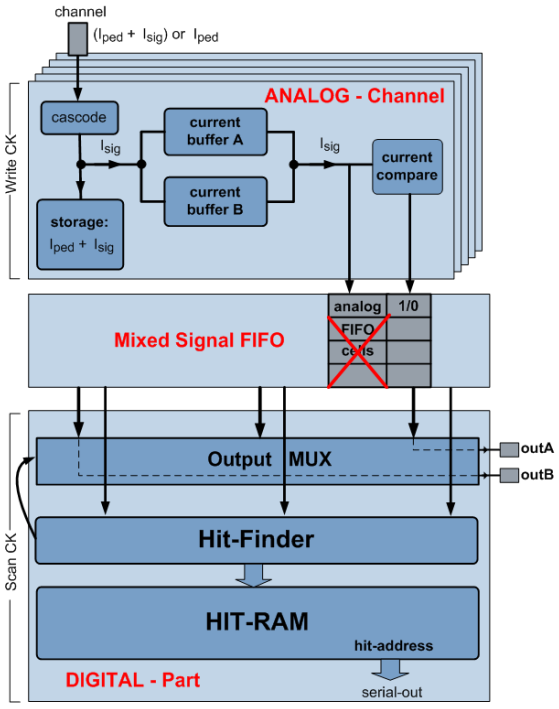

Figure 3.7: *Architecture of the CURO chip. This chip was used in the DEPFET system prototype to read the drain currents of the pixels but will be replaced by a new generation in the final design.*

3.4 The DEPFET module

Up to now, only the system prototype developed for laboratory tests have been introduced. The final modules will have special features, not present in the current system test.

3.4.1 Thinning

Although the test matrices prepared for the laboratory measurements are 450 μm thick, one of the main issues to be addressed by the vertex detectors in future e^+e^- colliders is the material budget. In order to reduce the multiple Coulomb scattering, only $0.1\%X_0$ and $0.19\%X_0$ are allowed in the ILC concepts and Belle-II, respectively, which is the equivalent to silicon thickness of 100 μm and 200 μm. Different metal layers and polysilicons have to be added to read and control the matrix, imposing a limit to the silicon thickness of 50 μm and 75 μm for each experiment, respectively.

Because of the electrically active backside implantation that is needed in a DEPFET detector, conventional thinning by backside grinding is not possible in this technology. On the other hand, backside processing afterwards is not possible with $\sim$50 μm thin sensors because of its fragility, so a new thinning technique, based on bonding and anisotropic etching, has been developed (Fig 3.8) [46].

This technique allows to produce monolithic structures with thin sensors (down to $\sim$50 μm) integrated on a thick frame ($\sim$450 μm) in 6" waffers (Fig 3.9), so such *all silicon module* needs no aditional support structure and internal stresses are avoided because of CTE (Coefficient of Thermal Expansion) mismatch between the ladder and the support material.

3.4.2 The steering chips

The Switchers present on the system prototype were developed only for laboratory test and because they are not radiation hard, can not fulfil the requirements for operating the Belle-II detector. A new chip has been designed to be used in the final detector with special features. The Switcher-B, that will allow in the same chip the selection and clearing of the pixels, has 32 channels and is implemented in AMS high voltage 0.35 μm technology providing a clear pulse of 20 V. Using thin gate oxides and a special design of enclosed devices and guard rings, a radiation tolerance of, at least, 36 MRad is achieved. In the case of the Switcher-B chips, the interconection with the sensor will be done by means of bump bonding.

3.4.3 The readout chip

The CURO chip, developed for the system tests, in the final design for the Belle-II detector will be replaced by a two complementary new generation of ASICs, called DCD (Drain Current Digitizer) [47] and DHP (Data Handling Processor) [48] (see Fig 3.10). The drain current of each pixel will be digitized by means of 8 bits algorithmic ADCs in the DCD chip that, fabricated in UMC 180 nm technology, has 256 analog inputs. The chip is radiation tolerant up to 7 MRad. The digitized data is then sent to the DHP where the data reduction will be performed. This ASIC, fabricated in IBM 90 nm technology can store raw data and pedestals, perform the common mode correction, pedestal substraction and zero suppression

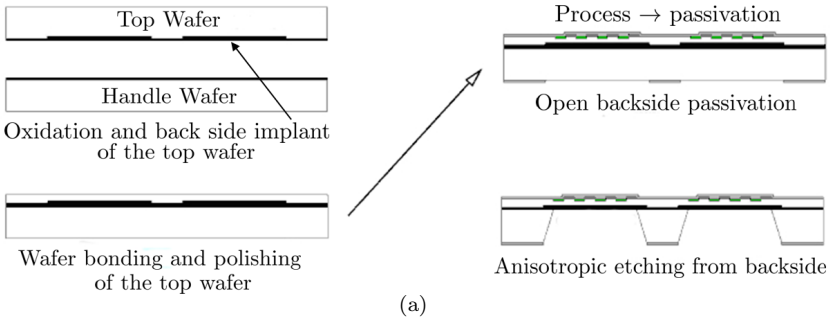

(a)

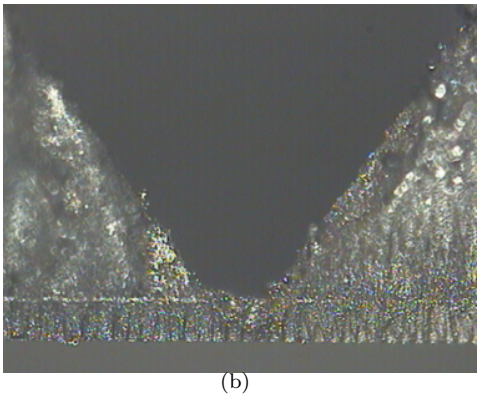

(b)

Figure 3.8: (*a*) *Processing steps of the thinning technology for electrically active back-side implantations. Starting with the back-side implantation of the top wafer, both wafers are direct bonded after the oxidation. The top wafer is then thinned down to the desired thickness. The processing of the DEPFETs on the top wafer can then start just by using conventional equipment, and the backside is passivated leaving open holes on the handle waffer where the no needed material is placed. Finally, windows is the handle wafer are opened by deep anisotropic wet etching; The etch of the backside stops at the oxide interface between the two wafers.* (*b*) *Microphotography of the interface between the handle and top wafers. The V groove in the handle wafer after the wet etching is also clearly visible.*

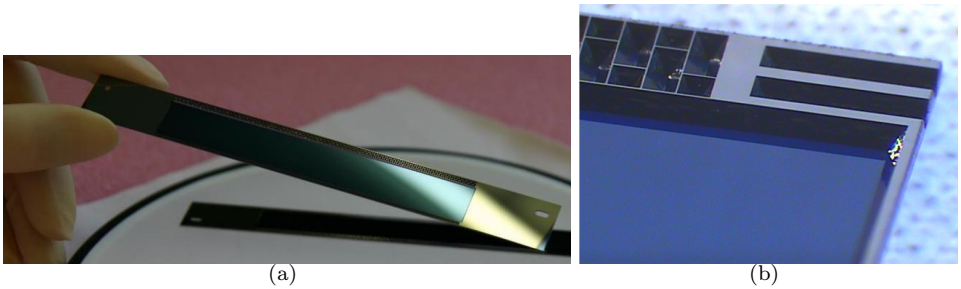

(a) (b)

Figure 3.9: (*a*) *Mechanical sample of the Belle-II PXD inner layer. The central part is the sensitive area, thinned down to 50 µm. The sensor is supported by a thick silicon rim (450 µm) with a hole pattern* (*b*) *etched for material reduction underneath the lateral balconies. In the final design, one full ladder will contain two half ladders joint in the middle.*

and can generate the timing signals and configuration files for the DCDs and Switchers. All this chips, as in the Switcher-B case, will be connected to the sensor by means of bump bonding in the final experiment.

3.5 General layout of a DEPFET detector

The layout of a vertex detector based on the DEPFET technology is similar for both projects, ILC and Belle-II. The basic unit is the DEPFET ladder (Fig. 3.11 (*a*)), with the sensitive area in the central region (thinned down to the desired thickness), the Switchers laying on the lateral balcony and the readout chips (DCD and DHP) bump bonded on the end of stave. This configuration allows to disipate the highest amount of power (coming from the readout chips) in the most convenient part for cooling that is the end of the stave. The full detector can be built by arranging the ladders in several layers in a cylindrical structure (Fig. 3.11 (*b*)) around the beam pipe.

Because of the different requirements needed for the two projects, two layouts with specific characteristics are needed for each project. ILC needs five ultra-thin layers covered with very small pixels (Table 3.1) while for Belle-II, two layers with moderate pixel sizes in a 75 μm thick substrate (Table 3.2) are enough to cope with the requirements. In both designs, the readout is done from both sides so the two sensor halves are read in paralel and shorter readout times are needed. The readout speeds are imposed to keep the occupancy below 1%. The occupancy is mainly generated by the background, and the performance of the tracking algorithms would be degraded with higher levels, asociating fake tracks to the background hits.

In order to achieve small pixel sizes, two pixels share the source and gate electrodes (Figure 3.12 (*a*)). Both transistors form a double cell structure (the basic building block), are controlled by a common gate, and the clear is performed

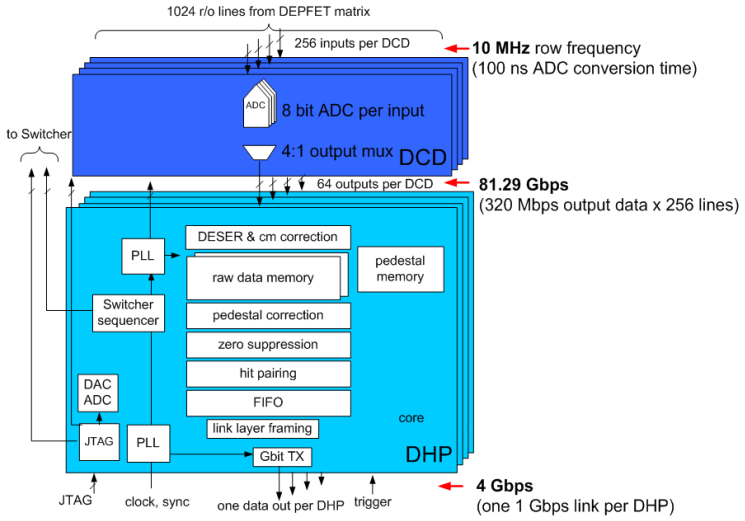

Figure 3.10: *Schematic architecture of the DCD and DHP chips. The drain currents are digitized in the DCD while the DHP can store raw data and pedestals, perform the common mode correction, pedestal substraction and zero suppression. In adition, can generate the timing signals and configuration files of the DCD and Switchers.*

with the same contact (the clear and the gate contacts of the pixels belonging to the same row are connected and read and cleared at the same time). The two drain lines are connected to two different readout channels an read in paralel at the same time. This double cell structure allows the increase of the readout speed by a factor two, needed to meet the frame time requirements in the ILC project. In case of Belle-II, even higher readout speeds are needed, so to solve this problem, and because of the pixels are bigger, four columns can be read in parallel, instead.

Layer	♯ ladders	Radius [mm]	Area [mm^2]	Pitch [μm^2]	r/o time [μs]
1	8	15.5	100x13	25x25	25
2	8	26.0	250x22	25x25	75
3	12	38.0	250x22	25x25	100
4	16	49.0	250x22	25x25	100
5	20	60.0	250x22	25x25	100

Table 3.1: *Default geometrical parameters of the DEPFET based ILC vertex detector.*

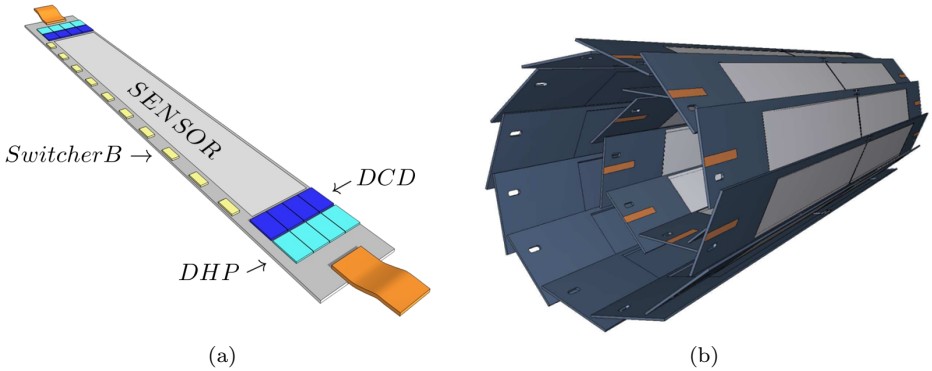

Figure 3.11: *Artist's view of* (*a*) *a single Belle-II ladder and* (*b*) *the full vertex detector arranged in two cylindrical layers around the interaction point.*

Layer	♯ ladders	Radius [mm]	Area [mm^2]	Pitch [μm^2]	r/o time [μs]
1	8	14.0	80x12.5	50x50	20
2	12	22.0	120x12.5	75x50	20

Table 3.2: *Geometrical parameters for the DEPFET Belle-II PXD detector.*

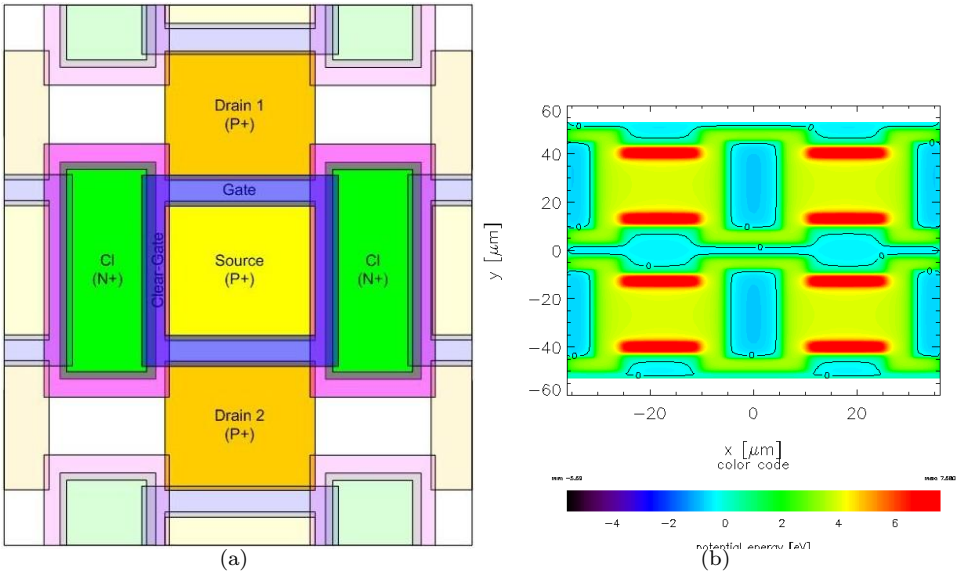

(a) (b)

Figure 3.12: (*a*) *Double pixel cell within the matrix array. The source contact is shared between two pixels.* (*b*) *Simulated potential distribution in 1 μm depth during the charge collection step. The minimum of potential for the electrons are the red areas, that correspond to the internal gates. The clear contacts are the ligth blue regions.*

Chapter 4

DEPFET characterization

May work in a lab, but the tiny signals will be lost in the noise in an accelerator environment!

Old comments about the SLC detector. Book of appointments C. Damerell.

In the following chapter, the characterization of two generation of DEPFET matrices (PXD4 and PXD5) with two different clear mechanisms will be introduced. Finally in section 4.4 a simulation of a CCG matrix using the CLG generation is discussed.

4.1 Common data analysis chain

Analog data from the DEPFET-CURO system are multiplexed to the transimpedance amplifiers and ADCs mounted on the readout board. The analog data are stored and processed off-line in a number of steps:

- Pedestal distribution: The pedestal is the average signal present in our device without any external signal (hits). The pedestals are calculated in two steps:
  1. The average and the standard deviation of the signal is calculated for each pixel.
  2. The first point is done again, but applying a cut of $\pm 4\sigma$ to the signal, in order to remove the hits present on the device.
- Common mode: Is the mean signal for each row, after pedestal subtraction and hit removal.
- Noise calculation: The noise distribution is the signal that remains after the pedestal and common mode subtraction (without hits). It is calculated as the sigma of the Gaussian fit of the curve remained around 0.

- Cluster finding: The first step in the clustering consists on finding the seeds over the matrix. For that, one have to look for the signals all over the sensor with an amplitude more than 6 times (although this threshold is trimmable) the noise (σ) of the pixel. This threshold can be, nevertheless, modified voluntarily. Once the seed of the signal is located, to find the cluster one have to look for the signal that is 2 times above the noise on the pixels in a square window around the seed. The clusters studied cover an area of 3x3, 5x5 or 7x7 pixels.

4.2 PXD4 DEPFET matrix generation

The first tested device was produced in the PXD4 generation using a CLG (Clocked Cleargate) clear scheme with a pixel size of 36x28.5 μm^2, a thickness of 450 μm and having 64 columns and 128 rows.

4.2.1 Sensor optimization: Determination of optimal voltages

As a first step, the optimal working point of the DEPFET system is determined. To this end the following supply voltages are scanned: gate-source voltage difference, clear and backplane. The gate-source voltage regulates the current flowing into the transistor, resulting in a direct influence of the system gain; obviously, this parameter has to be maximal. The clear voltage has to be fixed at a potential such that all the charges must be removed from the internal gate, assuring a complete clear; theoretically, the higher clear voltages, the higher probability of having a complete clear of the device. The backplane scan aims the point where the sensor is fully depleted, ensuring a good charge collection.

For each set of voltages data are taken while illuminating the DEPFET with a Ba-133 source. The signal is defined as the mean value of the Gaussian fit of the 30 keV peak.

V_{gate} scan

The first scan was made varying V_{gate} and keeping constant V_{source}, for three different values of the later voltage. Figure 4.1 shows the results of this scan. The plots show, respectively, the signal, noise and signal to noise ratio of that scan as a function of the difference $V_{gate} - V_{source}$, for three values of V_{source} (7 V, 6 V and 5 V). The best results are obtained for a values of V_{source}=6 V and V_{gate}=3 V. With these values, compared with the starting scan voltages (V_{source}=7 V and V_{gate}=2 V), an improvement of $\sim$60% in the signal to noise ratio is achieved while the noise level is reduced from 19 ADC down to $\sim$13 ADC units.

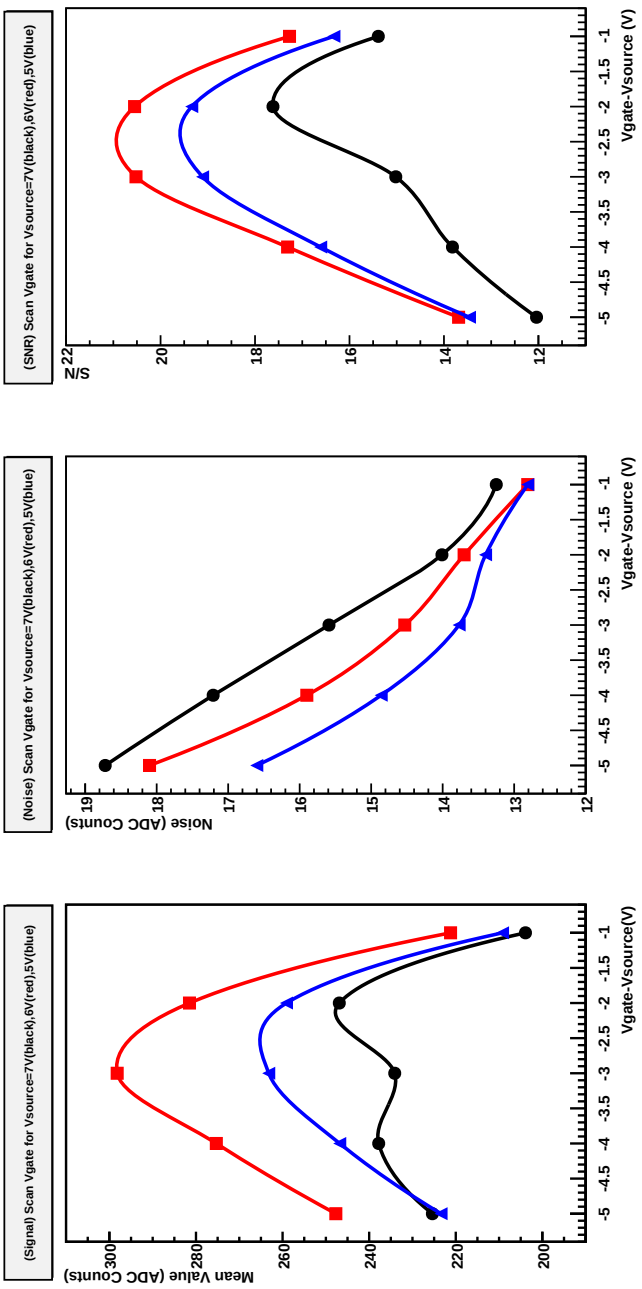

Figure 4.1: *Results of the scan of V_{gate} for different values of V_{source} (6 V squares, 5 V triangles, 7 V circles) in terms of signal, noise and signal to noise ratio.*

V_{clear} scan

Once the two first voltages are fixed, the next important voltage is V_{clear}. Varying this voltage, one can see if the clear of the matrix is complete. The results from a scan of the clear voltage are shown in Figure 4.2. In this case, as an example, the scan was made from 17 V to 23 V in steps of 2 V, for fixed values of V_{gate}=5 V and V_{source}=7 V. Although these are not the best values obtained in the previous scan, the observed behavior was repeated using whichever allowed combinations between gate and source voltages. The signal to noise ratio increased with higher clear pulses, independently of the gate-source difference, in this voltage range.

As before, the Ba-133 peak at 30 keV is used to study the variation of the signal as a function of the clear voltage.

The signal is found to increase monotonically up to the maximum voltage set here. At the same time the noise decreases. Clearly, working under the starting scan conditions (V_{clear}=17 V) does not guarantee a complete clear of the charges collected in the internal gate thus resulting in an increment of the noise. The signal level is determined by the subtraction of two consecutive samples of the DEPFET drain current (before and after the clear) so if the clear is incomplete, some charge remain in the internal gate that contribute to reduce the difference level between the two samples; in addition, those remaining charges have influence in the charge level variation of the first sample with respect to the next ones, resulting in an increased noise. Although the best results are obtained with the maximum voltage that can be delivered with this generation of the switcher chip (V_{clear}=23 V), in fact no sign of saturation of the signal is seen in the range of voltages investigated and probably, with higher voltages, better signal to noise ratio levels could be achieved.

$V_{backplane}$ scan

The last free parameter to fix is $V_{backplane}$, the voltage governing the side-wards depletion of the device. The effect of $V_{backplane}$ on the response is studied using a 1060 nm laser. In Figure 4.3 the voltage is scanned from -20 V to -100 V in steps of 10 V. Figure 4.4 shows a more detailed scan, with voltages from -2 V up to -40 V. Applying voltages lower than -15 V no depletion is achieved in the substrate and thus no signal is collected. Raising the supply voltage further, the signal increases rapidly, reaching a plateau at approximately 35 Volts, where the substrate is already fully depleted. Increasing the voltage above -60 V, the signal to noise ratio decreases slightly, so the selected value is -40 V$\leq V_{backplane} \leq$-60 V.

Final voltages

On the basis of the voltage scans described above the working point of the DEPFET matrix is defined in Table 4.1.

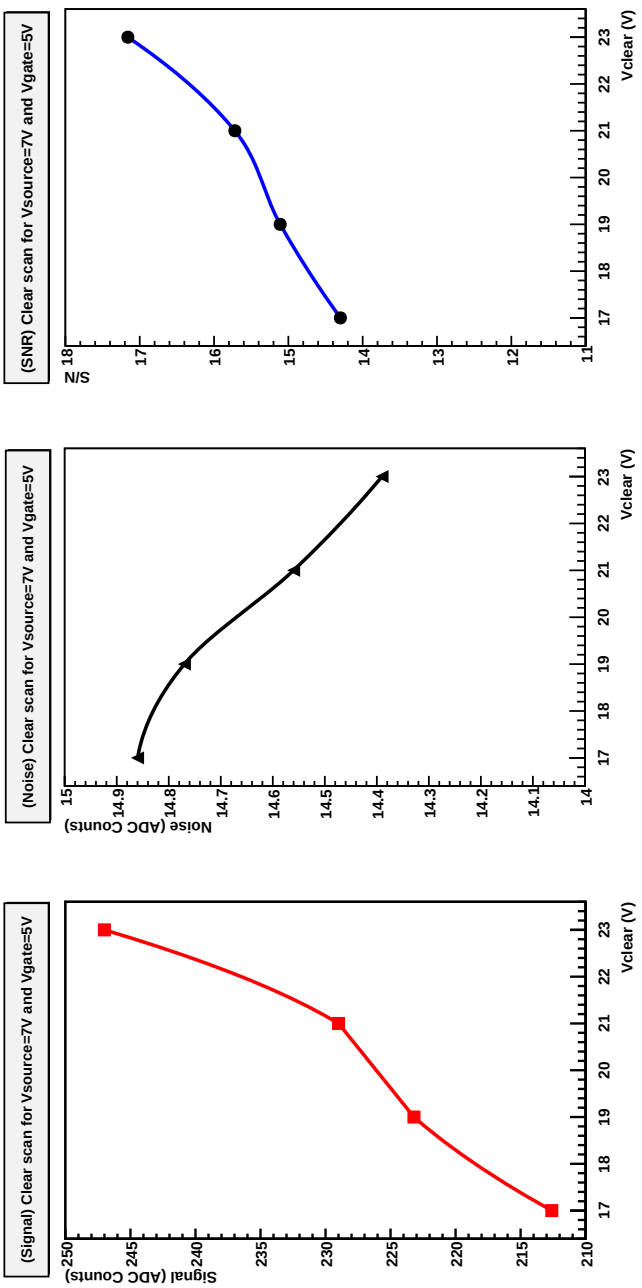

Figure 4.2: *Results of the scan of V_{clear} for a fixed values of $V_{gate} = 5\ V$ and $V_{source} = 7\ V$.*

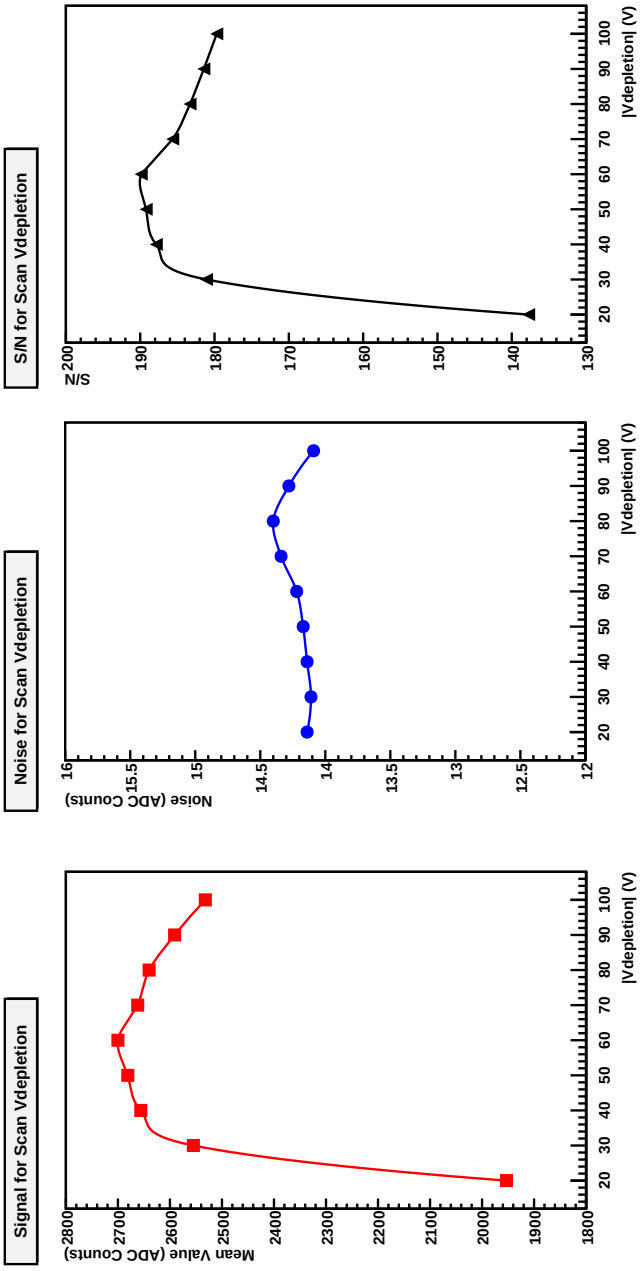

Figure 4.3: *Signal, Noise and signal to noise ratio for different $V_{backplane}$. Once the substrate is fully depleted at ∼40 V, the charge collection enters in the plateau region, and increasing the backplane voltage has no major effect.*

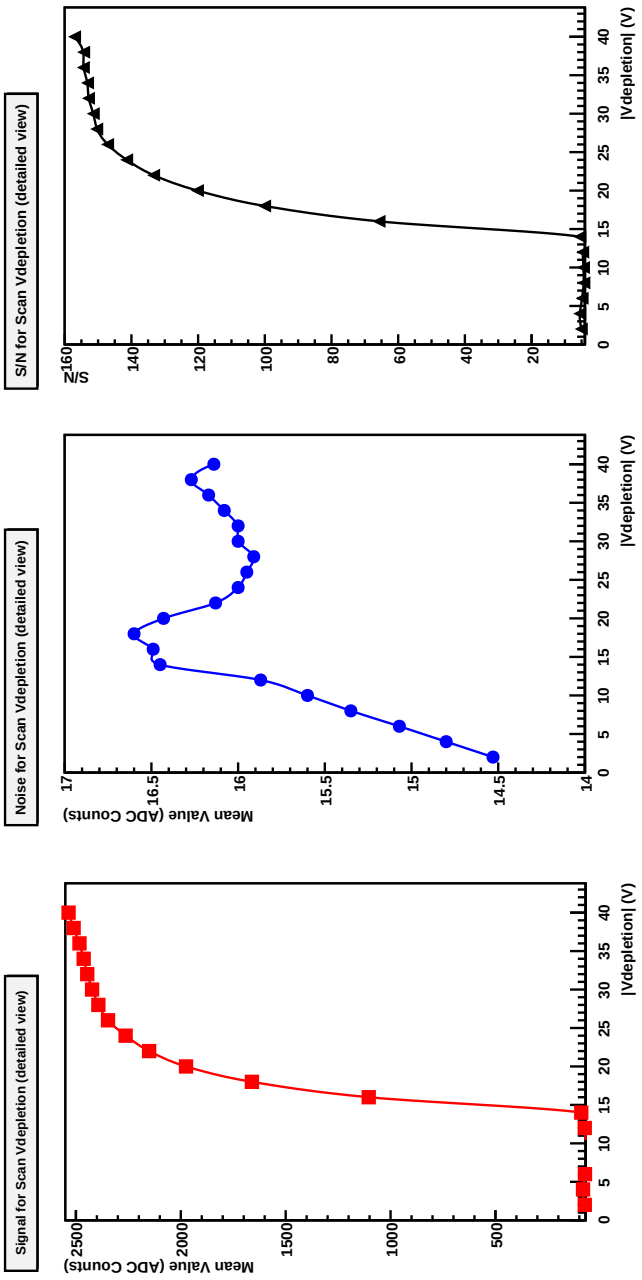

Figure 4.4: *A detailed scan of signal, noise and signal to noise ratio for small $V_{backplane}$ voltages, from -2 V up to -40 V. With voltages lower than -15 V no depletion is achieved and no charge is collected.*

Voltage	Value (V)
Source	+6
Bulk	+ 10
Backplane	-60
Clear High	+23
Clear Low	+8
Cleargate High	+9
Cleargate Low	+6
Gate High	+15
Gate Low	+3

Table 4.1: *Final operation voltages*

The next step, to determine the performance of the device, is to study the distribution of the pedestals and noise in the matrix. Values of these quantities are shown in Figure 4.5 for each pixel of the matrix. While pedestals are rather uniform, with an average value of ∼8200 ADC units, the noise shows a number of features:

- The average noise level for the final supply voltages is approximately 15 ADC counts.
- The noise of the two ADC (32 channels each, corresponding to 32 columns) is quite similar, but not the same (Fig. 4.6 and Fig. 4.7).
- There are 3 columns with higher noise compared to the matrix average.

The noise level of pixels digitized by ADC1 (Fig. 4.6) and ADC2 (Fig. 4.7) show a significant difference that will slightly affect the signal levels collected with the radioactive sources (see next section). Some pixels have a noise higher that 30 ADU and although there are only a few (mainly on the matrix edges), should be masked.

First results using radioactive sources

This section shows the results obtained by using radioactive sources and working under the conditions described in last point. The first result is shown in Figure 4.8, where one can see the seed pixel location using a Ba-133 radioactive source. The edges are not considered in this analysis, that is the reason why no seed is found in this area. The whole matrix presents an uniform behavior.

Figure 4.9 shows the spectra of two radioactive sources, Ba-133 and Cd-109 taken with the sensor using the optimized voltages. The Gaussian fit of both peaks gives the following results:

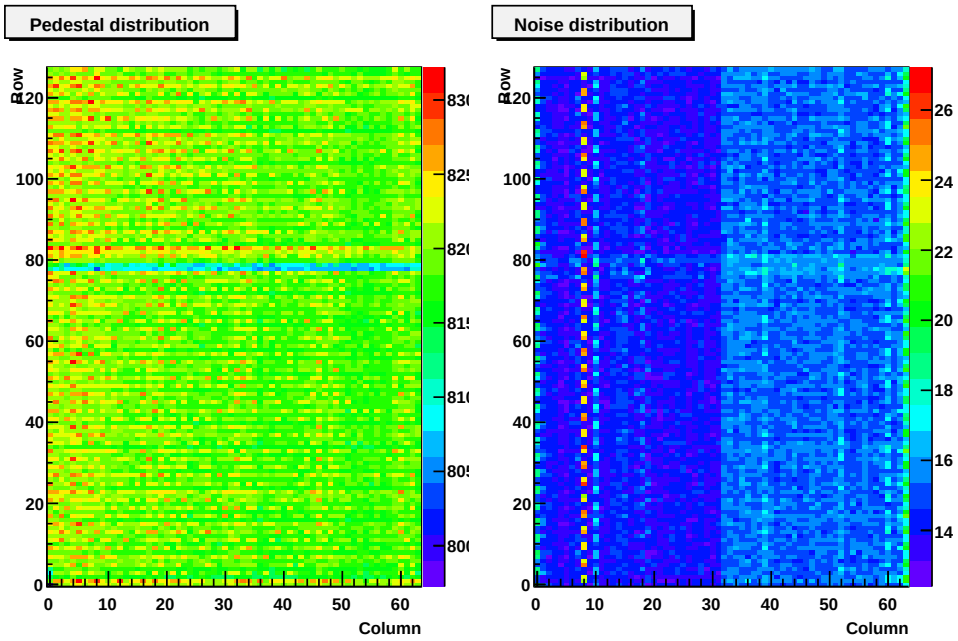

Figure 4.5: *Pedestal and Noise distribution, measured for the final voltages chosen.*

- Ba-133 (30 keV)⟶Mean Value=310.4 ADC Units (S/N=20.33)
- Cd-109 (22 keV)⟶Mean Value=209.9 ADC Units (S/N=14.54)

For both sources, these peaks actually contain two sub-peaks that are just about visible. Although at a first sight these peaks could be linked to two photons close in energy emitted by the sources, this fact is just an artifact due to the different gain of the two ADCs (as suggested by Fig. 4.6 and Fig. 4.7).

In the case of Ba-133, two photons of energies 30.6 keV and 30.9 keV are emitted. With such energies, the 30.6 keV photon is expected to produce 8500 e^- while 8583 e^- are expected in the 30.9 keV case. Having a noise level of 330 e^- (Eq. 4.1), it is clear that the DEPFET could not resolve such similar energies, and that both sub-peaks correspond to the same peak but read with the two halves of the matrix.

For the Cd-109 source, two photons of energies 22 keV and 25 keV are expected to produce 6111 e^- and 6944 e^-, respectively. These peaks could be resolved by the sensor but taken into account the fact that they are emitted with a probability of 84% and 18%, respectively, is not expected to have both peaks of the same height, but one should have just the 20% of the height of the second. Once again, this fact can be explained by the two different gains in both halves of the detector.

Having the energies of the particles and the corresponding ADC counts, the gain of the system can be extracted using the slope of the linear fit of the two

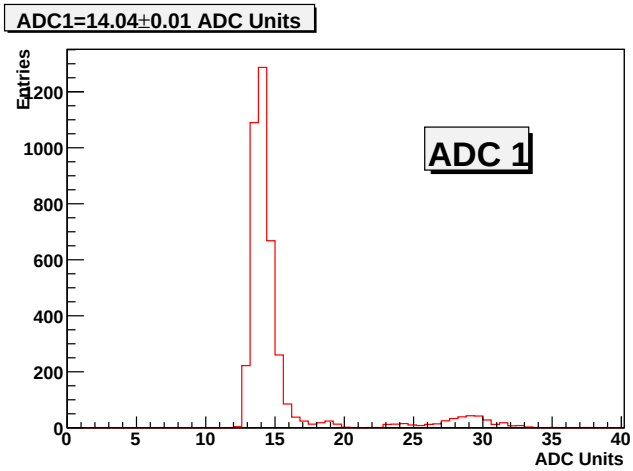

Figure 4.6: *Noise distribution for ADC 1. The first ADC reads the 32 pixel columns laying in the left half of the matrix. The noise peak is centered in 14 ADC units. The entries at higher values belong to hot pixels, that are excluded from the analysis.*

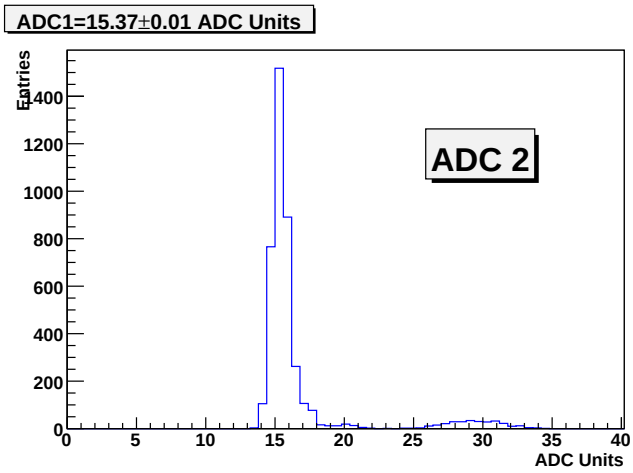

Figure 4.7: *Noise distribution for ADC 2. The second ADC reads the 32 pixel columns in the right part of the matrix. In this case, the noise peak is centered in 15.4 ADC units. As in ADC 1, the hot pixels that produce the entries at higher ADC values, are excluded from the analysis.*

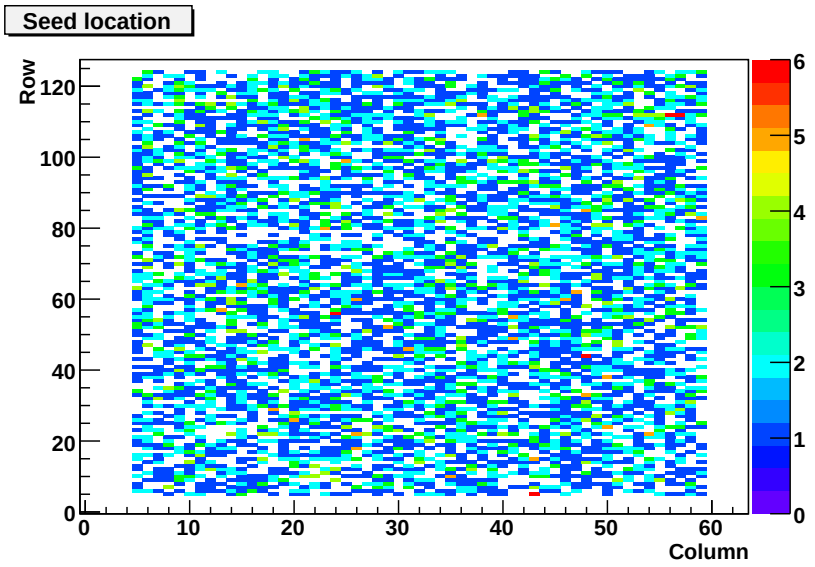

Figure 4.8: *Seeds found using a Ba-133 radioactive source. Note that the edges are not used for the seeds search.*

points. The slope gives a gain factor of 12.5 ADC/keV. Using the conversion factor, the noise, written in terms of ADC units, can be expressed in electrons using the energy needed to create an electron-hole pair in silicon; thus, the ENC level is estimated to be approximately 330 e^- (Eq. 4.1):

$$ENC = 15\ ADC \cdot \frac{1\ keV}{12.5\ ADC} \cdot \frac{1e^- h}{3.6 \cdot 10^{-3}\ keV} \sim 330\ e^- \tag{4.1}$$

The g_q factor (the gain of the system) can be also calculated (Eq. 4.2):

$$g_q = \frac{12.5\ ADU}{1\ keV} \cdot \frac{7.7\ nA}{1\ ADU} \cdot \frac{3.6\ eV}{1\ e^-} \sim 346\ pA/e^- \tag{4.2}$$

Scanning the matrix using laser

The charge collection uniformity or the charge sharing between adjacent pixels, can be studied in the laboratory using a diode laser. The laser test system is based on an emitter of wavelength of 1060 nm corresponding to a photon energy of 1.17 eV, just above the energy gap of the silicon at room temperature (1.12 eV), thus ensuring an uniform ionization along the laser path. The penetration depth in silicon is around 800 μm, allowing a complete transversal of the 450 μm detector. The laser is driven by a pulse generator, that produces a square pulse of 600 mV and 30 ns, with a repetition time of 10 ms. The laser diode is mounted on a micro-metric support structure held to an aluminum cantilever that is controlled

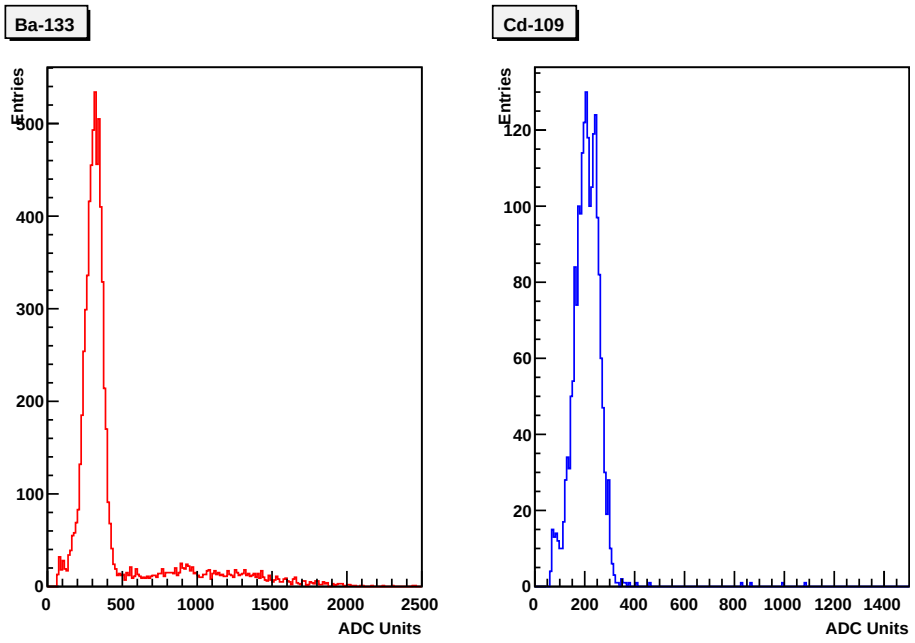

Figure 4.9: *Spectra of two radioactive sources, Ba-133 and Cd-109.*

remotely using a XYZ-motorstages. In order to be able to resolve the smallest sensor structures possible, the laser spot has to be minimal. The optimal configuration of the laser spot on the matrix was done by finding the optimal vertical distance to the matrix (Figure 4.10), that allows to focus the laser spot, and also the angle (Figure 4.11) that guarantees a perpendicular incidence over the sensor.

After fixing the proper distance between laser and matrix (∼35.65 mm in this case) and the angle (19 A.U. in this case), a scan of a matrix area of 100 μm · 50 μm in steps of 5 μm was performed. The result of the scan can be seen on Figure 4.12. It shows the average seed pixel charge (the pixel with the largest signal of the event) as a function of laser position. The 'red' squares are the centers of the pixels, where charge sharing between pixels is the smallest. The 'green' lines denote the position where charge sharing is maximum, i.e. the pixel boundaries.

One can see better the structure of the matrix if one observe the Figure 4.12 (middle) and 4.12 (bottom), where the projections of the Fig. 4.12 (top) over the axis X and Y are shown. The fit with a combination of error functions and complementary error function yields a value for the Gaussian width of the laser spot: 4.0 μm in X and 4.8 μm in Y. The periodicity of the function gives an estimate of the pixel size: 38.0 μm in X, 30.0 μm in Y, fully compatible with the design value.

While the laser scan is definitively able to distinguish structures at the sub-pixel level (as seen in Fig. 4.12 (top)), the total cluster charge is found to be quite

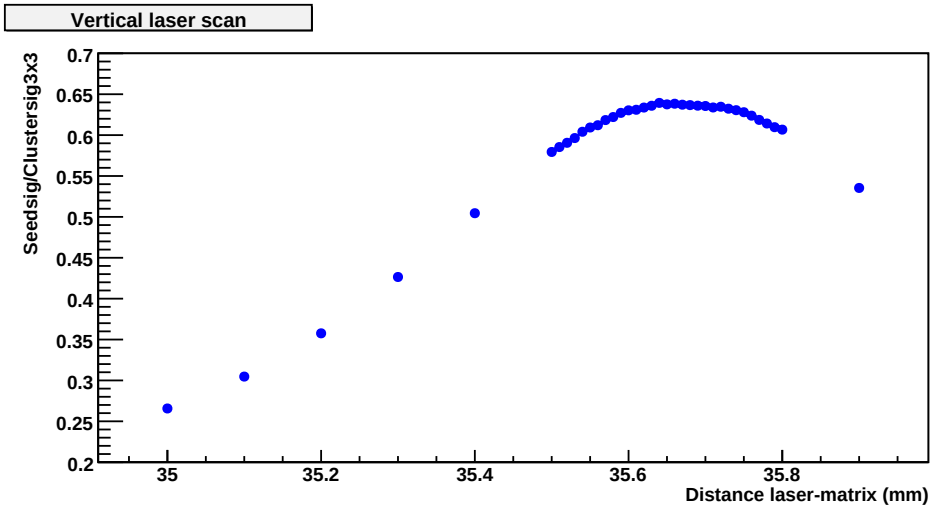

Figure 4.10: *The proper distance between laser and matrix was found maximizing the ratio of the charge collected in the seed and the cluster charge, forcing the cluster to be as small as possible.*

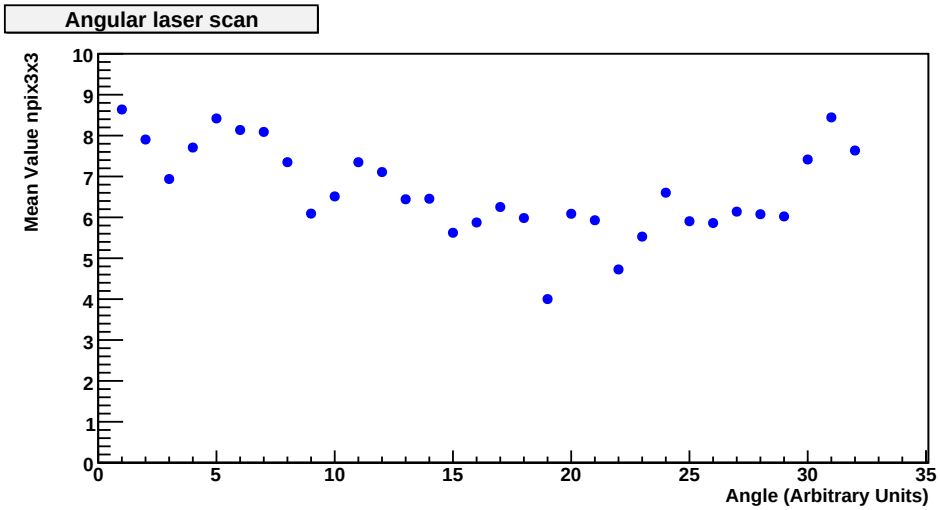

Figure 4.11: *The angle was selected analyzing the number of pixels in a 3x3 cluster. Once the laser comes into contact with the matrix in a perpendicular way, this number (cluster size) should be minimal. The value of 19 (in arbitrary units) was selected.*

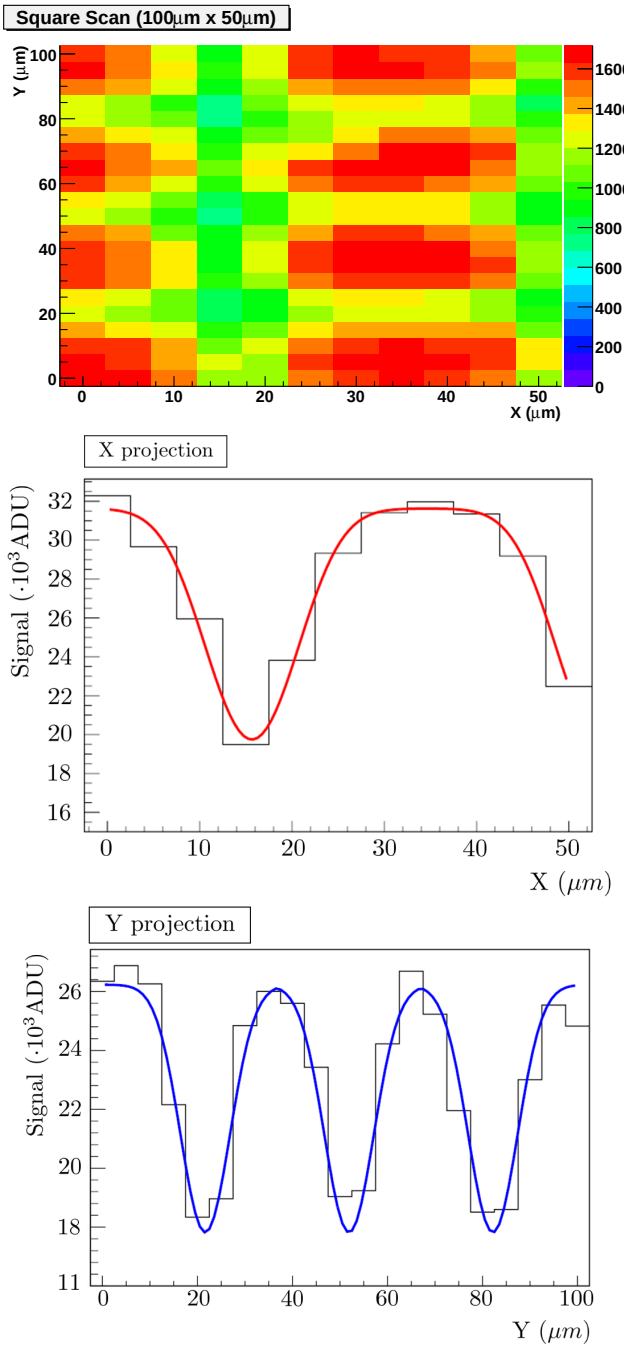

Figure 4.12: *The average seed pixel charge in an area of 100 μm · 50 μm within the matrix and the sum of the charge deposited in X and Y directions are shown. The scan was made in steps of 5 μm, looking for the pixels with the highest signal of the event.*

stable. In Figure 4.13 the 3x3 cluster charge is shown versus laser spot position. Some structure is seen, but the total variation is small: the RMS of all measured signals is 1.8%.

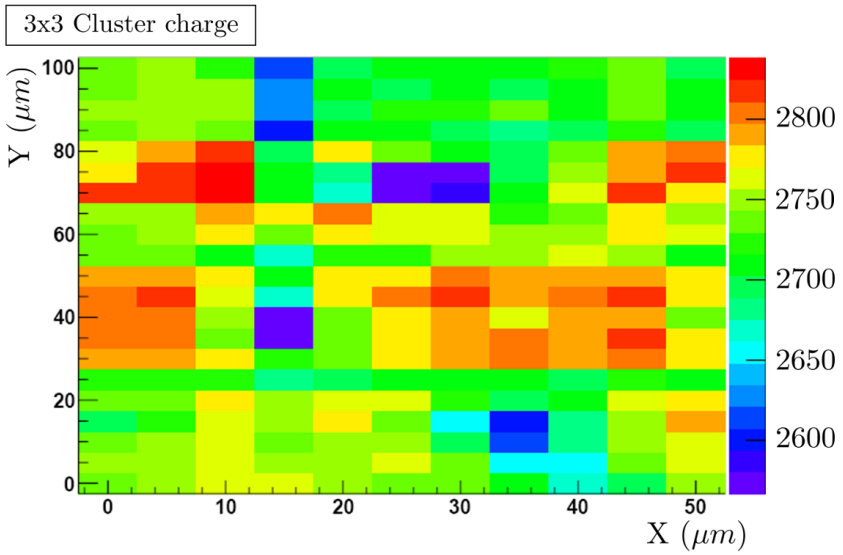

Figure 4.13: *View of an area of 100 μm · 50 μm. The scan was made in steps of 5 μm.*

4.3 PXD5 DEPFET matrix generation

In the following section all the results shown correspond to the same DEPFET matrix produced in a PXD5 generation with a CCG (Common Cleargate) clear scheme with a pixel size of 32x24 μm^2, a thickness of 450 μm. The steps followed to process the data are the same that for the PXD4 matrix generation.

4.3.1 Voltage scan

As a first step the optimal working point of the DEPFET is determined. To this end the different supply voltages are scanned. As in the previous generation, the efforts has to be channeled into a voltage configuration that avoids an incomplete clear of the device and that ensures a fully depleted substrate. Thus, clear high, clear low, cleargate and backplane are the voltages that have to be optimized. The starting working conditions were obtained using simulations of the device, the the different voltages will be varied around these central values.

For each set of voltages, data are taken while illuminating the DEPFET with a Ba-133 source. The signal is defined as the mean value of the Gaussian fit of the 30 keV gamma peak.

V_{Clear_High} scan

The first point is to scan the Clear High voltage in order to be sure that a complete clear is made. A scan between 13 V and 22 V in steps of 0.5 V was performed.

In Figure 4.14, the results of this scan are shown. In this figure, the SNR increases as one increase the Clear High voltage, up to a value of 19 V where the signal-to-noise ratio seems to be constant. At that value (and above) we are sure that we are under a complete clear region and that we are collecting all the charge deposited under the internal gate, that is the reason why we have chosen 19.5 V for this voltage.

V_{Back} scan

Another important parameter is V_{Back} because this voltage indicates when the matrix is fully depleted. In the Figure 4.15, the results of this scan (from -130 V and -250 V in steps of 10 V) are shown. Here we obtain a similar behavior as in the V_{Clear_High} scan. One can increase the SNR by increasing the depletion voltage, up to a value $\sim$-220 V where the signal-to-noise remains more or less constant. The final value that we have chosen is -230 V, to be sure that we are in the right region.

In Fig. 4.15 there are three sections, the central one between -170 V and -210 V. The explanation of this effect could be that this scan was performed in 3 different days and some variation in the room's temperature could be expected, thus affecting the leakage current produced in the substrate. Because of the pedestals are calculated using the first thousand events and used as constant all over the run, minor changes in the conditions will lead to variations in the estimated charge.

V_{Bulk} scan

No great variation is observed (neither in the signal nor in the noise) when varying V_{Bulk}. A scan between 12 V and 19 V in steps of 1 V was made and the result of this scan is shown in Figure 4.16. Although no major variations were observed in the signal to noise ratio within this range, $V_{Bulk} = 16\ V$ seemed the best result and was the voltage chosen.

V_{CCG} vs V_{Clear_Low} scan

Finally, a bidimensional scan was performed, involving CCG (from 3.5 V to 7 V in steps of 0.5 V) and ClearLow (from 11 V to 14.5 V in steps of 0.5 V). The results of this scan are shown in Figure 4.17.

The noise distribution is uniform all over the matrix so no point is preferred using this criteria. Looking at the SNR distribution, a maximum is achieved using $V_{CCG} = 5.5\ V$ and $V_{Clear\_Low} = 11.5\ V$. If one moves around this point, the signal

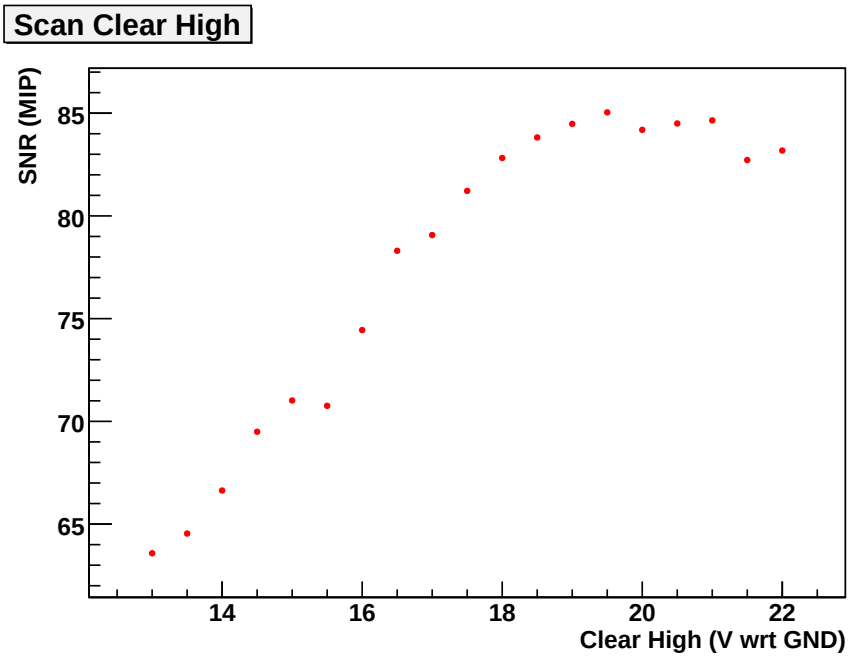

Figure 4.14: *Results of the scan of* V_{Clear_High}.

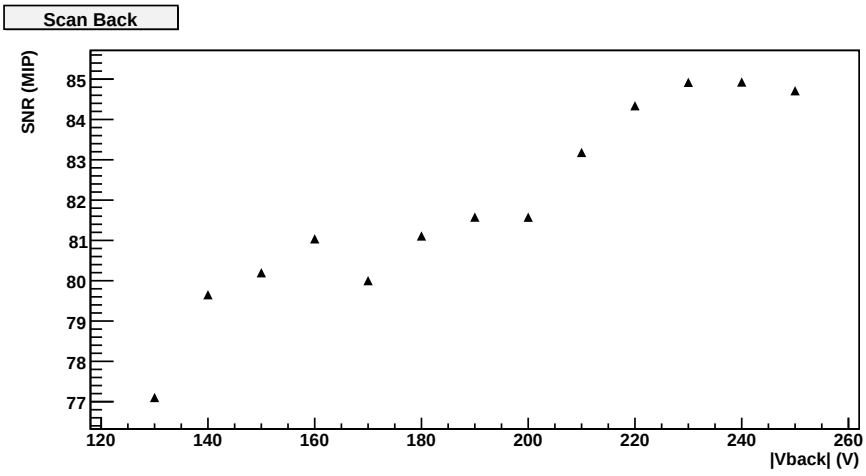

Figure 4.15: *Results of the scan of* V_{Back}.

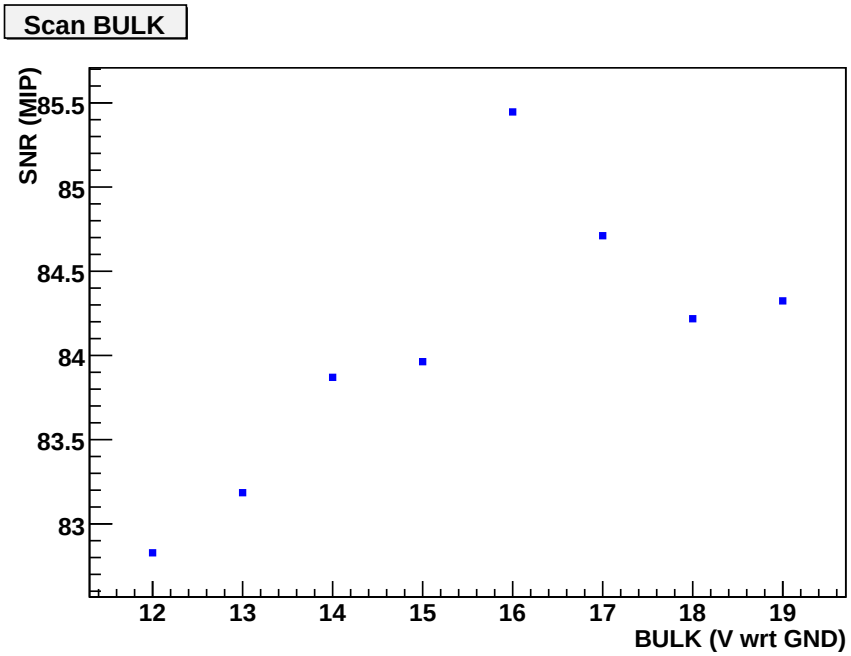

Figure 4.16: *Results of the scan of V_{Bulk}.*

decreases whatever the direction one chooses, so this configuration seems to give the optimal performance.

Looking at the Figure 4.17 one can see that there are a lot of points marked with a 0 label. In those points, the combination of the voltages in the system, produced a bad response of the matrix (appearing as a hole illuminated area), and were excluded from the optimization stage.

Final voltages

As a result of the scans performed to our matrix, the best configuration achievable for this matrix is summarized in Table 4.2:

With these final parameters, a final run was taken (using 50000 events with a Ba-133 source) and the main features of the matrix are shown in the Figure 4.18. As one can see on the first histogram, the noise of the system is between 12 ADU and 14 ADU. Converting this number ($\sim$13 ADU) of electron-holes pairs (using the calibration given by the Ba-133 and Cd-10 sources), the ENC level is around 360 electrons. The noise distribution over the whole matrix is quite uniform, and just the hot rows in the middle show a higher noise, that contribute to the small peak on the noise distribution ($\sim$25 ADU).

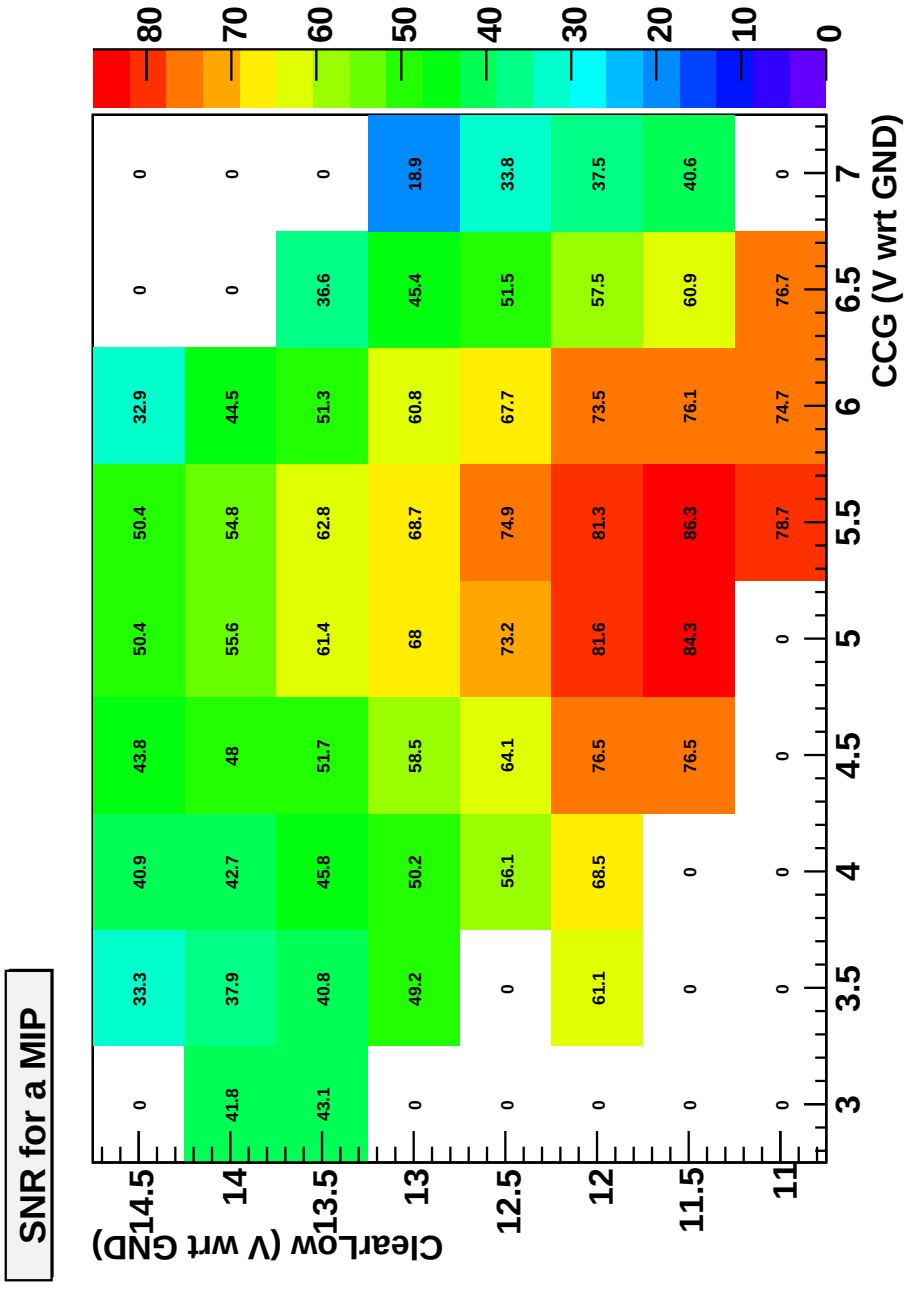

Figure 4.17: *Signal to Noise Ratio (scaled to a MIP) for a the 2dimensional scan of* V_{CCG} *vs* V_{Clear_Low}.

	Voltage(V)	Current(mA)
Source	5.5	6
Gate High	12	0
Clear High	19.5	1
Cleargate	5.5	0
Clear Low	11.5	21
Bulk	16	0
Gate Low	1.5	0
Backplane	-230	$\sim 10^{-3}$

Table 4.2: *Final operation voltages and power consumption*

From the Cluster Size histogram one can see that the number of pixels in a cluster 3x3, 5x5 and 7x7 are the same, so we can conclude that the charge is confined in a small area of the matrix.

The pedestal distribution is, again, quite uniform along the hole matrix and centered around ∼8000 ADU.

The last plot (Fig. 4.18, bottom right) shows the masked pixels (∼13% of the total number of pixels). The edges of the matrix and the hot rows are excluded for the analysis (the cluster finding algorithm can not work well in this regions), so we are just considering the well behaved part of the matrix.

Calibration

The next step, once that one knows the right voltages of the matrix, is to obtain the final signal to noise ratio for this matrix; For this purpose, two different spectra were obtained.

The first one (Figure 4.19) belongs to Barium 133 source, and 50000 events were taken. On the left part, one can see that the whole matrix is able to find seeds (obviously, except the masked pixels), so the whole matrix is active.

The second one (Figure 4.20) belongs to Cadmium 109 source, and, again, 50000 events were taken. On the left part, one can see again that the matrix is working. Nevertheless, the matrix could find less seeds in comparison with the Ba133 because this source has a lower activity.

Using this two spectra, the Gaussian fit of both peaks give the following results:

- Ba-133 (30 keV)⟶Mean Value=266 ADU (SNR (MIP[1])=86)
- Cd-109 (22 keV)⟶Mean Value=183 ADU (SNR (MIP)=81)

[1]Supossing that 1MIP creates 22300 pairs e^-h in 285 μm of Silicon

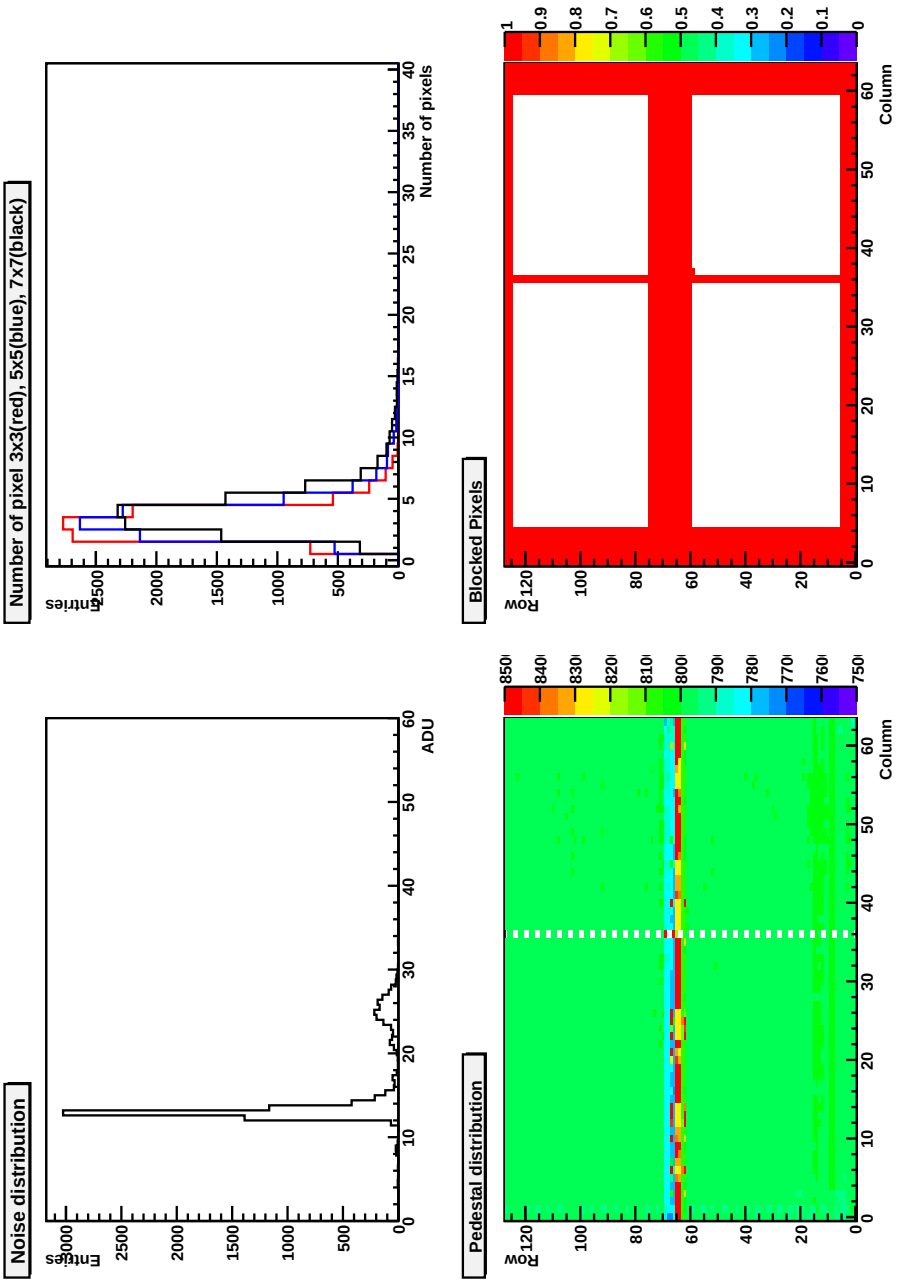

Figure 4.18: *Performance of the PXD5 matrix. Plots of main characteristics (noise, cluster size and pedestals) are shown. The map of the masked pixels (in red) is also shown.*

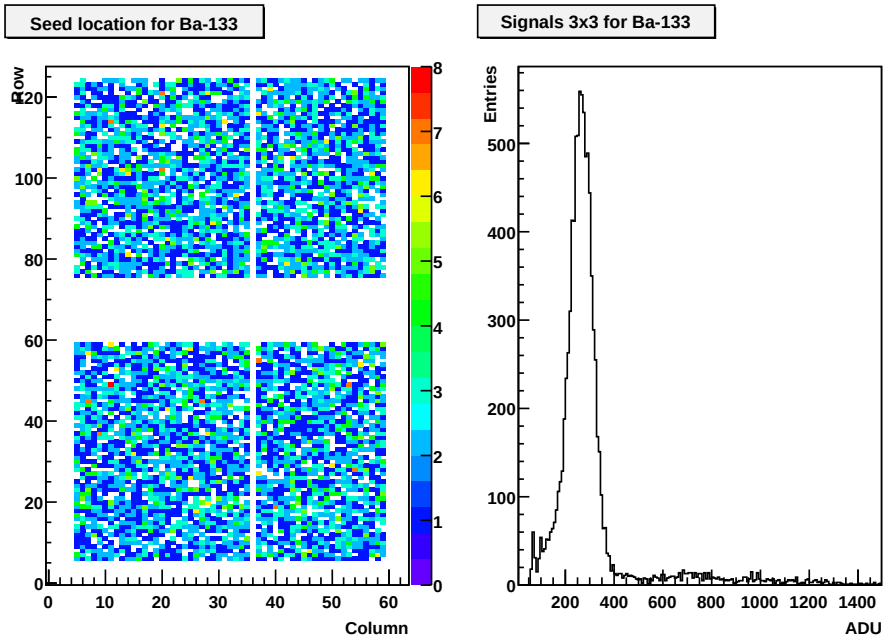

Figure 4.19: *Spectrum of Ba-133.*

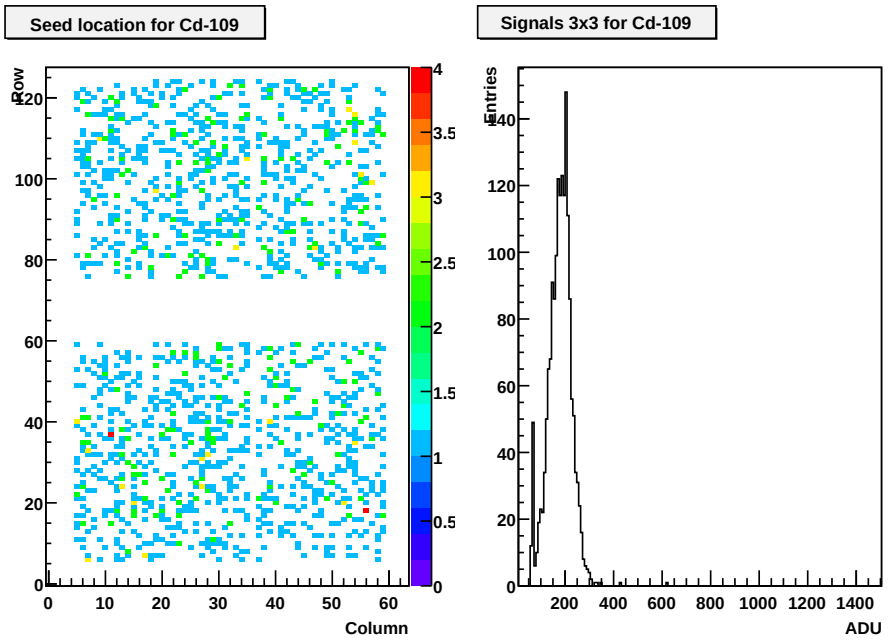

Figure 4.20: *Spectrum of Cd-109.*

Fitting this two point to a straight line, one can obtain that the gain of the system (given by the slope of the line) is ∼10 ADU/keV.

As in the previous generation, the g_q factor (the gain of the system) can be also calculated (Eq. 4.3) using this conversion factor, and is found to be 20% lower than in the PXD4 case.

$$g_q = \frac{10\ ADU}{1\ keV} \cdot \frac{7.7\ nA}{1\ ADU} \cdot \frac{3.6\ eV}{1\ e^-} \sim 277\ pA/e^- \tag{4.3}$$

4.4 Simulation of a CCG matrix using a CLG generation

Because of speed requirements and simplicity, the CLG (Clocked Cleargate) clear scheme was abandoned in favor of CCG (Common Cleargate). In order to have an impression of the performance of the new clear mechanism before the PXD5 production was prepared, a *CCG like* matrix was simulated using the CLG scheme, in two different ways: by voltage (by making equal the values of Cleargate High and Cleargate Low) and by sequence (by suppressing the Cleargate High signal) (see next sections for details).

4.4.1 Voltage simulation

This first option includes the supresion of the Cleargate High pulse when the Clear voltage is applied, just by making equal the Cleargate High and Low voltages ($V_{Cleargate_High} = V_{Cleargate_Low}$). The results shown here belong to a laser scan over a random selected area in the matrix, containing 21x21 points with a distance of 3 μm between them and containing 48 samples per point.

Nominal voltages

In order to be able to compare the results of the simulation, the matrix was first operated using the nominal voltages found in the optimization procedure (Table 4.1), with $V_{Cleargate_High} = 9\ V$ and $V_{Cleargate_Low} = 6\ V$. The results are shown in Figure 4.21. The plot on the left side shows the total amount of charge collected in a cluster 3x3, normalized to the mean charge of all the points taken during the scan. As can be seen, the charge collection is quite uniform and charge losses are not observed. In the right plot, the charge collected on the seed normalized to the total cluster charge is shown. In this case, the pixel structure is revealed, with the red spots corresponding to the gate contacts of the pixels surrounded by the blue regions with the clear contacts.

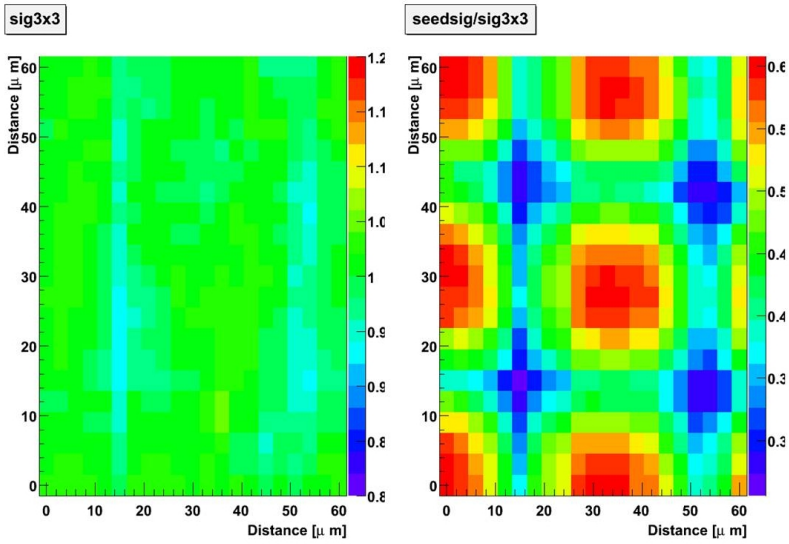

Figure 4.21: *Result of a laser scan over a CLG matrix using standard voltages. The plot on the left side is the charge collected on each point, normalized to the mean value of the distribution. Is clearly visible that the charge is uniformly collected all over the area. The right plot shows the charge collected on the seed divided by the charge of the cluster. The total fraction of the cluster charge that is collected by the seed gives an idea of the charge sharing. If the result of this fraction is high, the charge sharing is also high. The pixel structure is also visible. The center of the pixel (red color), collects the 60% of the total cluster charge while if the laser illuminates the pixel boundaries the charge sharing increases, and only half of this fraction is collected.*

$V_{Cleargate_{High}}$=9 V; $V_{Cleargate_{Low}}$=9 V

In this case, the Cleargate Low voltage was increased up to the same level of Cleargate High, so although the Cleargate contact is voltage pulsed, the matrix will see no differences between the upper and lower pulse levels. The results of the laser scan are shown in Figure 4.22. In this case, the pixel structure is still clearly visible (right plot) while (left plot) the collected charge seems to be a bit worse than in the nominal case, with some blue areas (meaning less collected charge in a cluster 3x3 pixels) on the plot. In this case, the positive voltage applied to the Cleargate during the charge collection phase seems to compete with the internal gate and some charges move to this contact instead of underneath the transistor's channel, resulting in a loose of charge in some regions around the clear and cleargate.

$V_{Cleargate_{High}}$=6 V; $V_{Cleargate_{Low}}$=6 V

Another option to simulate a CCG scheme but trying to keep the charge collection high could be to reduce the Cleargate High voltage to the same level of Cleargate Low, with $V_{Cleargate_{High}} = 6\ V$ and $V_{Cleargate_{Low}} = 6\ V$. The result is shown

in Fig 4.23. In this case, the Cleargate contact, because of the small value, does not compete with the internal gate during the charge collection step, but the clear phase falls only upon the Clear High pulse that is not able to swept away all the charges collected, resulting in an incomplete clear of the pixels. The behavior of the matrix is unpredictable and this mode can not be used to operate the system.

Summary CCG Voltage simulation

To summarize the results:

1. Clocked Cleargate
   - Signal $\longrightarrow$ 1131 ADU
   - Noise $\longrightarrow$ 14.6 ADU
2. Common Cleargate Voltage $V_{Cleargate_{High}} = 9\ V$ and $V_{Cleargate_{Low}} = 9\ V$
   - Signal $\longrightarrow$ 1078 ADU
   - Noise $\longrightarrow$ 16.6 ADU
3. Common Cleargate Voltage $V_{Cleargate_{High}} = 6\ V$ and $V_{Cleargate_{Low}} = 6\ V$
   - Signal $\longrightarrow$ 588 ADU
   - Noise $\longrightarrow$ 16.8 ADU

According to these results, is clearly visible that the right choice of the Cleargate voltages is crucial for the operation of the matrix. If the Cleargate voltage is too low (6V for example) the system jumps into an incomplete clear operation (the Clear pulse is not capable to remove all the charges by itself alone) and the matrix is by far, not in the optimal working point. By fixing the Cleargate voltages to higher values, a working operation point for the matrix near the optimal one is recovered. Nevertheless, although the signal (using 9 V on the Cleargate contact) is close the the one collected in the optimal point, the higher noise lead to conclude that the performance is not the best achievable. The explanation can be that even in this more favorable situation, either the clear is yet incomplete and part of the not cleared charge in the internal gate contribute to increase the noise levels or either the cleargate competes with the internal gate in the charge collection phase.

4.4.2 Sequence simulation

The system elements are monitored by a software control, called DAQ. In this tool, the decision when to apply each of the supply voltages to the matrix, Switchers and CURO can be controlled. When the DAQ is launched, the configuration files are sent to the different elements and the matrix is read row by row, as explained

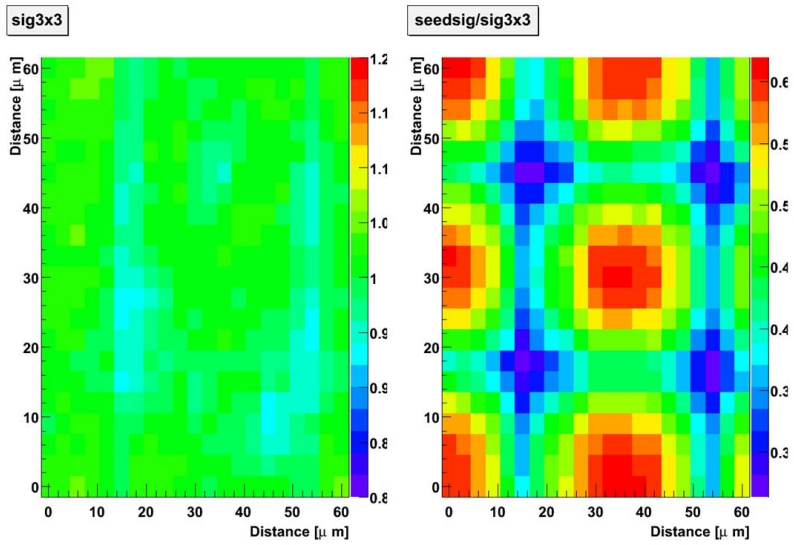

Figure 4.22: *The same area as in Fig. 4.21 was scanned but raising the Cleargate Low voltage up to the same value of Cleargate High. Similar results as in the nominal case were obtained, but a lower charge collection was found in some areas (blue areas on the left plot). The pixel structure is also visible in the right figure.*

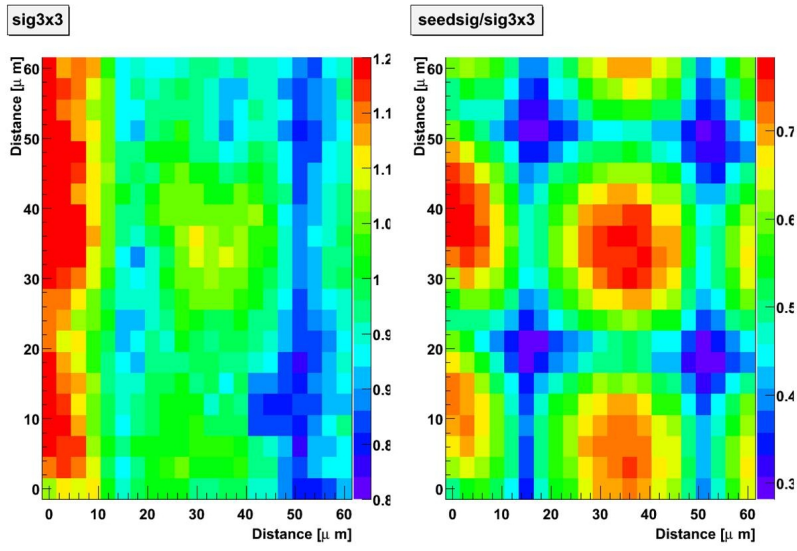

Figure 4.23: *This figure is equivalent to the Fig. 4.21 but the Cleargate High was lowered instead of increasing Cleargate Low ($V_{Cleargate_High} = 6V$; $V_{Cleargate_Low} = 6V$), resulting in an incomplete clear. In this case, the charge collection is not uniform anymore, resulting in an unpredictable behavior and this option should be abandoned.*

before. This way, the integration time of each row can be modified, the clear step can be delayed or simply suppressed and the voltages are applied (or not) when desired. This second simulation took into account this fact, and the Cleargate High signal was removed from the sequence, and only Cleargate Low voltage was used all the time.

Supressed Cleargate High and $V_{Cleargate_Low}$=9 V

In this first test, the Cleargate High, as was already said, was suppressed in the sequence and the Cleargate Low voltage was set to 9 V. The results are shown in Fig. 4.24. The results are similar to the ones obtained in the voltage simulation, with a pretty smooth charge collection all over the area, but showing also some trenches (light blue) where less charge was collected. The reason, once again, is that the potential of the Cleargate is too high that some electrons tend to migrate directly to this contact instead of to the internal gate.

Supressed Cleargate High and $V_{Cleargate_Low}$=6 V

Common Cleargate scheme just ask for a constant potential applied to that contact, but no boundary conditions are established to the voltage to be set. For this reason, a constant voltage of 6 V was applied to the Cleargate Low contact, and the results can be seen in Fig 4.25. As happened in the voltage simulation, the matrix is working under an incomplete clear mode; less charge is collected and the behavior is erratic and unpredictable, making this operation mode impossible.

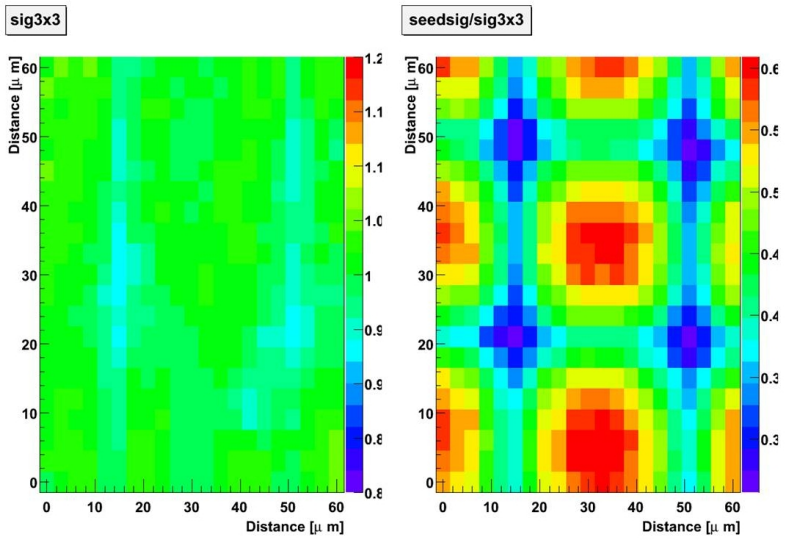

Figure 4.24: *The CCG matrix is now simulated just by removing the Cleargate High signal in the readout sequence. This figure is equivalent to the Fig. 4.21 but the Cleargate Low was set to 9 V, and the result is similar to the voltage simulation.*

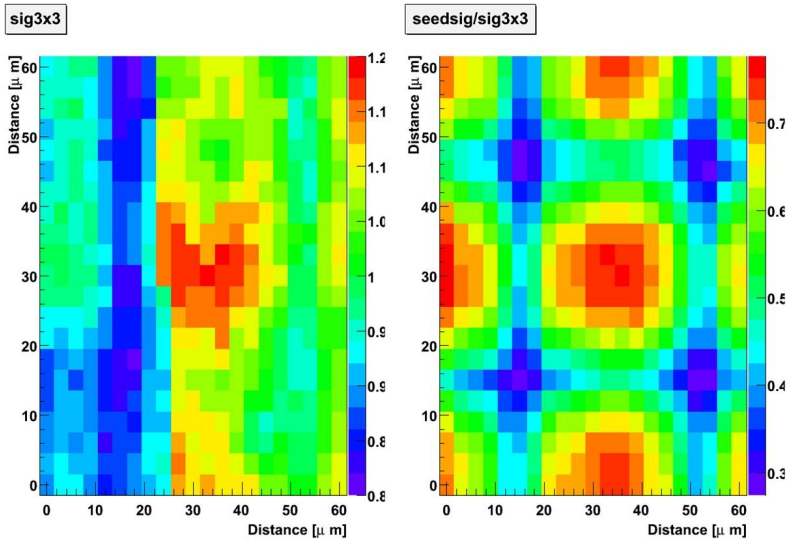

Figure 4.25: *In this case, the Cleargate Low was fixed to 6 V and the Cleargate High voltage was removed from the sequence.*

Summary CCG Sequence simulation

To summarize the results:

1. Clocked Cleargate
   - Signal $\longrightarrow$ 1131 ADU
   - Noise $\longrightarrow$ 14.6 ADU
2. Common Cleargate Sequence $V_{Cleargate_Low} = 9\ V$
   - Signal $\longrightarrow$ 1211 ADU
   - Noise $\longrightarrow$ 14.6 ADU
3. Common Cleargate Sequence $V_{Cleargate_Low} = 6\ V$
   - Signal $\longrightarrow$ 696 ADU
   - Noise $\longrightarrow$ 16.13 ADU

Analyzing these numbers, if the Cleargate Low voltage is not high enough, the internal gate can not be completely cleared of charges what results in an incomplete clear with a small signal collected and a high noise. If the Cleargate Low voltage is set to the optimal value, both configurations (CLG and CCG) obtain the same results, with a high amount of signal collected and with a moderately low and constant noise levels which gives confidence that the signal is completely cleared from the internal gate. The main conclusion is then, that a matrix with a CCG clear scheme and optimized voltages can deliver the same results as a CLG, but faster and with less complexity. An intermediate solution could be a CCCG (Capacitive Coupled Cleargate) configuration giving a CLG performance while keeping a CCG system complexity.

Chapter 5

Beam tests

Put such a delicate device in a beam and you will ruin it...

Old comments about the SLC detector. Book of appointments C. Damerell.

Tests under beams are complementary proves of the performance shown by the DEPFET sensors in the laboratory. These tests, produced with particles with defined characteristics (particle type, energy, beam intensity) give complementary information to the obtained in the laboratories, like the single point resolution. For this purpose, the DEPFET collaboration organized several test beams using 6 GeV/c electrons (DESY, Germany) and 120 GeV/c pions (CERN, Switzerland) in the campaigns started more than 5 years ago. In this chapter, the main results obtained during the 2008 campaign at CERN are shown.

5.1 Test beam setup

The test beam setup is shown in Fig 5.1. The telescope, used to reconstruct the tracks, is formed by five DEPFET planes, divided in two arms. Each sensor has 64x128 pixels running in a CCG clear mode. The pixel size is 32x24 μm^2, resulting then in a total size of $\sim$2x3 mm^2 and the matrix thickness is 450 μm. In between the two telescope arms, the DUT (Device Under Test) is mounted on a rotating motor-stage that allows rotations perpendicular to the beam axis. Several modules were tested and, although all of them are 450 μm thick, have different pixel sizes and layouts. All the modules in the beam test have been fully pre-characterized using lasers and radioactive sources and the electrical settings optimized for the best performance. The first and last elements, enclosing the set up, are scintillators for beam finding and, the AND logic signal between pulses in both scintillators, triggers the system. The trigger synchronization is made via a TLU (Trigger Logic Unit) [49], that accepts signals from the scintillators or a external trigger and generates a signal to trigger the system. Each trigger carries

a unique number and time stamp. The control and monitoring of the full system is done remotely via a Linux based DAQ. The system allows for an online data processing (pedestal and noise calculation, common mode correction), called DQM (Data Quality Monitoring) that serves to control the quality of the run and detect possible problems during the data acquisition.

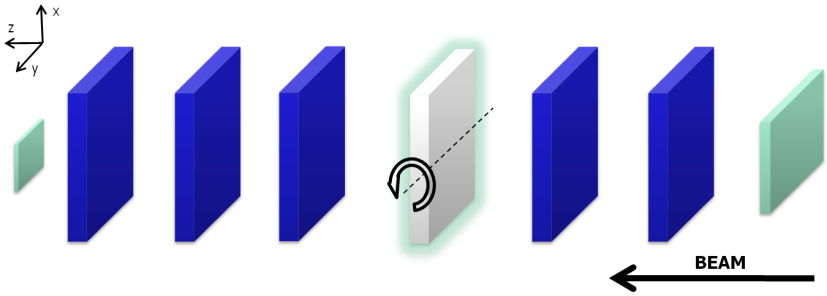

Figure 5.1: *Schematic view of the test beam setup. The DUT (Device Under Test) is placed between the two telescope arms, in a motor-stage that allows rotations perpendicular to the beam axis. The system is triggered by two small scintillators at both ends. The synchronization of the full system is done using a TLU (Trigger Logic Unit).*

5.2 Results

During the 2008 test beam campaign in the H6 line of the SPS complex at CERN, more than 20 million of events (3.5 TB of data) were taken in a period of 3 weeks, using 120 GeV/c pions. The off-line data analysis was done using the EUTelescope [50], the framework developed by the EUDET collaboration [51] using the standard analysis tools and reconstruction software used by the ILC community. This framework uses Marlin [52] (Modular Analysis and Reconstruction for the LINear collider, that is the execution framework), LCIO [53] (the I/O format and the data model), GEAR [54] (for the geometry description), LCCD [55] (to handle pedestals, noise and alignment constants), RAIDA [56] (for histogramming) and Millipede-II [57] (for alignment). The analysis road map is shown in Figure 5.2.

5.2.1 Raw Data Reader

The event reconstruction chain starts with the format converter. This processor converts the native raw DEPFET format (.dat) to the standard LCIO (Linear Collider Input Output) raw format, with the proper event structure and the correct event model. The run file starts with the description of the setup and the proper run number. After the beginning of the run event (BORE), the ADC information recorded on each pixel of the telescope modules and the DUT is written on the file. Finally, the end of the run is marked with a stream (EORE or end of run event). After this first step, no new information or histogram is produced.

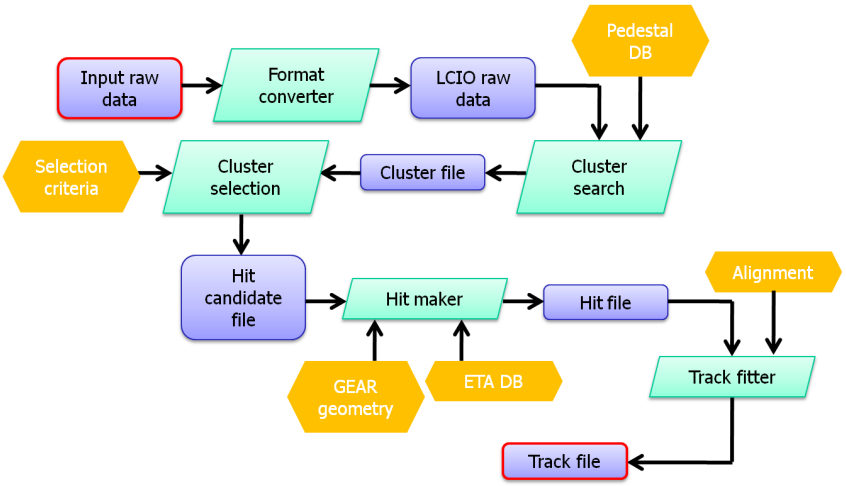

Figure 5.2: *Schematic view of the overall analysis strategy. The diagram shows the steps to follow to obtain tracks starting from the raw data extracted from the detector.*

5.2.2 Pedestal Noise Processor

In this step, a calibration of the output of each pixel detector is done in order to remove the constant and useless signal. The raw signal (t_k^i) of a non-zero suppressed event i in the detector channel k contains the signal (s_k^i, coming from the physical collected charge and random noise), the pedestal (p_k^i, a pixel specific offset) and the common mode (c^i, a common correlated noise specific for the pixels laying on the same row) (Eq. 5.1)

$$t_k^i = s_k^i + p_k^i + c^i \tag{5.1}$$

In order to determine the pedestal for the channel k, the mean value is extracted from the signal suppressed raw values using the first N events of a run (typically N=1000, in this analysis):

$$p_k = \frac{1}{N}\sum_{i=1}^{N}(t_k^i - s_k^i) \tag{5.2}$$

Pixels whose pedestal or noise is found to be very high or low with respect to the average value calculated for the whole matrix can be masked as *bad pixels* and excluded from the analysis. In this analysis, the pedestals are calculated for each run and assumed that the their values are constant over that time (Fig 5.3). The mean value of the pedestal distribution is ∼8100 ADU and is quite homogeneously distributed all over the pixels of the matrix, with a pedestal spread lower than ∼20 ADU. Because the FPGA is equipped with ADCs with 16 bits of resolu-

tion (thus 2^{16} quantization levels), having the pedestals on such level, guarantees enough dynamic range to digitize the deposited charge without being saturated.

The noise has two components, a random variation and a row-wise correlated variation, the common mode noise. This second component is generated by variable causes and has to be corrected for, after the pedestal correction and hit rejection (pixels with signal charge are excluded for the calculation). The noise map is shown in Fig. 5.4 (upper figure) and using the noise distribution, the mean noise value was found to be 12.5 ADU (∼260 e^-, using the conversion factor between the ADC counts and electrons found in the previous chapter), very stable along the matrix. This noise level is fully compatible with the one found in the characterization stage done in the laboratory with lasers and radioactive sources. Looking at Fig. 5.4 (lower plot), by comparing the black (before common mode correction) and the red curves (after common mode correction), is visible that the common mode noise contribution is found to be 15 ADU.

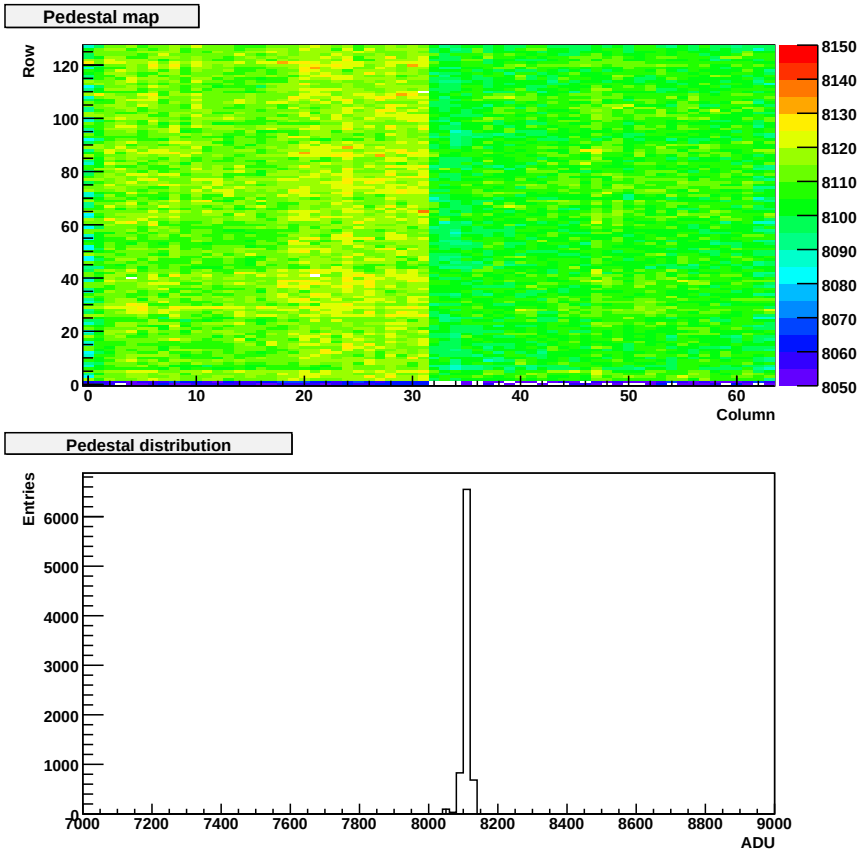

Figure 5.3: *Pedestal map (upper plot) and distribution (lower plot) over the matrix. An homogeneous pedestal value distribution of ∼8100 ADU is found and will be corrected from the raw signal.*

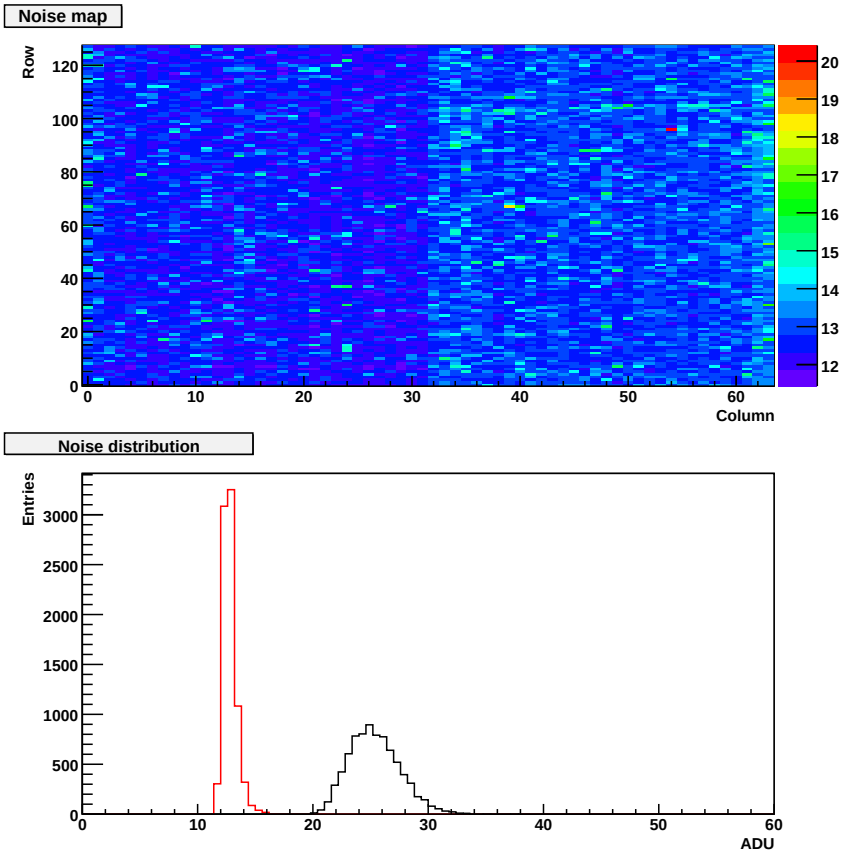

Figure 5.4: *In the noise map distribution (upper plot), is clearly visible that the noise is quite uniform on each pixel of the matrix. In the lower plot, a comparison of the noise before (black curve) and after (red curve) the common mode correction is shown. This correction reduces the noise from ∼29.5 ADU to a final value of 12.5 ADU (∼260 e^-).*

5.2.3 Cluster Finder

Once the common mode and the pedestals are known, for events $i > N$, the signal charge (the signal collected in the internal gate due to the impinging particles) for every channel k can be extracted as follows:

$$s_k^i = t_k^i - p_k^i - c^i \tag{5.3}$$

Once the signal and the noise levels are known for each pixel, the next step is to find along the matrix the channels with the highest signals, above a certain (and trimmable) threshold (t_{seed} or *seed cut*, n_n times the noise on that pixel (σ_{seed})), in order to start the cluster reconstruction:

$$s_{seed} \geq t_{seed} = n_n \cdot \sigma_{seed} \tag{5.4}$$

This step allows to identify if all the pixels within the matrix are capable to collect charge, just looking at the hit-map. Fig. 5.5 shows the times that a pixel in the matrix was found as a cluster seed along the run, while looking for signals that are above 7 times the noise of each pixel. The homogeneous hit-map shows an uniform illumination with no dead pixels or bad readout channels. The uniform illumination also serves to conclude that the DUT is centered with respect to the beam; if it was displaced, in this picture areas with higher number of hit pixels would be found. In Fig. 5.6, the seed signal distribution is shown in the curve filled with red strips. The mean charge collected in the seed pixels by the impinging 120 GeV/c pions is found to be around 1000 ADC counts, but signals between 500 and 1500 ADC counts were also found.

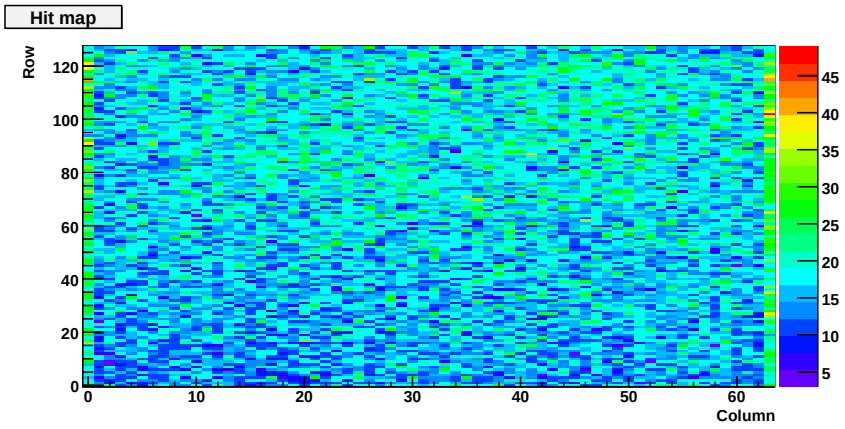

Figure 5.5: *Hit-map. An homogeneous illumination is achieved, with no dead areas in the matrix.*

After the selection of the seed pixels, a cluster is reconstructed around them, looking for pixels with a signal above a certain (and trimmable, once again) threshold ($t_{neighbour}$ or *neighbor cut*, n_m times the noise on that pixel ($\sigma_{neighbour}$)) in a window 3x3 or 5x5 around the seed:

$$s_{neighbour} \geq t_{neighbour} = n_m \cdot \sigma_{neighbour} \tag{5.5}$$

The selection of only fix squared windows (NxN pixels) around the seed can be modified arbitrarily depending on the specific geometry. In this case, the particles will come into contact with the matrix in a perpendicular way but at higher angles, elongated clusters will be found (NxM pixels) instead of squared ones.

In order to perform a good clustering some cuts were applied in the code. Only frames with a low number of hits were used for the clustering (typically 5 or less)

and the seeds of the clusters have to be well separated, just to avoid the inclusion of a close second seed pixel in the cluster of a neighbour one. Because the cluster algorithm needs to look for pixels in a window of NxN pixels around the seeds, the pixels laying on the border of the matrix were excluded in the clustering procedure.

The charge deposition obtained for the signal collected in a cluster is described by a Landau distribution, shown in Figure 5.6. The most probable deposited charge of a MIP in a 3x3 cluster is 1710 ADC units (using $7\sigma_{seed}$ and $2\sigma_{neighbour}$ cuts). Combining this value with an average noise of 12.5 ADC units, the signal over noise ratio (SNR) is 136 for a DUT of 450 μm ($g_q \sim 360\ pA/e^-$).

The signal collected in a 3x3 cluster is almost the same to the one collected in a 5x5 cluster, thus is clear that the charge is collected in a small square with an area of 72x72 μm^2 around the seed pixel.

The Table 5.2 shows the main characteristics presented up to now for all the modules in the beam (telescope+DUT).

5.2.4 ETA Correction

Once the cluster is reconstructed, the most straightforward method to calculate the impact positions is the Center of Gravity (CoG). This method gives the hit position (x_{CoG}) weighting it in terms of the charge fraction (Q_k) in each k pixel belonging to the cluster:

$$x_{CoG} = \frac{\sum_k Q_k \cdot x_k}{\sum_k Q_k} \tag{5.6}$$

Nevertheless, this method, assumes that the position is a linear interpolation of the charge distribution between a pixel and its neighbor and this is not exactly true at small angles. Fig. 5.7 illustrates what happens at small incidence angles of the traversing particle, as happens in this case. If the particle pass through the detector exactly in between two pixels (Fig. 5.7 leftmost drawing), the same quantity of signal will be collected in the two pixels and the position will be correctly reconstructed on the border of the two pixels. The CoG will also reconstruct nicely the position when the particle hits just one pixel (Fig. 5.7 rightmost drawing) but the critical situation is present if the particle hits the edge of one pixel. In this case, some charge will be deposited in the neighboring pixel, resulting in a wrong reconstruction as can be seen graphically (Fig. 5.7 center). Therefore the relation between position and charge deposit is not linear, but it is a non-linear s-curve as shown in Fig 5.8.

The η-algorithm is a standard method widely used in case of small incident angles to calculate the center of the cluster. It is used as a non-linear interpolation between the two neighboring pixels in one direction of the cluster which have collected the highest signals (Q_{Right} and Q_{Left}). Is an approach [58] based on the fact that the probability to find the cluster center should be flat over the pixel surface. A certain region does not collect more cluster centers than another.

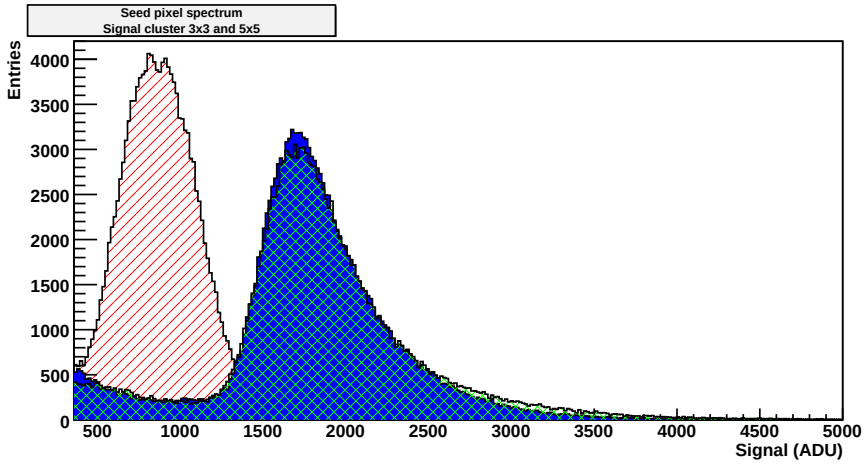

Figure 5.6: *Signal collected in a 3x3 cluster (blue), 5x5 (green squares) and the seed signal distribution (red strips). All the charge is collected in a small region, in a window not bigger than 3x3 pixels around the seed. The entries below the low signal tail of the Landau distributions are due to readout artifacts.*

	d0	d1	d2	d3	d4	d5
Pitch(μm^2)	32x24	32x24	24x24	32x24	32x24	32x24
Sig3x3(ADU)	1339	1497	1710	1715	1508	1654
Noise (ADU)	12.7	13.4	12.7	13.4	12.8	13.2
SNR	105	112	134	128	118	125
$\frac{SeedSignal}{ClusterSignal}$ (%)	69	56	59	61	63	64
ENC (e^-)	345	326	286	284	309	290
g_q (pA/e^-)	283	316	360	363	319	350

Table 5.1: *Main characteristics of the modules beam tested.*

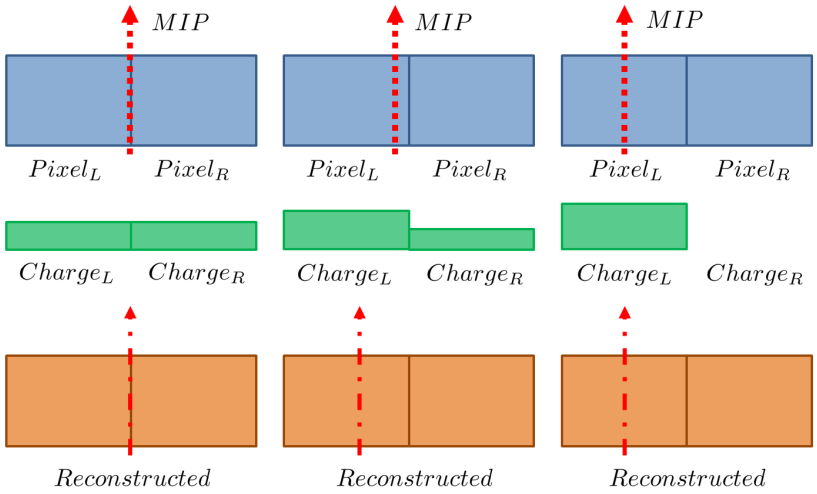

Figure 5.7: *Charge collected for particles passing at different positions in the pixel. The CoG can reconstruct the first and last situations, but in the central case, the position will be reconstructed close to the center of the pixel.*

The η correction is made in two orthogonal directions. The following quantity is calculated for each event:

$$\eta = \frac{Q_{Right}}{Q_{Right} + Q_{Left}} \tag{5.7}$$

A probability density function is then calculated:

$$f(\eta_0) = \frac{1}{N_0} \int_0^{\eta_0} \frac{dN}{d\eta} \mathrm{d}\eta \tag{5.8}$$

where N_0 is the total number of entries in the $\frac{dN}{d\eta}$ distribution, and η_0 is the η value for the considered event. The corrected hit position is then given by:

$$x_\eta = Pitch \cdot f(\eta_0) + x_{Left} \tag{5.9}$$

In Fig. 5.8 (upper part) the X projection of the cluster center distribution is shown before (red curve) and after (blue curve) the η correction. The cluster center distribution should be flat within the pixel and if it is not, the definition of the cluster center is corrected using a non-linear weighting function (lower part). The η correction is useful when the particle hits the detector at small incidence angles and is less effective at higher ones, where the charge will be shared between more than one pixels.

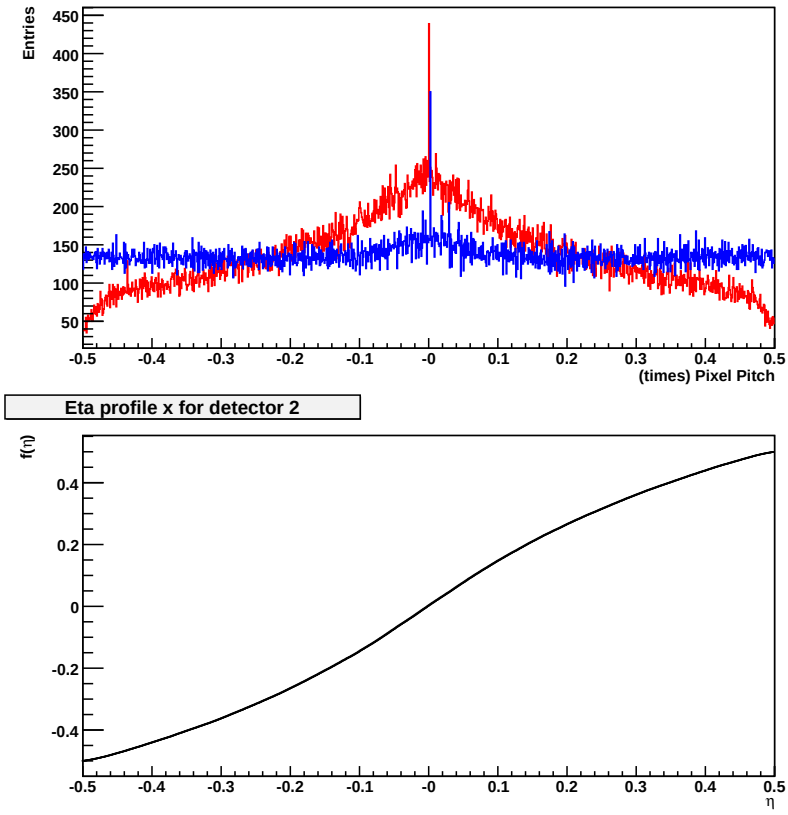

Figure 5.8: *(Up) X projection of the cluster center distribution using the center of gravity before (red curve) and after (blue curve) η correction. Because the pixel is homogeneously illuminated, there is no reason why the center of the pixel should reconstruct more events rather than the periphery so a non-linear relation between position and charge has to be implemented. (Down) A non-linear s-curve is introduced to establish such interpolation between charge and position (Eq. 5.8).*

5.2.5 Hit Maker

Once the cluster center is found, this has to be translated from pixel units in the detector frame of reference into hits, that are space points in the global telescope frame of reference (Fig. 5.9). In order to do that, this processor access the geometry repository, extracting the plane positions in the z direction (along the beam axis) and the pixel pitches from the GEAR file.

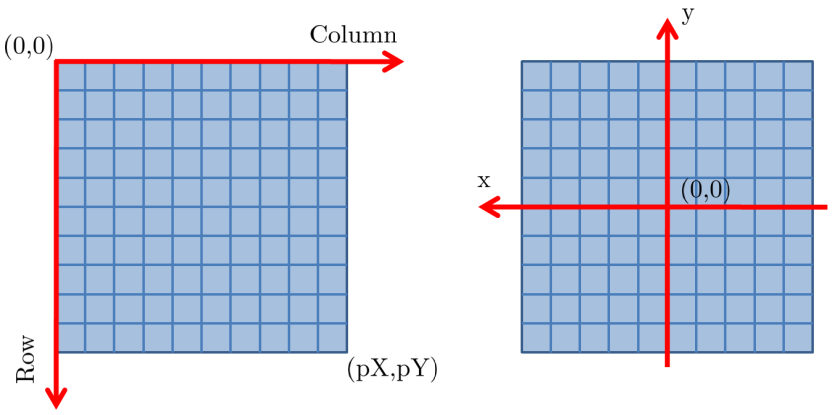

Figure 5.9: *In the Hit Maker step, the cluster center in the detector reference system (left) is translated into a hit in the global telescope reference system (right).*

5.2.6 Alignment

The most important sensor characteristic that can only be studied in a test beam is the intrinsic resolution. In order to calculate it, the reference telescope has to reconstruct the particle trajectories (using hits on the 5 modules) and interpolate the particle impact positions on the pixel sensor. Before tracks can be reconstructed, it is important to pre-align the sensors of the telescope and the DUT respectively. This first pre-alignment was done before the data taking, using the online DQM. The hit correlations between two of the telescope modules (as an example) are shown in Fig. 5.10.

When the pre-alignment procedure is over, the alignment using tracks is started, to obtain a more precise knowledge of the position of all the planes (telescope and DUT). The alignment consists on finding the translations (in X and Y directions, perpendicular to the beam line) and the rotation (around the beam line), that are needed to correct for on all the modules, to refer them to the same system of reference. These parameters, called *alignment constants*, are calculated minimizing the χ^2 of the straight line fit to the hits found in the telescope planes and in the DUT. The alignment constants are calculated using the EUTelMille processor that calls the global χ^2 fitter, called MillepedeII. MillepedeII loops over all events recorded

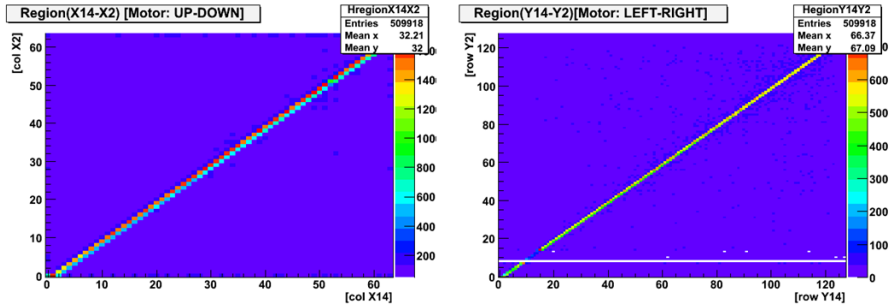

Figure 5.10: *Pre-alignment of the modules (telescope and DUT) before the data taking. The diagonal configuration shows that the same pixel shows a hit in both of the sensors in the same event.*

to find track candidates off-line and by considering a huge number of reconstructed tracks, the alignment constants can be extracted and the sensor positions can be corrected. The first and last planes of the telescope are fixed and the rest of the planes are iteratively aligned in terms of spatial translations and rotations. In this step, to avoid the combinatorial background when fitting the tracks, only frames with a small number of hits are processed and also the edges of the sensors are excluded from the fitting. The alignment constants (and thus the displacements to apply to the modules) were found to be in all the runs in the order of tens of microns, which confirms that the pre-alignment was done in a good shape and the modules were already aligned with less than a few pixels of difference.

5.2.7 Track fitter

Once the system is aligned, the tracking phase is entered. The most simple tracking can be done just by fitting the hits on the telescope modules to a straight line minimizing the χ^2 and relating this track to the hit appeared in the DUT. This first simple approach is far from reality because of the neglection of the multiple Coulomb scattering. A charged particle passing through one detector will change its direction with respect to the point of incidence because of the multiple Coulomb scattering with the nuclei inside of the sensor. The mean deflection angle of a 120 GeV/c pion over 450 μm of silicon is $\sim 6.3 \cdot 10^{-3}$ $mrad$ so, a deviation of ~ 1.3 μm is expected between planes at a distance 195 mm; this fact has to be taken into account when fitting the track.

The residual distributions are the shortest distance between the real hit and the extrapolated track on the DUT. If the hit in the DUT is used for the track fitting, the residual is called *biased* while if it is excluded, the residuals are called *unbiased*; thus, the biased residuals are always found to be smaller than the unbiased ones. The residual distributions measure the quality of the alignment: for a perfectly aligned detector the residuals distribution is a Gaussian curve centered around 0 and with a width determined by the intrinsic resolution of the detector.

To show the importance of the alignment before the tracking step, the residual distributions before (black line) and after (red line) the alignment are shown in Figure 5.11. A Gaussian distribution centered at 0 is recovered once the system is aligned after moving the module around 50 μm in X direction (in this case, as an example).

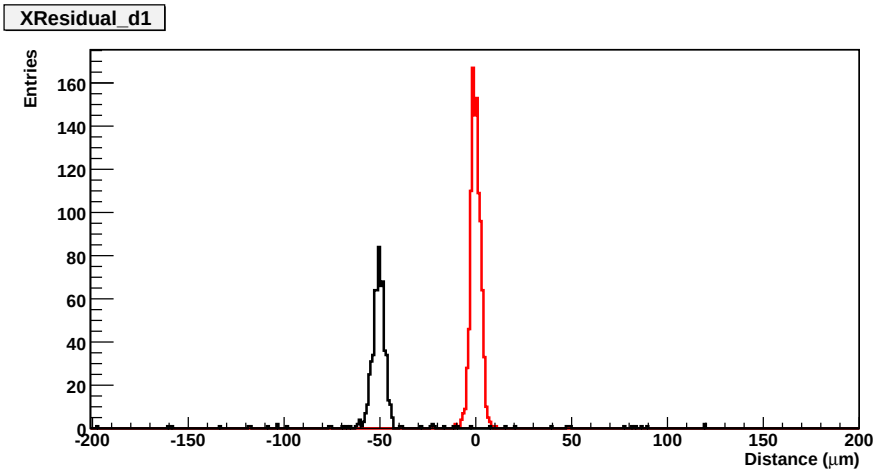

Figure 5.11: *The residual distributions in X direction before (black line) and after alignment (red line) for the second telescope module are shown to see the importance of the alignment. The σ of the Gaussian fit around 0, gives information about the resolution of the device.*

Element	X direction (μm)	Y direction (μm)
σ_{Total} (Module d2 24x24 μm^2)	4.15±0.16	2.8±0.15
$\sigma_{Telescope}$	3.63±0.13	2.11±0.10
$\sigma_{Multiple-scattering}$	0.71	0.71

Table 5.2: *The measured total unbiased residual contribution is shown. The DUT is excluded from the linear fit. The telescope and te multiple Coulomb scattering contributions are estimated using GEANT4 simulations.*

In table 5.2, the total unbiased residuals (excluding the DUT from the linear fit) obtained for the DUT are shown. This residuals are a convolution of the telescope resolution, the intrinsic resolution of the DUT and the multiple Coulomb scattering contributions, expressed in the following way:

$$\sigma^2_{Total} = \sigma^2_{Telescope} + \sigma^2_{Intrinsic} + \sigma^2_{MultipleScattering} \tag{5.10}$$

The influence of the multiple Coulomb scattering term to the total residual contribution can be seen in Fig. 5.12.

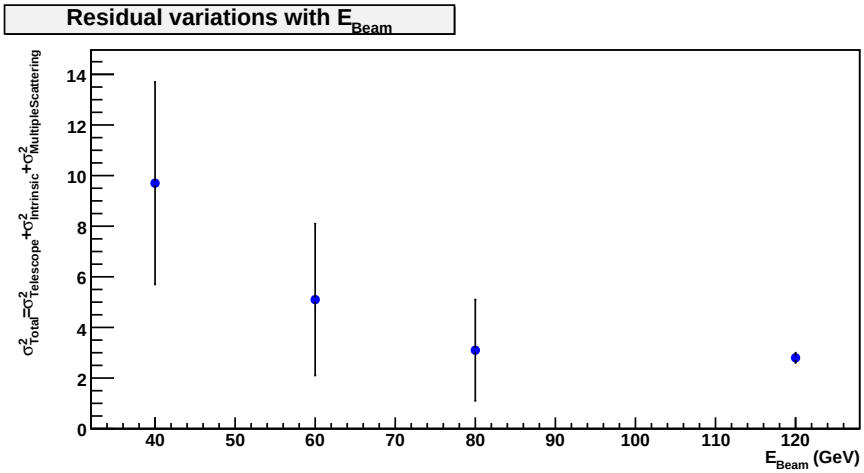

Figure 5.12: *Total residual distribution as a function of the beam energy scan. As the beam energy decreases, the multiple scattering term is getting bigger and bigger (the intrinsic and the telescope resolutions do not depend on the beam energy), degrading the residual distribution ($\sigma^2_{Total} \propto E^{-2}_{Beam}$). The large error bars on the low energies are caused by the low statistics achieved with those runs.*

Based on detailed GEANT4 simulations [59], both the telescope resolution and the multiple Coulomb scattering contribution can be estimated as shown in table 5.2; thus, the intrinsic resolution of the DUT (24x24 μm^2) can be estimated using the equation 5.10 and the contributions in table 5.2 as:

$$\sigma_x^{Intrinsic} = 1.88 \pm 0.60 \ \mu m \tag{5.11}$$

$$\sigma_y^{Intrinsic} = 1.69 \pm 0.36 \ \mu m \tag{5.12}$$

A problem found time after the test beam and that can degrade the resolution of the modules, concerns the XY motor-stages where the modules are assembled on. The positioning motor-stages presented a drift of several microns varying in time, so the position of the modules was not constant over the hole run. The results shown here correspond to a long run processed as a hole, so the numbers obtained are bigger than expected. Although this fact has to be taken into account for future test beams, another strategy could be to re-align (extracting the alignment constants each time) the system every a small number of events (10000 was found to be a trade off between stability and statistics [60]). In this case, better resolutions are achieved but, on the other hand, because of the lower statistics, the accuracy of each alignment is smaller.

5.3 Complementary studies

Although the most important objective in the test beam period was to establish the spatial resolution of the device, some complementary studies have been made.

In Fig. 5.13, the charge collected in a 3x3 cluster is shown for different pion beam energies, from 20 GeV/c to 120 GeV/c. As expected in this range [61], there is no charge collection variation, because at 20 GeV/c the pions are already minimum ionizing particles (MIP). Increasing the beam energy does not increase the energy deposited. This collected charge is under normal incidence of the pions, and the charge is also collected in a small region inside de matrix.

Although presented as one of the final results, the following measurement was done at the very beginning of the test beam to cross-check (with the voltages obtained in the laboratory during the calibration stage), that the matrix was properly biased. Thus the bias voltage was varied from 150 V to 220 V and the 3x3 cluster signal was obtained (Fig. 5.14). The charge collected is uniform in the whole range, so the fully depletion conditions are achieved at low voltages, and all the scanned values where yet on the plateau region.

Finally, the beam data have been also used to study the uniformity of the charge collection over the sensitive area. In Fig 5.15 (upper), the charge collected in a cluster 3x3 is plotted, while the matrix is being illuminated by the 120 GeV/c pion beam. The mean signal is collected on each pixel using 400 MIPs. As can be seen in the charge distribution (Fig 5.15, lower plot), the charge collected centered around the already mentioned 1700 ADU and is uniformly distributed all over the surface of the matrix, with a variation of less than 5%. The sensor is well behaved and the uniform charge collection observed while being illuminated by a laser in the optimization procedure in the laboratory, was also reproduced in the beam.

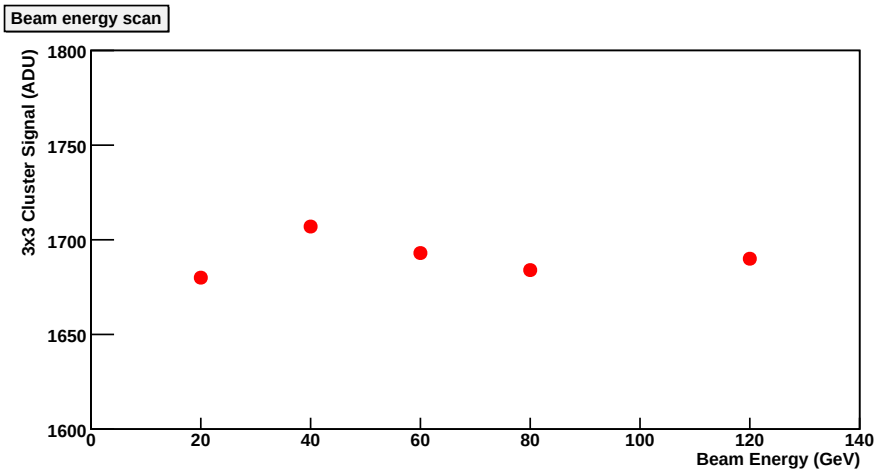

Figure 5.13: *Results of the beam energy scan using pions with energies between 20 GeV and 120 GeV. The charge collected in a 3x3 cluster is homogeneous in this range.*

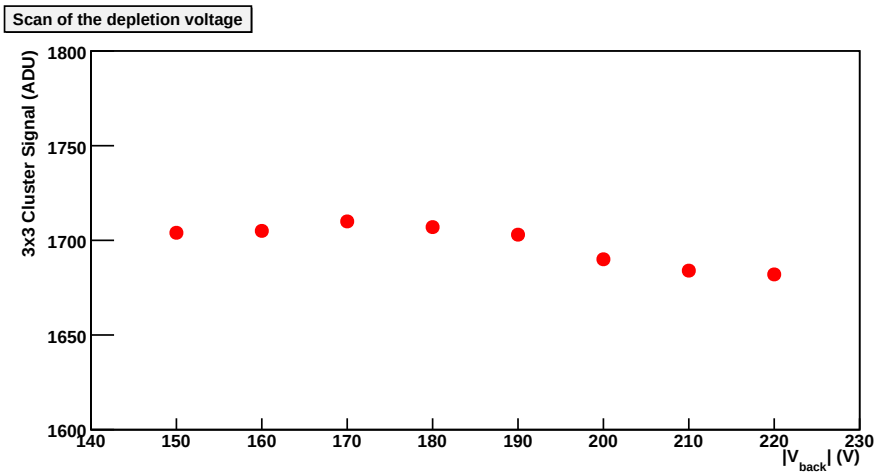

Figure 5.14: *Results of the charge collected in a 3x3 cluster using 120 GeV pions as a function of the backplane voltage. As can be seen, the sensor achieves the fully depletion at a low voltages (∼ -160 V), and after reached the plateau, the charge collection is uniform.*

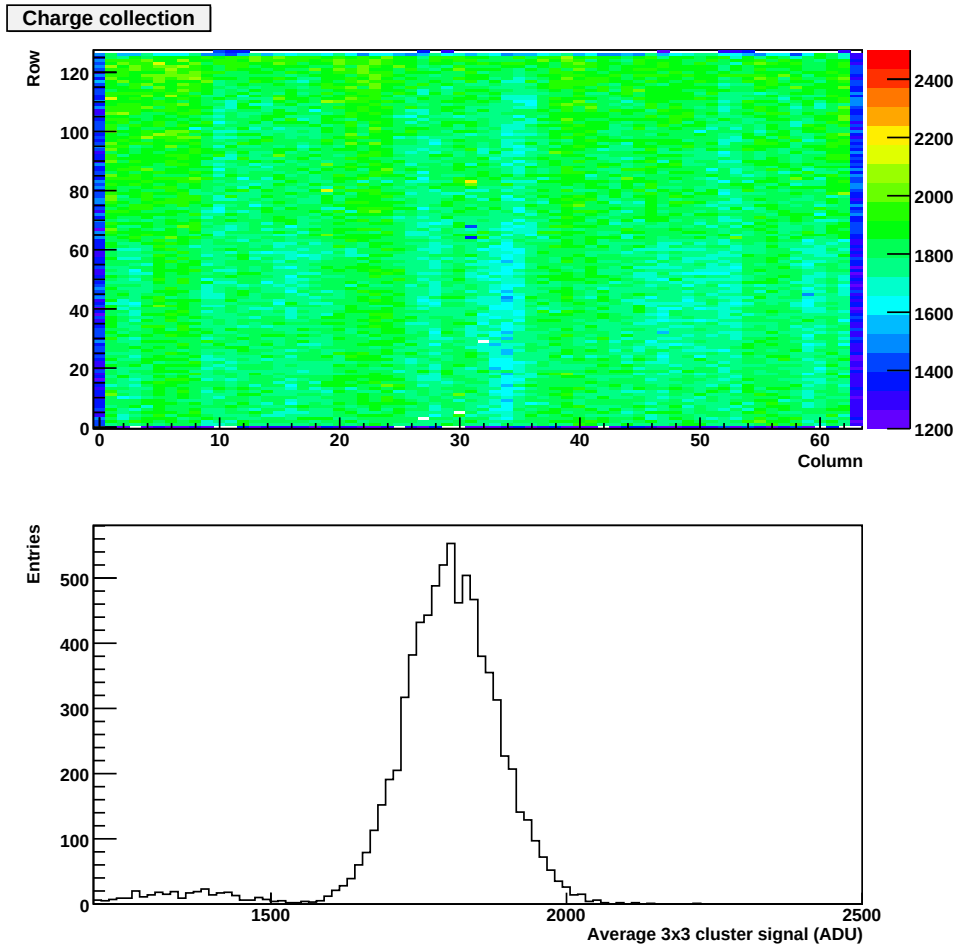

Figure 5.15: *(Up) Charge collection uniformity map using 3x3 cluster signals. The mean signal collected on each pixel using 400 MIPs is plotted. (Down) Charge collection uniformity mean distribution. The charge collected is uniform over the surface of the matrix, less than 5% of variation is observed.*

Chapter 6

Thermal studies for Belle-II

At room temp it would be easy, but given the need to run cold, the cryogenic problems will be insurmountable

Old comments about the SLC detector. Book of appointments C. Damerell.

6.1 Motivation

The beam energy assymetry in Belle-II causes that the interesting physics events are to be produced in regions of interest covering angles between 17° and 155°. The Vertex Detector has the cylindrical layout around the beam pipe presented in Chapter 3. The sensitive area of one ladder is placed in the central region, while the Switchers will lay on the lateral balcony and the readout chips (DCD and DHP) will be on the end of the stave. This arrangement has special importance when considering that no extra material (in the shape of cooling pipes) is allowed inside the acceptance region. As will be presented in the following sections, the strategy will be to cool the end of staves using massive structures outside of the acceptance, while the center of the ladders will be cooled by means of forced convection with cold air [62]. In this chapter, the evolution of the thermal studies is presented, from the very first measurements to the latest final simulations.

6.2 First steps

The first measurements towards the design of a cooling solution for the Belle-II detector, were made using a small microstrip detector (3.4x1.4 mm^2 and 300 μm thick). These first measurements were done to disentangle the conduction and convection contributions to this primitive cooling system (Fig. 6.1). A heater, a flat resistor made in copper over a polymide foil to simulate a chip, was placed in the middle of the sensor, to dissipate heat from it. The design and production

of the heaters was done at IFIC, and each one was fabricated *ad hoc*, with the specific geometry needed for each application: an array of thin and long heaters to simulate the switchers and a thicker one to simulate the DCD and DHP chips (see next section). A Pt100 resistance was glued on top of the system to measure the temperature. The detector was held in between of two aluminum blocks, cooled using the coolant coming from a chiller. The temperature of these structures can be selected over a wide range (from +20 °C to -20 °C). The air was provided for the first test, using a PC fan which can be regulated with a potentiometer. In further tests, the air was delivered by mean of an air pump with filters to remove the dust and humidity.

6.2.1 Conduction and convection disentanglement

Fig. 6.2 shows the evolution of the heater's temperature, for different temperatures of the cooling blocks, as a function of the power dissipated by the chip. The slope is the same in all cases, the only difference is the offset. The influence of the cooling block's temperature (conduction) in the center of the module is not so big; decreasing ∼20 °C the temperature of the coolant just entails a reduction of ∼8 °C in the heater placed in the center of the sensor.

Fig. 6.3 shows the evolution of the heater's temperature, for two configurations of the cooling blocks (in idle state and with circulating liquid at 15 °C), as a function of the speed of air for 0.4 Watts of dissipated power. In this plot, is clearly visible that a moderate air flow is an effective mechanism for cooling the center of the module. When the cooling blocks are cooled at a temperature of 15 °C, the temperature decreased a lot from free convection to $v_{air} = 1\ m/s$ but once the air is blowing, the temperature varied slowly, independently of the speed (at this range). If the conduction mechanism is switched off, the air has to compensate its loss and the plateau is hardly visible.

6.2.2 Power cycle

Because of the readout scheme of the Belle-II DEPFET ladder, the steering chips (Switchers) will be powered on sequentially to provide the gate and clear signals to the matrix rows, while the readout chips will all remain powered on all the time. The switchers, even in idle state (when not applying the clear and gate pulses), will have power consumption, although lower than when active. In the ILC, the behavior will be similar as in the Belle-II case while having collisions but the full system will be completely powered off in the period between trains, using this time to cool down completely all the ladder elements.

To evaluate the influence of the power cycling on the ladder, a set up similar to the one described in the previous section was used. In this case, the heater was sequentially powered on and off using a programmable power supply, and the evolution of the temperature was measured using a thermal camera [63]. The infrared camera measures and images the emitted infrared radiation from an

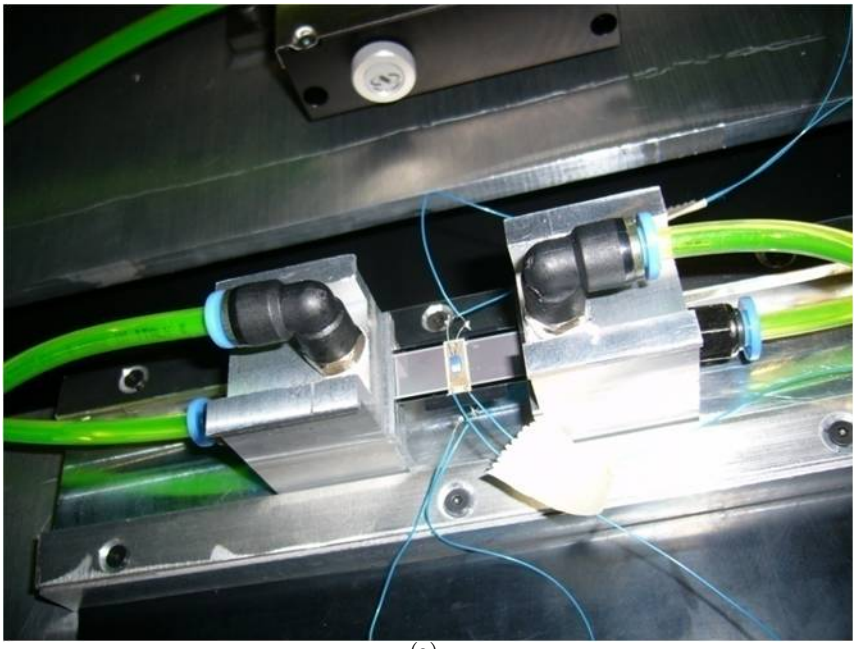

(a)

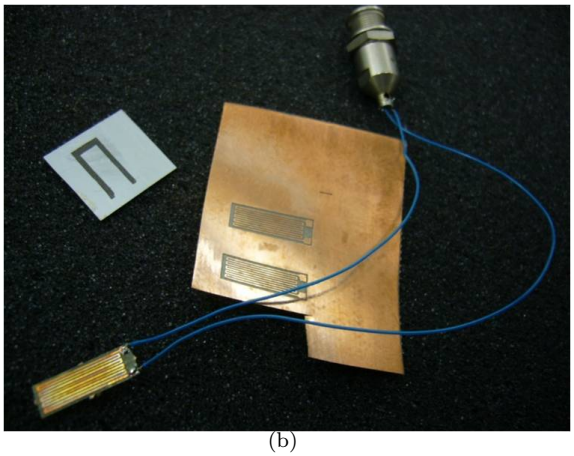

(b)

Figure 6.1: (*a*) *The first primitive set up consists on a couple of cooling blocks to hold a microstrip detector and provide cooling by means of conduction. The convection is performed with air in a speed range between 1.5 m/s and 6 m/s. A chip is simulated using a copper heater on polymide (b) on top of the silicon. A Pt100 resistor was glued on top of the system to register the temperatures.*

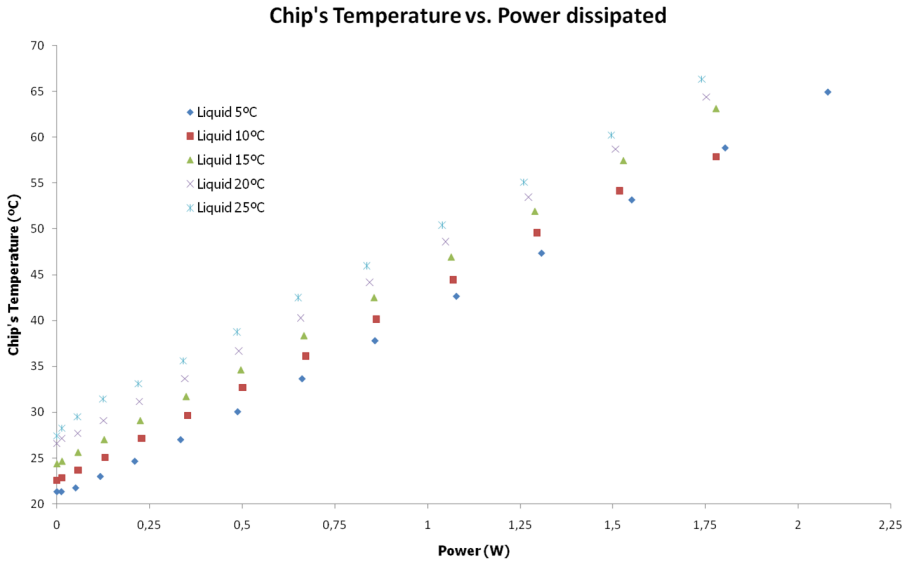

Figure 6.2: *The heater's temperature is shown as a function of the power dissipated for different temperatures of the cooling blocks. With these studies the contribution of the cooling by means of the conduction mechanism is studied.*

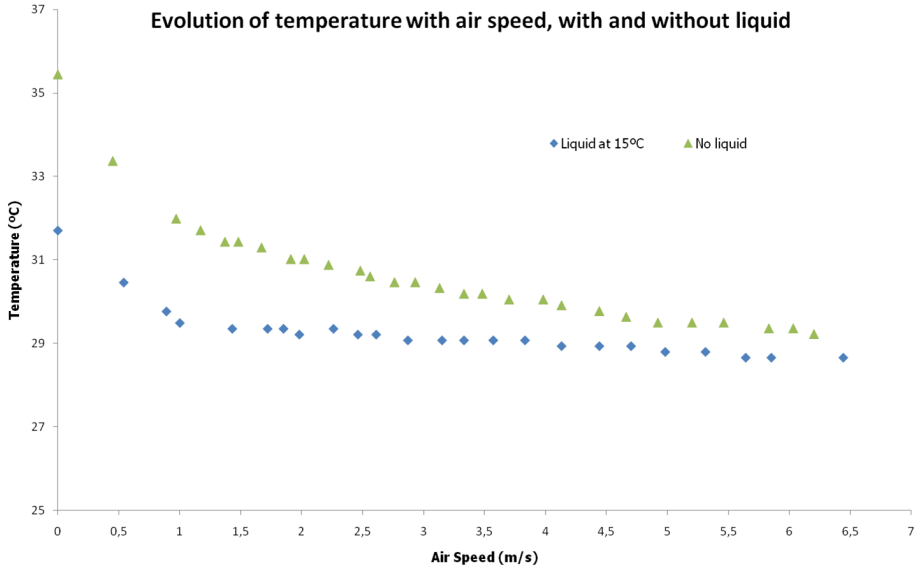

Figure 6.3: *The heater's temperature is shown as a function of speed of the air, with (diamonds) and without (triangles) conduction. With these studies, the contribution of the cooling by means of the convection mechanism is studied.*

object. Because of such radiation is a function of the object surface temperature, the camera can calculate then such temperature. The radiation that arrives to the camera lens depends on the emissivity (a measure of how much radiation is emitted from the object compared with a perfect blackbody with the same temperature), the distance between the object and the camera (part of the radiation will be absorbed in the atmosphere), and the reflected radiation emitted by other heat sources near the sample, and all these effects could be corrected for in the camera.

Fig. 6.4 shows the effect of the power cycling of the heater on the temperature of the sensor. A temperature plateau is always reached (Fig. 6.4 (*a*)), independently of the ON/OFF time. The final temperature is always the same, under the same cooling conditions. If the ON and OFF cycles are longer (Fig. 6.4 (*b*) and (*c*)), bigger oscillations around the equilibrium temperature are found. If the OFF state is longer than the ON one (Fig. 6.4 (*d*)), a plateau is also reached, but at lower temperatures.

In Fig. 6.5 the effect of the conduction and forced convection on the temperature plateau achieved with the power cycling is shown. As can be seen, the plateau is always reached after a certain time, but using cooling the value of this temperature is decreased. With no cooling (Fig. 6.5 (*a*)), the plateau is reached at 37 °C while if the convection mechanism is on (Fig. 6.5 (*b*)), the temperature can be decreased down to 30 °C. An extra reduction can be achieved opening the conduction channel (Fig. 6.5 (*c*)), obtaining the plateau at even lower levels of 28 °C. In this measurements was also shown that applying a power P in a pulsed shape (if $t_{Active} = t_{Idle}$) is equivalent to apply $\frac{P}{2}$ in continuous mode, and this fact will be used in the simulations. Fig. 6.5 (*d*) shows that the thermal RC of the silicon is high enough to see the thermal cycles applied. In the real experiment, the observed plateau will be shifted up because the Switchers, even in idle state, will have power consumption and there also will be another heat sources powered on near them, while in this case when in idle state the power consumption is zero.

As a curiosity, in Fig. 6.6 a thermal image of an *old* PXD4 (Clocked Cleargate) matrix is shown. The Clear Switcher, with 40 °C is the hottest point of the system, while the CURO and the Gate Switcher are at 36 °C and the matrix is at 32 °C (as expected because of the low power consumption of the technology). No cooling was applied in this case.

6.2.3 Support bars

The whole interaction region has to be designed carefully to be able to perform precision measurements and fully exploit the data produced. The performance of the pixel detector is also influenced by the beam pipe design and, because the later suffered major changes since the first geometry, the PXD also evolved during that time. As was already pointed out, the end of the stave will be chilled using massive cold structures outside of the acceptance. The location of these structures is defined by the beam pipe geometry, so their placement changed also in the same way as the beam pipe did. The first DEPFET detectors, made in an all silicon

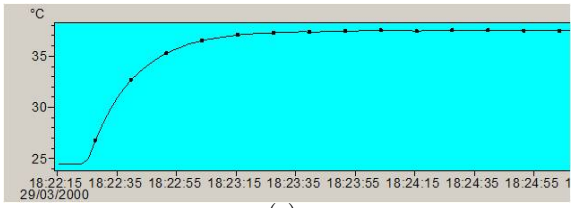

(a)

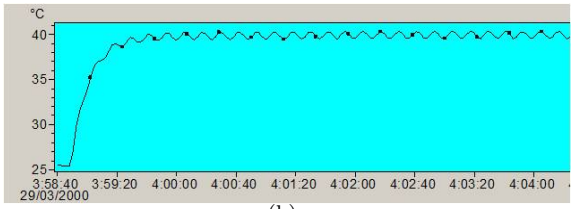

(b)

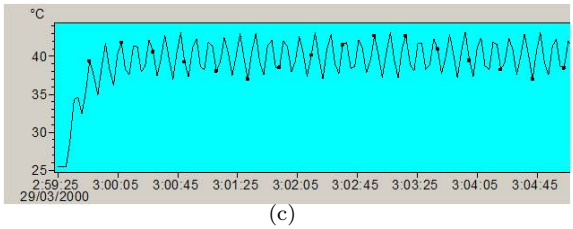

(c)

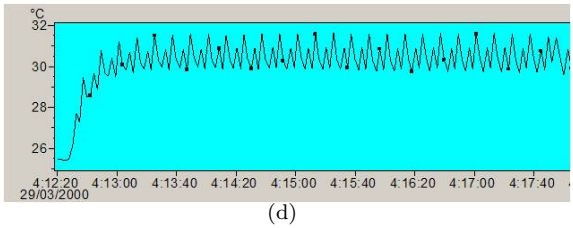

(d)

Figure 6.4: *Effect of the power cycle on the temperature for different ON/OFF cycle timing. In all the cases, with 1 W dissipated on the heater and no cooling, a plateau was always achieved around ∼40 °C, with bigger or smaller oscillations around this central value depending on the ON/OFF timing. (a) 0.1 s ON and 0.1 s OFF. (b) 1 s ON and 1 s OFF. (c) 10 s ON and 10 s OFF. In this case, the camera is slower rather than the ON/OFF cycle and could not follow the oscillation of the signal. (d) 1 s ON and 5 s OFF. In this case, a plateau was also reached, but at a lower temperature. This case is the most similar to the real detector, where the Switches will stay longer in an idle state.*

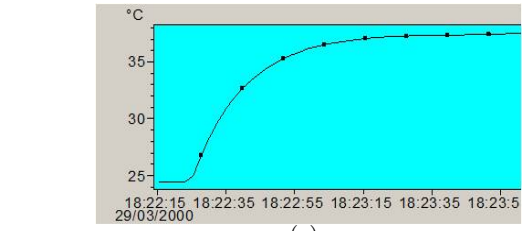

(a)

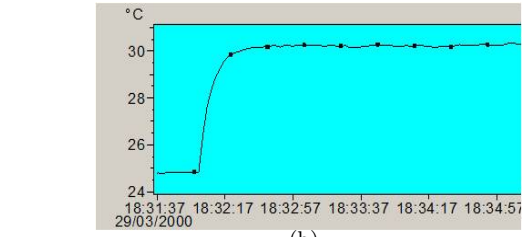

(b)

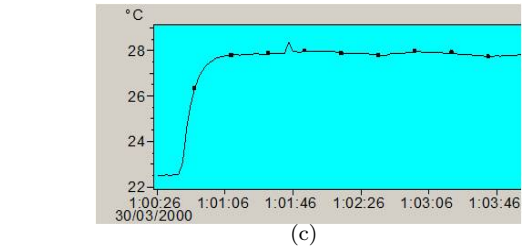

(c)

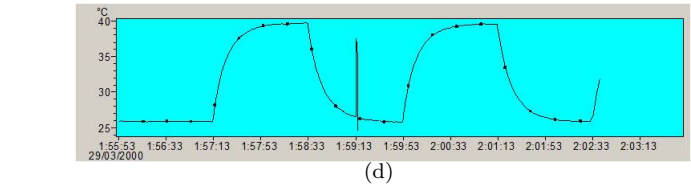

(d)

Figure 6.5: *Effect of the cooling mechanisms (conduction and forced convection) in the temperature plateau. In all cases, 1 W was dissipated and the heater was in a transient state with 0.1 s in ON and 0.1 s in OFF state. (a) With no cooling, the plateau temperature is 32.5 °C. (b) Applying forced convection with air at room temperature and v_{air}=5.6 m/s, the plateau temperature is 30.5 °C. (c) If an extra heat sink is opened with the cooling blocks at 15 °C, the temperature plateau is reduced to 28 °C. (d) Two heater power cycles are shown in this figure. Each cycle consists of 90 s.*

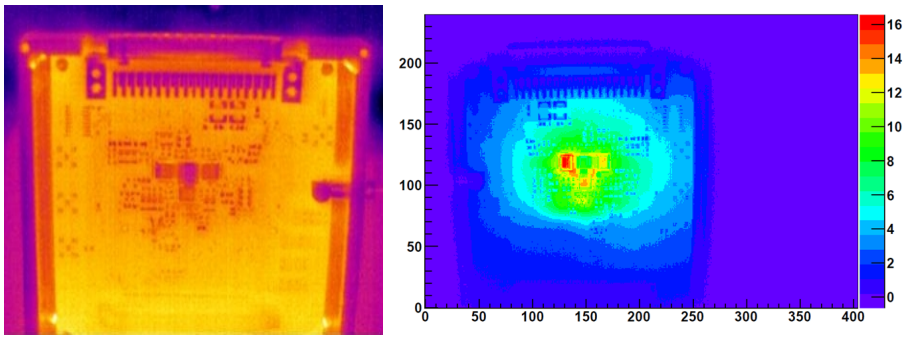

Figure 6.6: *Thermal images of a PXD4 matrix. (Left) Thermal image of the hybrid in OFF state. (Right) Difference with respect to the ambient temperature of the same hybrid. The hottest point is the Clear Switcher while the sensor is at a moderate temperature.*

single piece produced in 6 inches wafers, were not long enough to cover all the distance needed to reach the cooling blocks at both ends in the first design; thus extra elements would be needed to connect the ladders to the massive structures and to be used as a heat path between the ladder and the cooling blocks. The first studied support bars made on aluminum and copper were rejected because of the low thermal conductivities of those materials. The low thermal conductivity could be compensated, theoretically, with bigger thicknesses but this solution would displace the ladders from the nominal positions, making impossible its use. A new material was then tested, called TPG (Thermal Pyrolytic Graphite) [64], with a conductivity (theoretically) much higher than the mentioned materials. In Fig. 6.7 the set up to show the TPG capability for heat transfer compared with copper and aluminum is shown. Three pieces of material were cut and while the cold end (on the left) was in contact with the cooling block, the power was dissipated in the far right end by means of a SMD resistor (hot end). Several Pt100 resistors were glued at a different distances in between the two ends, to measure the temperatures. The temperature (measured with the Pt100 sensors) difference between the center and the cold end, normalized to the transverse area is presented as a function of the power dissipated by the resistor on the hot end (Fig. 6.8).

The physical mechanism that transfers energy through a surface and a moving fluid when they are at different temperatures is called *convection*. The convection heat transfer can be classified according to the nature of the flow in *natural*, if the flow is produced just by density differences in the fluid, or *forced* if the flow is caused by external elements (a fan, for example). The equation that governs the heat transfer process is called *Newton's law of cooling* (Eq. 6.1):

$$q'' = h \cdot (T_{surface} - T_{fluid}) \tag{6.1}$$

The heat transfer rate is proportional to the difference of the surface and the fluid temperatures and the proportionality constant (h) is called *convection heat transfer coefficient*, that depends on the surface geometry and the nature of the

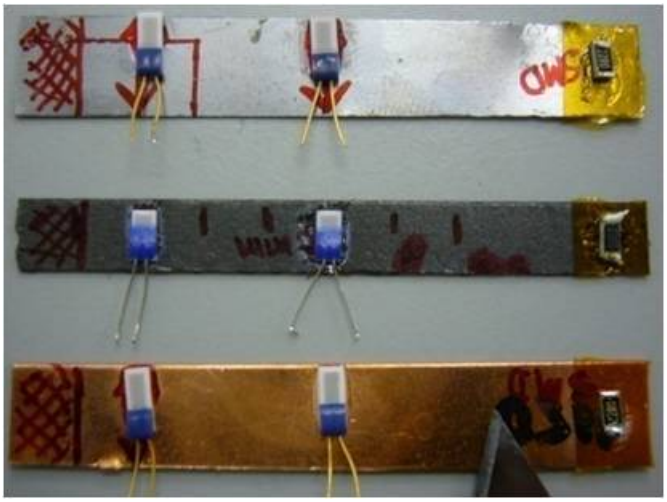

Figure 6.7: *Set up developed to test the thermal conductivities of various materials: Al (on top), TPG (middle) and Cu (bottom).*

fluid.

On the other hand, if the transfer occurs through a solid or a stationary fluid, the mechanism is called *conduction*. For heat conduction, the equation that governs the heat transfer per unit time in one dimensional plane is the *Fourier's law* (Eq. 6.2):

$$q_x^{''} = -k \cdot \frac{dT}{dx} \tag{6.2}$$

The heat transfer rate in the x direction per unit area (heat flux) is proportional to the temperature gradient on that direction. The proportionality constant (k) is a transport property called *thermal conductivity* and is a characteristic of the wall material. Assuming that the temperature distribution is linear, the Fourier's law (Eq. 6.2) can then be written in terms of the temperature gradient as follows (Eq. 6.3):

$$q_x^{''} = k \cdot \frac{T_1 - T_2}{L} \tag{6.3}$$

Plotting the ΔT (normalized to the transverse area of conduction) as a function of the power dissipated in the SMD resistor, an *effective* thermal conductivity can be extracted for each material using the slope of the linear fit (Fig. 6.8).

The ratio between the measured effective thermal coefficients matches the theoretical expectations (Eq. 6.4):

$$\frac{k_{TPG,effective}^{Measured}}{k_{Cu,effective}^{Measured}} = \frac{k_{TPG}^{Theoretical}}{k_{Cu}^{Theoretical}} = \frac{1600 \frac{W}{m \cdot K}}{400 \frac{W}{m \cdot K}} \tag{6.4}$$

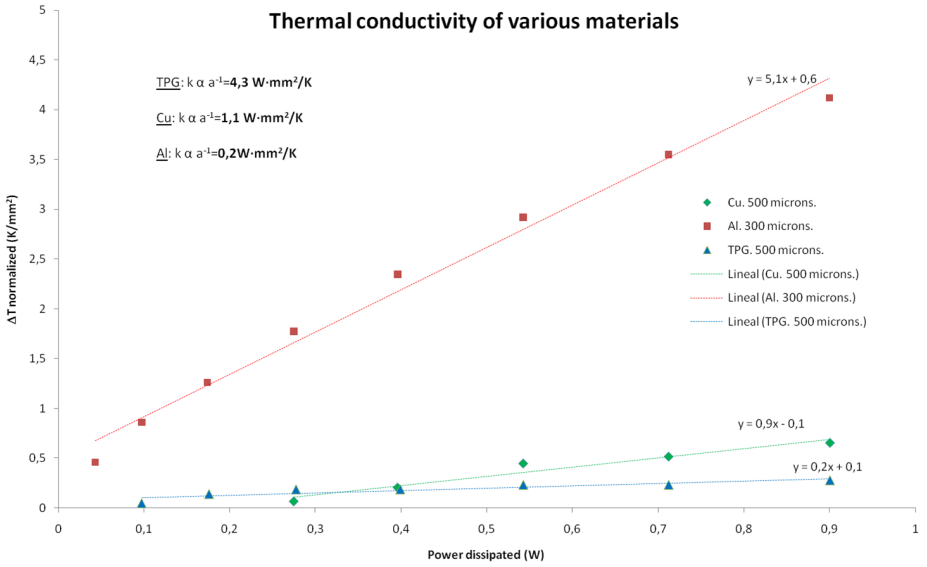

Figure 6.8: *The thermal conducitivies of various materials: Al (squares, $50 \cdot 8 \cdot 0.3\ mm^3$), TPG (triangles, $50 \cdot 6 \cdot 0.5\ mm^3$) and Cu (diamonds, $50 \cdot 8 \cdot 0.5\ mm^3$), can be extracted by plotting the ΔT on each material as a function of the power dissipated.*

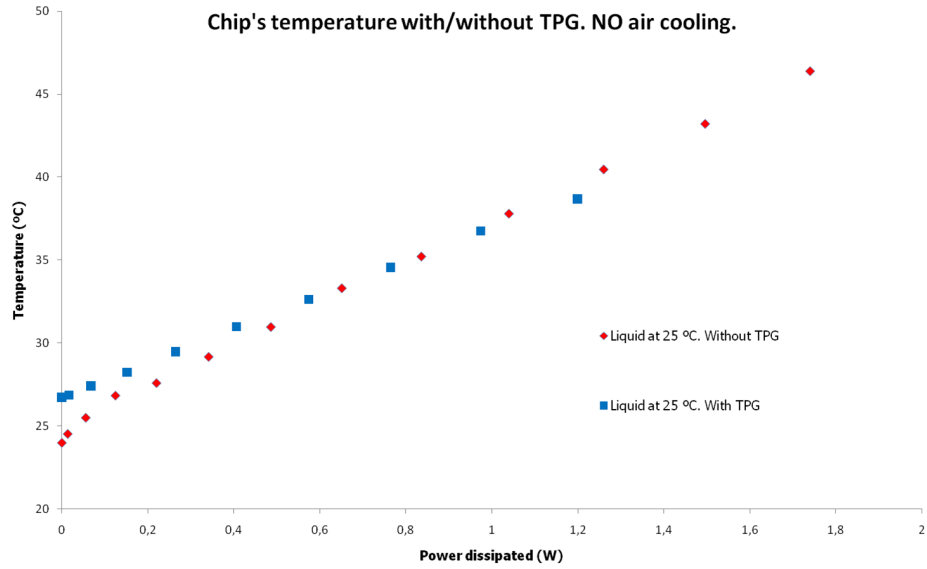

Figure 6.9: *The sensor's temperature is compared for a direct contact between the silicon and the cooling block and a contact by means of a TPG foil. The coolant is at 25 °C and no forced convection is used, and the overlap between the TPG and the microstrip detector is $2x14\ mm^2$.*

The thermal properties of the TPG (four times higher thermal conductivity than copper) makes this material a candidate to be used to connect the ladders to the support structures. On the other hand, although TPG has a high conductivity, this material tends to delaminate and for this reason also another new materials with higher conductivities (up to 2000 $W/m \cdot K$) and better mechanical properties, like CVD-Diamond [66], were also taken into account, giving good cooling results as well.

To show the properties of the TPG, two foils were incorporated at both ends of the microstrip detector shown in Fig 6.1 (a), to connect it to the cooling blocks. In Fig. 6.9 the sensor's temperature is shown as a function of the power dissipated in the heater with the silicon sensor directly connected to the cooling blocks and with a connection using TPG. At low power (below 0.5 W), the direct contact of the silicon seems to be a better option. In this case, the explanation could be the resistance of the joint that has to be made to connect the ladder to the TPG, using a glue (with a very low thermal conductivity of $\sim$1 $W/m \cdot K$) layer. At some point (around 1 W), the silicon started to *saturate* and then the better thermal properties of the TPG make this material a better option.

6.3 DEPFET thermal mock-up

Once the main cooling mechanisms of this minimal system are known, the next step would be to jump into a system closer to reality (Fig. 6.10). An ILC like DEPFET mechanical sample was equipped with new heaters (Fig. 6.11) at both ends of the stave to simulate the power consumption of the DCDs and DHPs and with an array of six heaters more on the lateral balcony to simulate the effect of the Switchers.

This ladder was connected to the cooling blocks and forced convection with cold air was also available. Because of the final power consumption can not be achieved with such heaters, a more conservative numbers were applied on the Switchers and readout chips of the system ($P_{Switcher} = 0.4\,W$ each, $P_{DCD} = 1.6\,W$ on each end). The power dissipation on the sensor was not considered in this measurements because of the impossibility to attach a heater on 50 μm of silicon. Once the system was ready, a set of measurements were done in order to disentangle the convection and conduction contributions to the cooling of such a close to reality system.

6.3.1 Forced convection

In Fig. 6.12 a set of thermal images show the temperature distribution in the ladder with different air speeds (from 0 m/s in (a) to 5.2 m/s in (e)). As in the microstrip detector, the air has major effect on cooling the middle of the sensor and, at higher speeds the effect between measurements is less significant. From 0 m/s (Fig. 6.12 (a)) to 1 m/s (Fig. 6.12 (b)), the temperature decreased a 10% while for an extra reduction of another 10%, the air speed has to be increased up to 5.2 m/s. It is

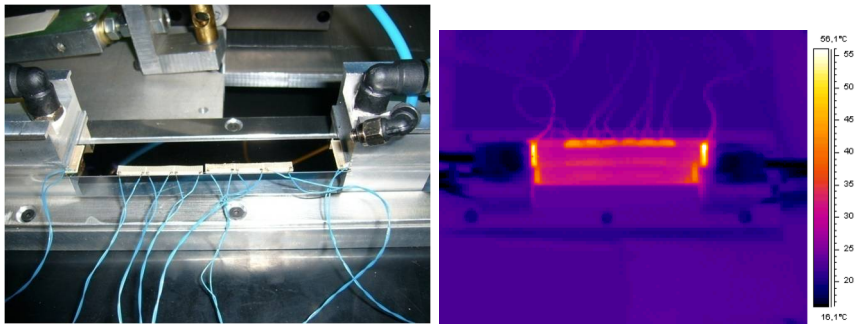

Figure 6.10: *DEPFET module with heaters to simulate the DCD and the Switchers. (Left) A real photo of the complete set-up is shown. The mechanical sample was placed in between the two cooling blocks. (Right) A thermal image with the heaters powered on.*

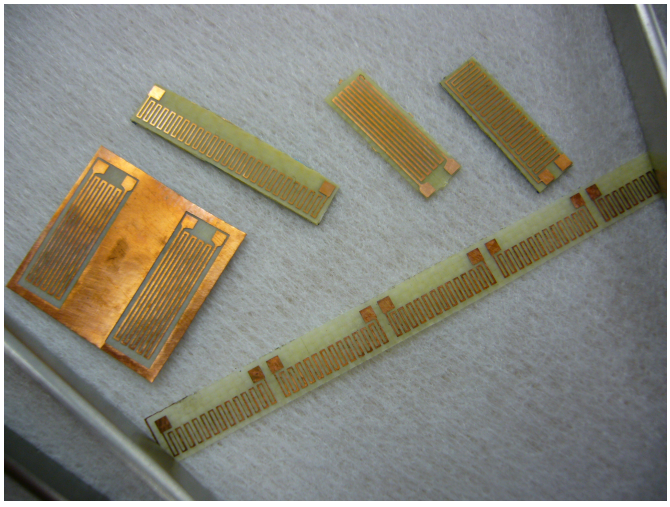

Figure 6.11: *A wide variety of heaters was designed ad hoc and produced at IFIC.*

also clear that after the cooling with forced convection, the maximum temperature that was then placed in the center of the ladder was displaced to the end of the stave.

In Fig. 6.13 is shown that, even with the Switchers in idle state, the DCDs generate enough power to heat up the middle of the sensor. With lower temperatures in the cooling blocks, the heat produced by the DCDs is more constrained on the end of the module, but the main work in the middle of the sensor has to be done by the air, anyway.

6.3.2 Conduction

The effect of the conduction can be observed by modifying the temperature of the cooling blocks (Fig. 6.14 (*a*) and (*b*)). The cooling blocks help the DCDs on both ends; they act as a barrier for the heat wanting to go to the center of the module but don't cool the middle of the sensor. The reduction of the coolant temperature in 8 °C just cause a reduction of 3 °C in the DCD's temperature, so just a moderate low temperature is needed in the cooling blocks. As can be seen once again, to cool down the center of the sensor (where the highest temperature is reached if there is no forced convection), forced convection has to be used (Fig. 6.14 (*c*)).

Introducing TPG

All the measurements made up to know, were done using a direct contact between the ladder and the cooling block. As was already said, this connection was intended to be done in the final design by means of support bars, made on a high conductivity material. Fig. 6.15 shows the effect of introducing TPG as a contact between the sensor and the cooling blocks with respect to a direct contact. The maximum temperature is a 10% higher in the TPG case but, as was seen in the microstrip detector, this difference is expected to be smaller if higher powers were dissipated in the system. Because the TPG does not degrade the temperature distribution in a relevant way, this material (at least taken into account its thermal properties) can be used to connect the ladders to the support structures.

6.4 Thermal simulations

In order to be able to extrapolate and study different geometries and configurations of the detector, detailed simulations were done using modeling with finite element analysis. The results of the simulations were validated with the measurements done in the laboratory. Due to the complexity of the system, only a single DEPFET Belle-II ladder was simulated, instead of the full detector. A second simplification considers a constant value of the convection heat transfer coefficient (h) of 5 $\frac{W}{m^2 \cdot K}$ for free convection and of 25 $\frac{W}{m^2 \cdot K}$ for forced convection [65], for the hole system.

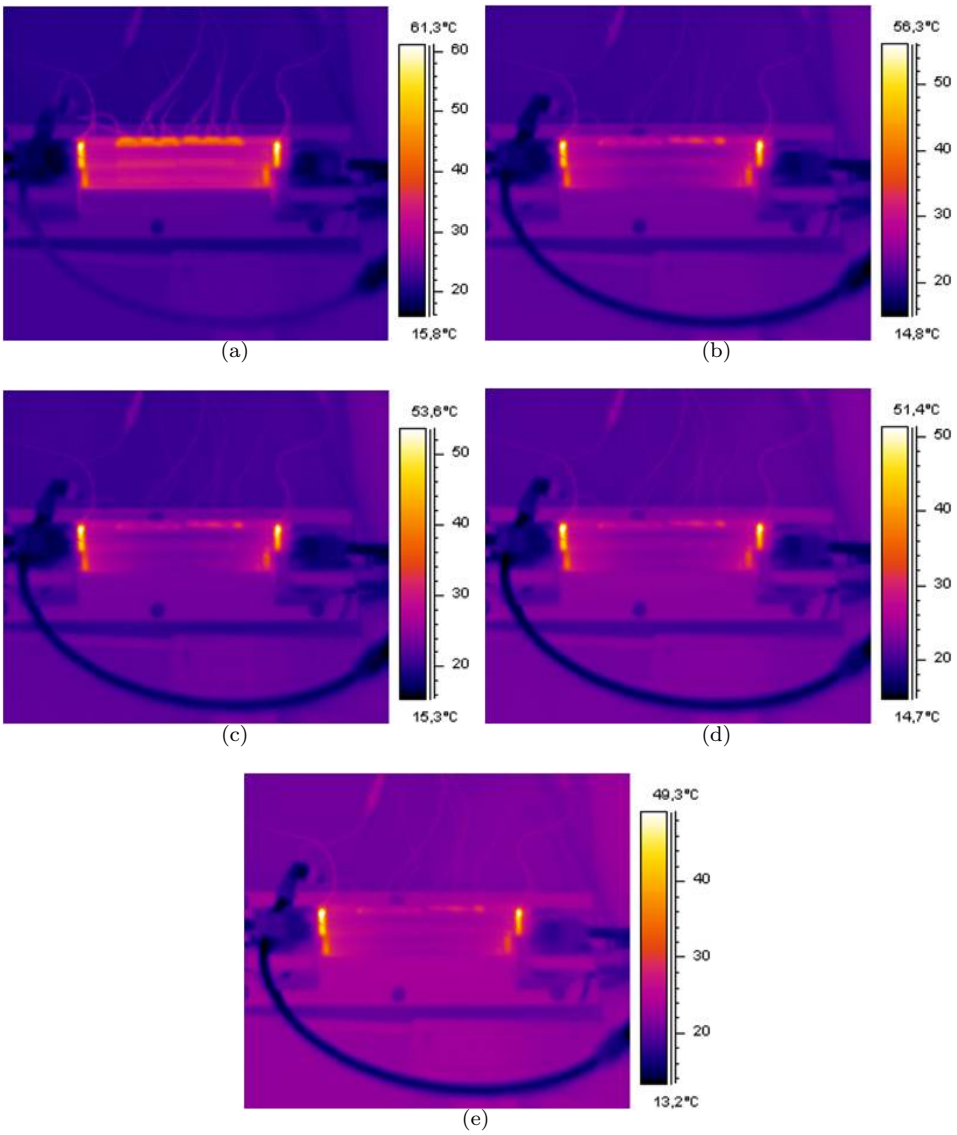

Figure 6.12: *The influence of the air on the thermal mockup is shown. The cooling blocks are at a temperature of 15 °C. (a)* $v_{air} = 0\ m/s$ *and* $T_{Max-ladder} = 61.3\ ^{\circ}C$. *(b)* $v_{air} = 1\ m/s$ *and* $T_{Max-ladder} = 56.3\ ^{\circ}C$. *(c)* $v_{air} = 2.2\ m/s$ *and* $T_{Max-ladder} = 53.6\ ^{\circ}C$. *(d)* $v_{air} = 3.5\ m/s$ *and* $T_{Max-ladder} = 51.4\ ^{\circ}C$. *(e)* $v_{air} = 5.2\ m/s$ *and* $T_{Max-ladder} = 49.3\ ^{\circ}C$.

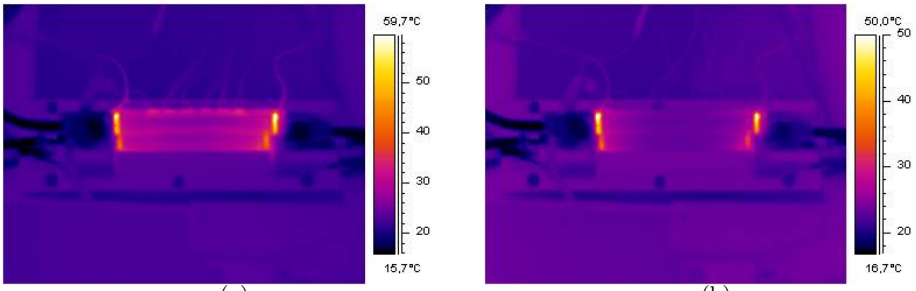

(a) (b)

Figure 6.13: *In this figure, the Switchers are in idle state and only the DCDs are working. The cooling blocks are at a temperature of 15 °C.* (*a*) *With natural convection* ($v_{air} = 0\ m/s$) *the temperature is 59.7 °C while with air forced* (*b*) *the temperature decreased down to 50.0 °C.)*

6.4.1 Flip chip

The first drawback to be addressed to implement the ladder's geometry, concerned the ASICs bump bonding. The first studies done, were to see if the bumps were a bottleneck for the heat created in the chip and to see if the temperature of the chip was out of tolerable limits. This study is specially important for the readout chips, because the heat produced on them has to be redirected through their base and dissipated using the massive cooling structures below.

The real geometry of the bump array is shown in Fig. 6.16 (*a*). Although this complexity was fully implemented in the finite element analysis (Fig. 6.16 (*b*)), this realistic simulation was abandoned in favor of a simplified one (Fig. 6.16 (*c*)). In this simplified model, only a single ball (flattened as expected after the flip chip), was used instead. The applied value for the thermal conductivity was chosen as the mean value of the thermal conductivities of the materials used on each element (solder balls, under-bump metalizations and solder joints), weighted by their expected thicknesses. This simplified simulation gives the same results as the realistic case but with much less CPU time consumption, so the complex model was abandoned.

The geometry of a Switcher chip was implemented in a finite element software (its dimensions are $1.2 \cdot 3.6\ mm^2$ and 450 μm thick) and equipped with 96 bumps with a bump pitch array of $150 \cdot 150\ \mu m^2$ and an effective thermal conductivity of 57 $\frac{W}{m \cdot K}$ (Fig. 6.17 (*a*)). The Switcher was then flip chip to a substrate (Fig. 6.17 (*b*)) whose bottom surface was kept at a constant temperature while a certain amount of power was dissipated in the whole chip's volume. With this first study, it was demonstrated that the heat traveled without problems through the bumps and that, even with natural convection, to keep the chip at a reasonable temperature, it was just enough to control the temperature of the substrate below it (Fig. 6.18). In this figure, the maximum temperature on the chip is presented as a function of

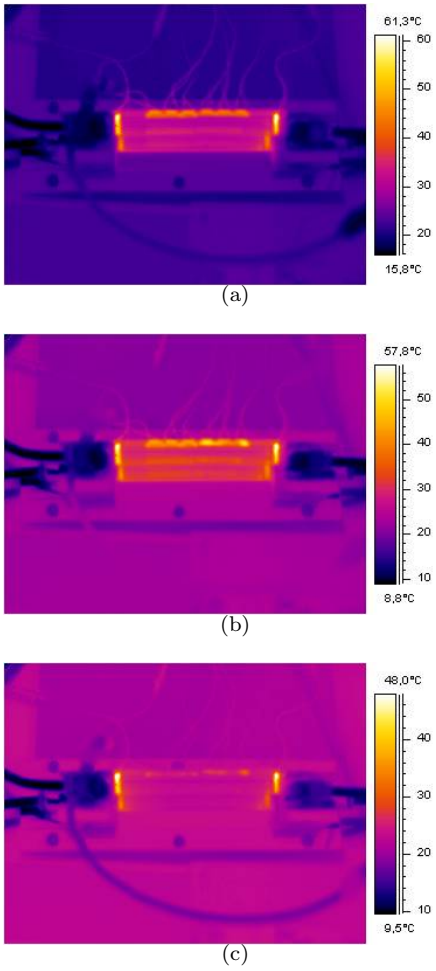

Figure 6.14: *The influence of the temperature of the cooling blocks.* (*a*) $v_{air} = 0\ m/s$ *and* $T_{liquid} = 15\ ^{\circ}C$. (*b*) $v_{air} = 0\ m/s$ *and* $T_{liquid} = 7\ ^{\circ}C$. (*c*) $v_{air} = 5.2\ m/s$ *and* $T_{liquid} = 7\ ^{\circ}C$. *By reducing the temperature of the coolant the end of stave is colder, but has no major effect in the center of the sensor.*

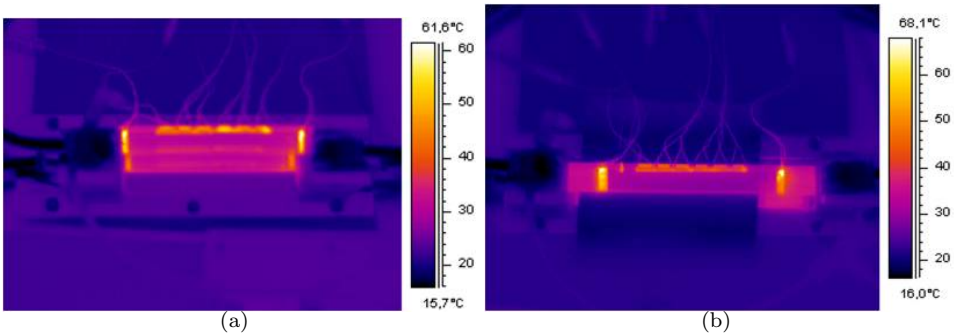

Figure 6.15: (*a*) *Direct contact between the silicon and the cooling blocks with no forced convection.* (*b*) *In this case, the contact is made by means of a couple of TPG foils. The same result is obtained in both cases, as expected, and the TPG does not degrade the temperatures inside the ladder.*

the temperature of the substrate below it. As can be seen from the slope of the linear fit, no matter the power dissipated, variations in the substrate's temperature are directly reflected on the chip's temperature; the power dissipated on the chip just shift the offset of the curve.

In order to implement the complete module while keeping the CPU time reasonable, an equivalent thermal coefficient of the already simplified bump matrix was performed. The idea is to replace the array of bumps (*full simulation*) by a block of thickness equal to the bump height, filling the total area with a material with a thermal effective coefficient (k_{eff}) (Fig. 6.18 (*c*)), *fast simulation*. An iterative process of the thermal coefficient calculation, gave an optimal value of $k_{eff} = 6\ \frac{W}{m \cdot K}$ for which both simulations gave identical results at this temperature range (Fig. 6.19). In this figure. the ratio of the maximum temperatures achieved with the *fast* and *full* simulations for three different powers, are shown (in %), revealing a perfect agreement (above 99.9%) between both cases. Giving these results, on the following sections, the simplified bump bond array will be used instead of the full one, for simplicity.

6.4.2 High conductivity support bars

The first simulated geometry (Fig. 6.20 (*c*)) recreates the DCD and DHP chips on the end of the ladder, the Switcher chips on the lateral balcony as well as a thinned central sensitive region. In this model, a CVD-diamond finger to connect the ladders with the cooling blocks was also implemented. This bridge acts as a heat path to the heat generated in the end of the stave to be driven to the cooling massive structure as well as to give mechanical stability to the ladders. In a first approximation, two different concepts were simulated (Fig. 6.20 (*a*) and (*b*)). In the t-shape option ((*a*)), the diamond covers all the area where the chips will dissipate heat, while in the t-shape extended option ((*b*)) an extra piece of

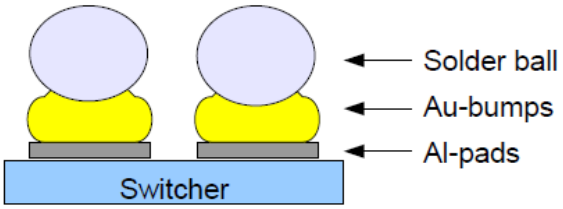

(a)

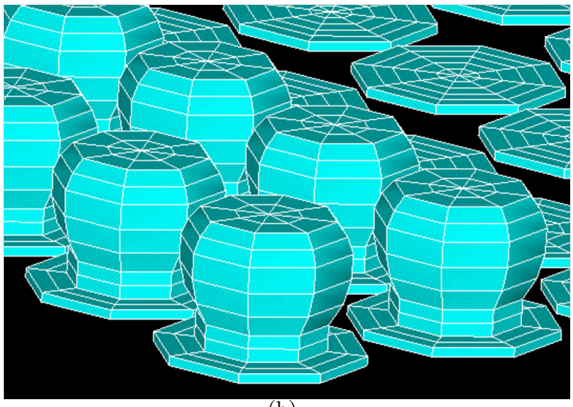

(b)

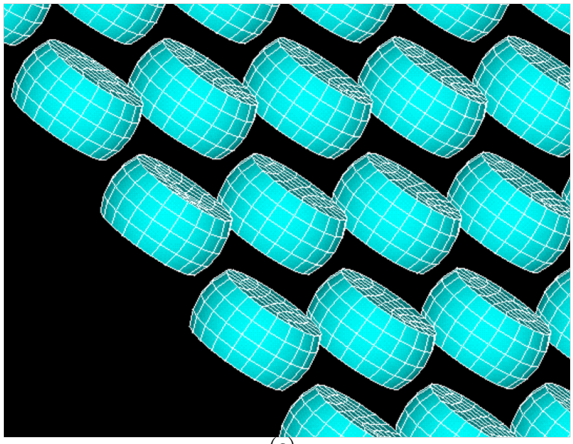

(c)

Figure 6.16: (*a*) *Bump bonding scheme.* (*b*) *Realistic simulation of the bump array.* (*c*) *A simplified model was implemented, showing similar results as the realistic case.*

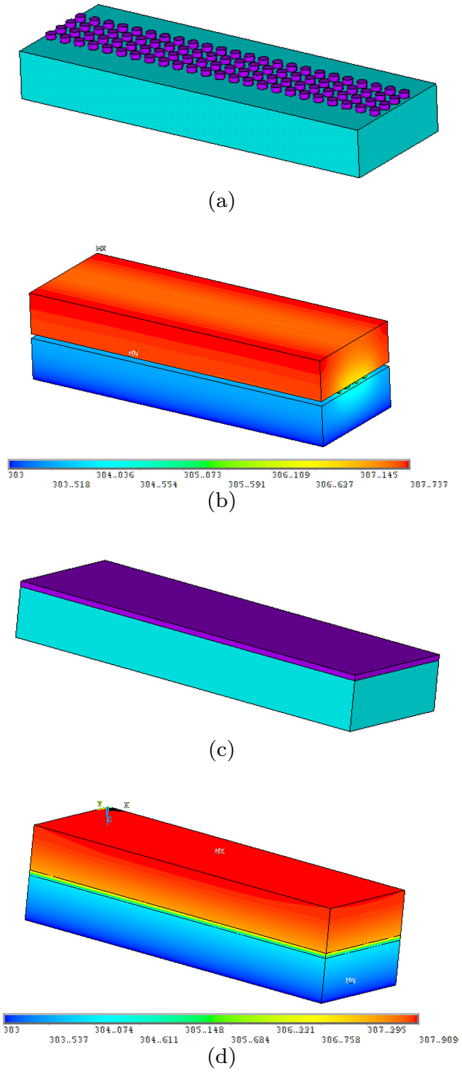

(a)

(b)

(c)

(d)

Figure 6.17: (*a*) *Geometry of a Switcher chip with the bumps created on the bottom.* (*b*) *The chip is flipped into the substrate and, while the latter is kept at a fixed temperature, a certain amount of power is dissipated in the chip's volume.* (*c*) *An equivalent model*

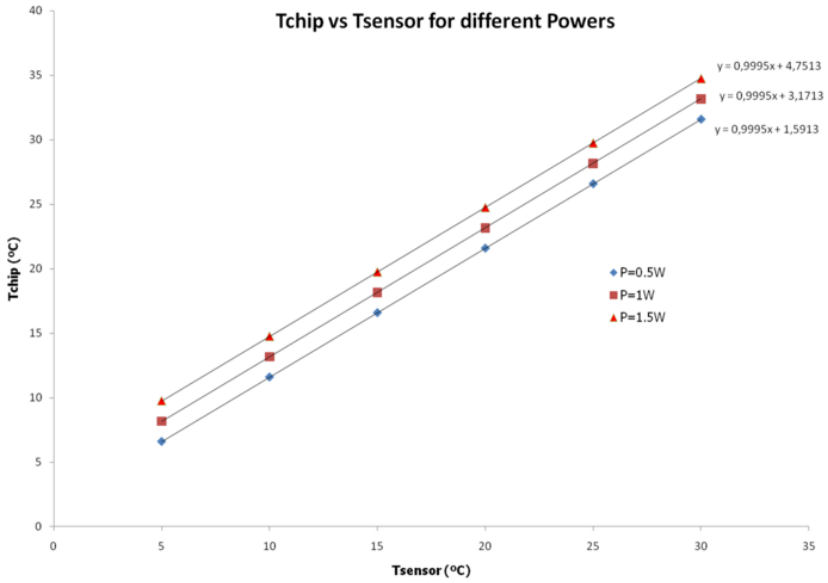

Figure 6.18: *The chip's temperature is shown as a function of the substrate temperature for three different powers dissipated in the Switcher. The temperature on the chip is the substrate temperature plus an offset which depends on the power. Controlling the substrate, the chip is also under control.*

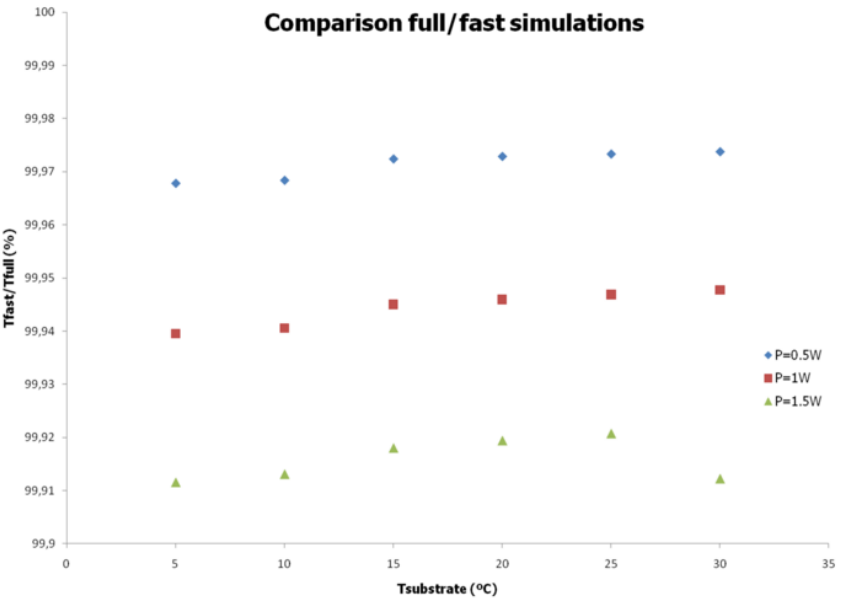

Figure 6.19: *The ratio of the values obtained between the fast and full simulations for three different powers dissipated in the chip are shown. A good agreement is found between the two, if an effective thermal coefficient of* $k_{eff} = 6\ \frac{W}{m \cdot K}$ *is used.*

diamond covers also the lateral balcony where the steering chips are placed to remove, partially, the heat produced there by means of conduction.

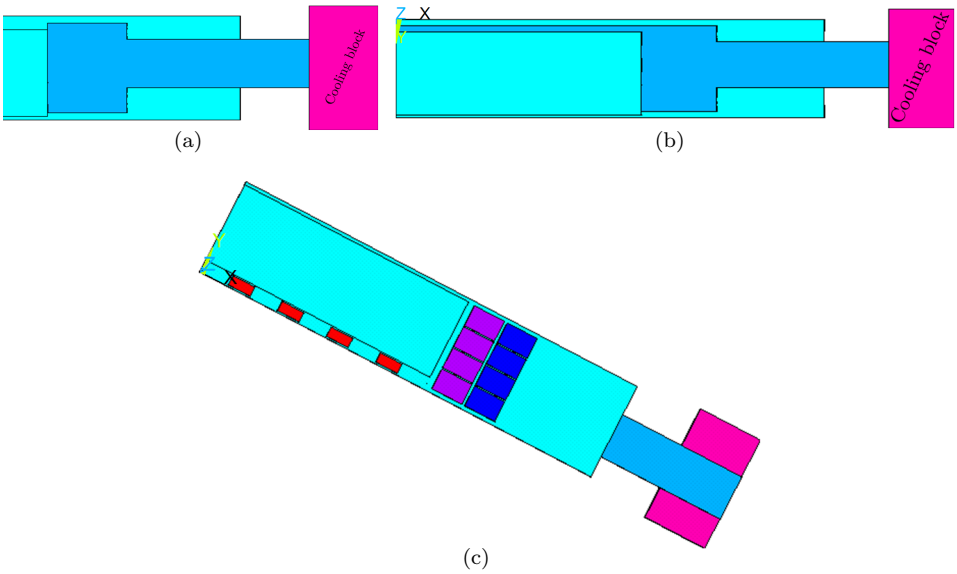

Figure 6.20: *The first cooling options contained a CVD-diamond finger to connect the ladder with the cooling blocks. Two options, covering the area under the ladder where the DCD and DHP generate power (t-shape, (a)) and also the lateral balcony (t-shape extended, (b)), were studied. (c) Top view of the ladder with the finger below.*

The first results concerning simulation are shown in Fig. 6.21. In this plot, the effect of the air speed in the maximum temperature achieved in the ladder, while keeping the cooling blocks at 0°C, for the two options (t-shape and t-shape extended) are shown. As can be seen, the highest temperature reduction is achieved from free (v_{air}=0 m/s) to forced convection with air at a very low speed and then, a plateau is reached, as was checked in the laboratory measurements. In the t-shape extended case, the heat produced by the Switchers along the ladder is partially removed by conduction using the diamond finger below the balcony so, the situation is more favorable from the beginning and the air has to do less work rather than in the t-shape only case. The initial temperature is lower and the plateau is reached sooner, with lower speeds.

The influence of the forced convection can be even amplified by using cold air instead of air at room temperature. In Fig. 6.22 the maximum ladder's temperature is presented as a function of the air temperature for free and forced convection. Although the most effective way to cool down the center of the detector is by forced convection, if the temperature in that region has to be reduced even more while keeping the air at low speed to avoid vibrations, cooling the air is the only way to reach it.

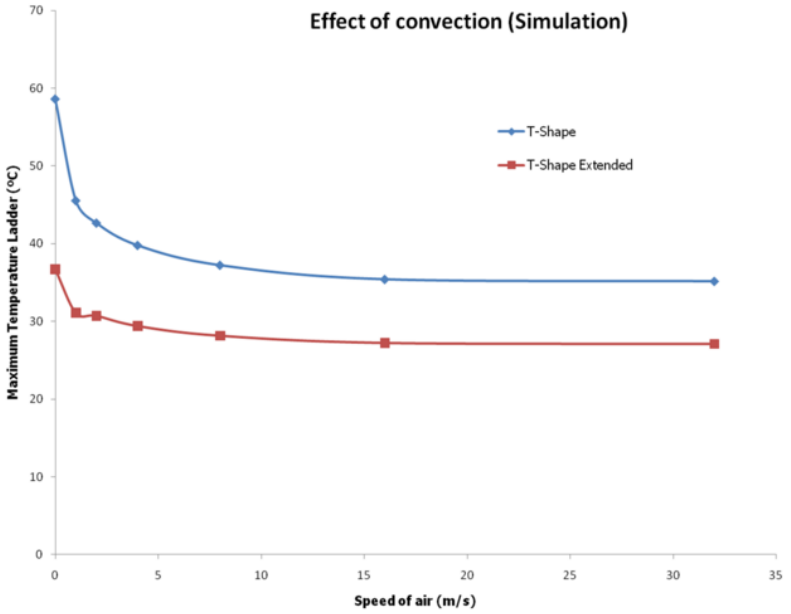

Figure 6.21: *Maximum temperature in the ladder as a function of the speed of air (at room temperature), for two configurations of the CVD-Diamond fingers. The t-shape, on covers the full ladder area under the chips while the t-shape extended, covers also the balcony where the Switchers are placed. The cooling block was fixed at 0° C.*

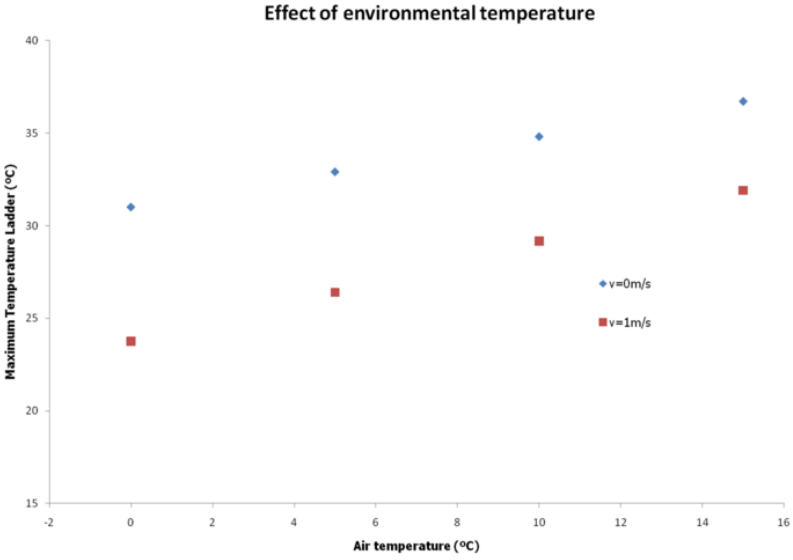

Figure 6.22: *The maximum temperature achieved in the ladder is presented as a function of the air temperature for free and forced convection with air at 1 m/s. T-shape option and 0 ° C on the cooling blocks*

The next element that can be modified is the temperature of the cooling blocks. In Fig. 6.23, the maximum temperature in the ladder is shown for different coolant temperatures. In this case, the efficiency is quite low, because the gain is 0.6 °C for 1 °C less in the cooling block. As was demonstrated in the laboratory measurements, the coolant in the cooling blocks has no major influence in the center of the ladder and just only prevent the heat produced in the end of the stave to enter the sensitive area.

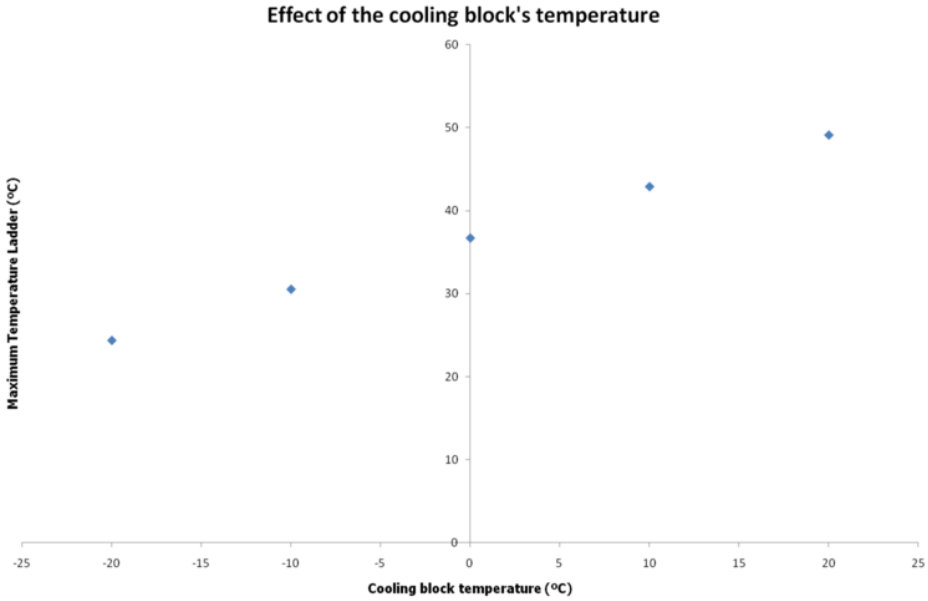

Figure 6.23: *The maximum temperature achieved in the ladder as a function of the temperature in the cooling blocks is presented.*

Another important parameter to take into account once the design of the mechanical structure is the maximum length achievable with the diamond bridge. In Fig. 6.24, the temperature in the ladder is shown as a function of the diamond length bridge, for two bridge configurations: t-shape and t-shape extended. As expected, the ladder has to be as close as possible to the cooling block. Once again, analyzing the slope of the linear fit, the t-shape extended is the best option, although a difference of around 20 °C is achieved between the two extreme cases (0 mm and 50 mm).

In building a cooling solution for the detector, every little detail has to be studied carefully. To show the importance of each element, the evolution of the temperature in the ladder as a function of the thermal conductivity of the glue that fixes the diamond finger to the cooling block and to the ladder, is shown in Fig. 6.25. Although there are no glues in the market with a conductivity of 50 $W/m \cdot K$ (where the temperature plateau is already achieved), a difference from 1 to 3 $W/m \cdot K$ mean a difference of several degrees in the maximum temperature. Even in the case that the environmental conditions were the optimal ones, a bad

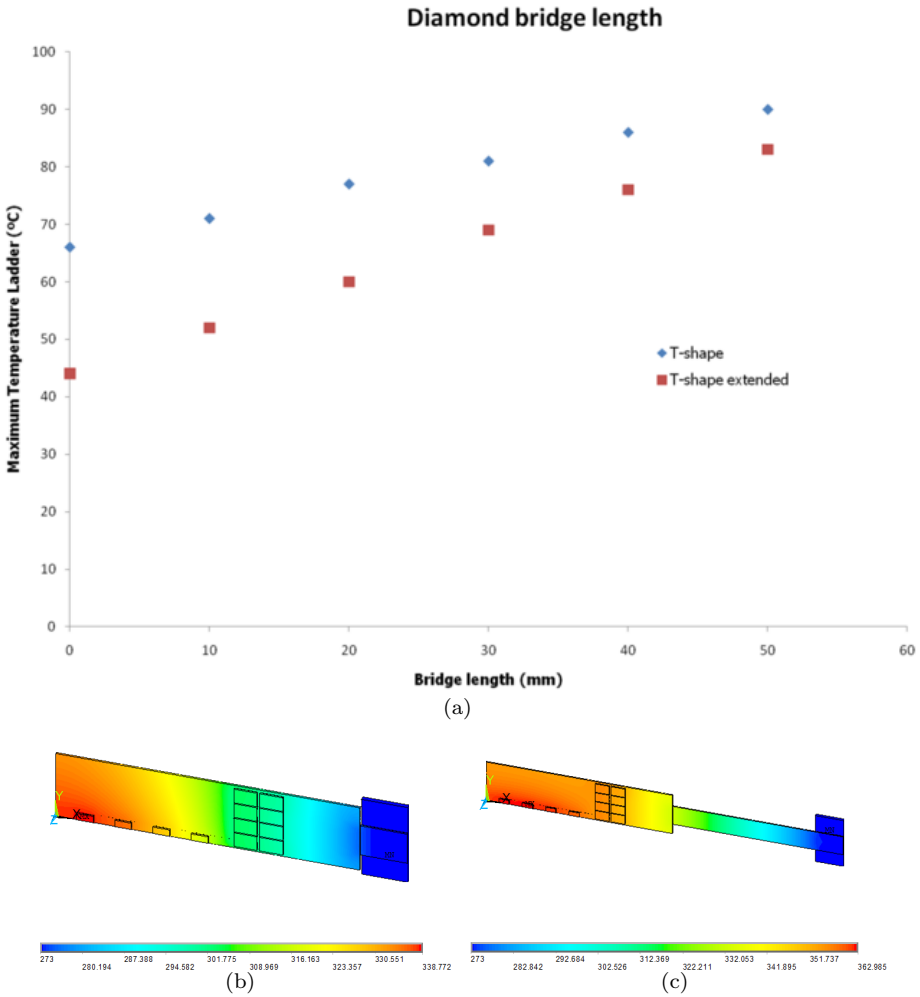

Figure 6.24: *The length of the diamond bridge, connecting the ladder with the massive cold structure, is an important parameter in the cooling blocks design. In this case, the maximum temperature in the ladder is plot for different lengths and diamond configurations, t-shape and t-shape extended. As expected, the shorter the bridge, the lower temperatures achieved. The cooling blocks are at 0 °C with free convection. The overlap of the diamond finger with the cooling block is 70 mm^2. The two extreme cases studied here belong to lengths of 0 mm (b) and 50 mm (c).*

selection of the thermal conductive glue, can ruin the experiment.

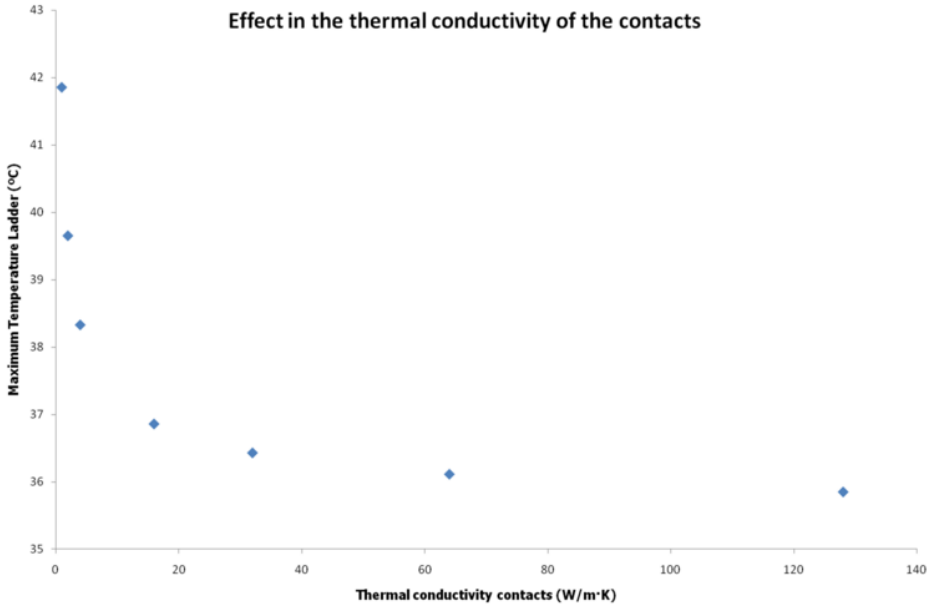

Figure 6.25: *The connection between the diamond and the sensor and the diamond with the cooling block should be done maximizing the thermal conductivity. Making a careful selection of the glue or grease to be used in the joints, the temperature can be decreased. In this case, the cooling blocks were at 0 °C and free convection.*

6.5 New geometry: towards a final design

Up to now, the geometry implemented in the finite element model corresponds to a generic ladder and the studies performed serve to check if the behavior obtained in the simulations matches the observed in the laboratory measurements. The next step is the implementation of the geometry of one of the ladders belonging to the outer layer of the PXD detector of Belle-II. In the Table 6.1 and Fig. 6.26 (*a*) and (*b*), a comparison between both designs is shown. The main difference is that in the new design the full module will consist of two half ladders glued at the center (to break electrically the connections and avoid ground loops with the magnetic field) with a couple of reinforcement pins; the second new element is the etching opened in the lateral balcony to reduce the material budget (Fig. 6.26 (*c*)). Fig. 6.26 (*a*) and (*b*) shows that, for the t-shape option and under the same conditions, in the new design the maximum temperature is lower; in this case, this is caused because of the lower heat density (the same amount of power is dissipated on a bigger area) and the frame perforation helps the convection because of the increased area.

During these studies, a completely new mechanical design was developed in the collaboration. Because of longer ladders could be produced (two half ladders glued

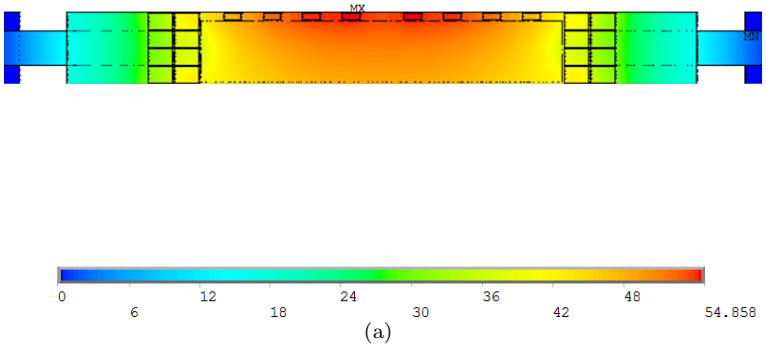

(a)

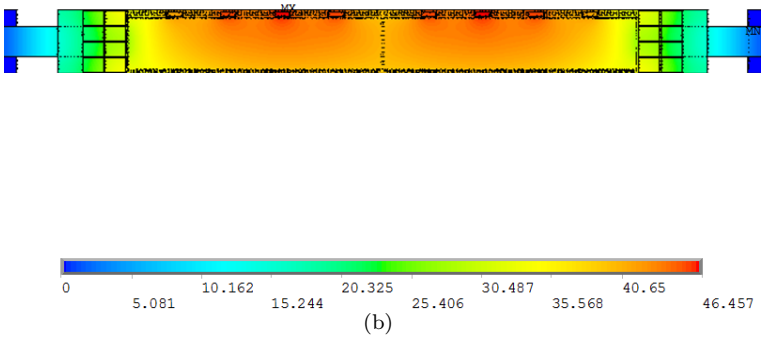

(b)

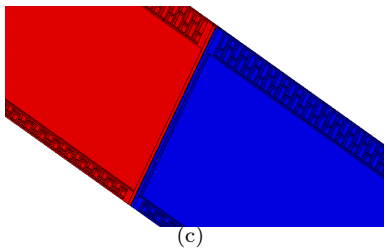

(c)

Figure 6.26: *A comparison between the old (a) and new (b) geometries is shown. Although the power dissipated and the environmental conditions (cooling blocks at 0 °C and forced convection with air at 1 m/s), just because of the power is dissipated over a bigger area, the temperature achieved is lower in the new geometry. The detailed of the two half ladders glued in the center and the frame perforation on the lateral balconies is shown in (c).*

	Old design	New design
Ladder length (mm)	65.5	78.35
Ladder width (mm)	15	15
Length end of stave (mm)	28	17
Length lateral balcony (mm)	2	2
Sensor width (mm)	12.5	12
Sensor length (mm)	75	$2 \cdot 61.35$
Thickness (μm)	50	50

Table 6.1: *Comparison between generic ladder implemented in the first step and a close to final geometry of one of the ladders belonging to the outer layer of the Belle-II PXD detector. Apart from the differences in length, the ladder will consist of two half ladders glued in the center, and the lateral balcony is etched to reduce the material budget.*

in the center) a new mechanical design could be developed to accommodate them in the cooling block with a direct contact, without the need of the support bars. With this new and simpler cooling design, the only problem is the attachment of the ladder to the cooling block, that has to be done with extremely precaution in order not to break the silicon slab. The physics performance defined also the pixel size and the number of pixels needed to cover the hole sensor; this studies also fixed the number of Switchers needed to steer the pixels in the matrix, to a number of 12, so this new situation was also implemented in the finite element software. Finally, the ultimate ladder's design is shown in Fig. 6.27; this design never changed again, and the simulation from this point recreates faithfully the final ladder geometry.

6.6 Fixing the working conditions

Having the full Belle-II ladder completely implemented in the finite element software, this tool has to be used to develop the cooling solutions knowing that the upper limits on the temperatures tolerable by the chips and the sensor are 60 °C and 30 °C, respectively. After the implementation of the right geometry, the estimated loads on the different elements of the system (DCD, DHP, Switchers and Sensor) were applied, as shown in Fig. 6.27. Using this conditions, both the environmental and the cooling block temperatures were varied in a wide range and the maximum temperature achieved on each element were extracted from the simulation and compared with the upper established limits. The environment temperature was varied from -20 °C to +15 °C, while the cooling block was in the range between -25 °C and +20 °C, and for all the simulations a forced convection with $v_{air} = 1\ m/s$ was used (the need of forced convection was presented in previous measurements and simulations). According with these conditions the

maximum temperature achieved in the DCDs (Fig. 6.28), Switchers (Fig. 6.29) and sensor (Fig. 6.30) were extracted withing this wide temperature range.

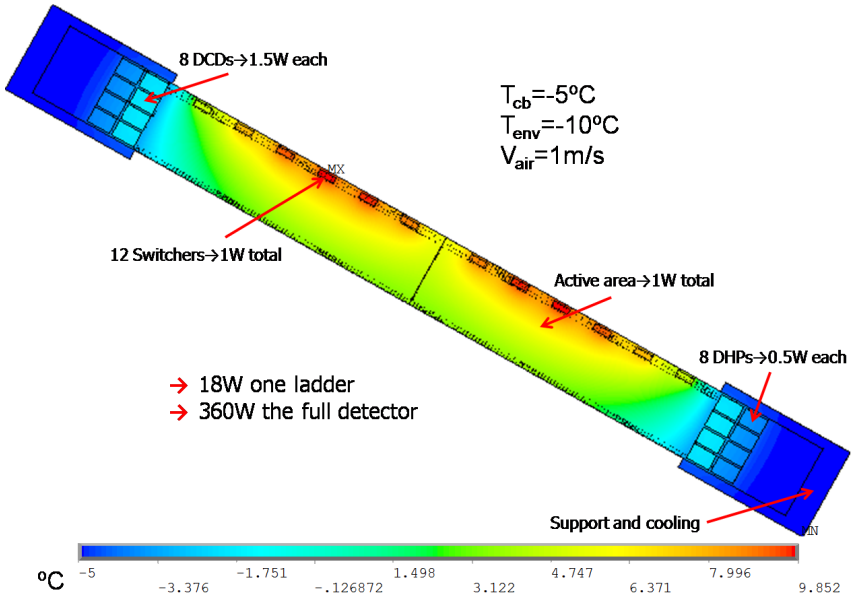

Figure 6.27: *Estimated power dissipation on each element. The geometry recreates faithfully the final ladder geometry of the Belle-II PXD detector.*

In Fig. 6.28, the maximum DCD temperature is shown for each pair of temperature values (environment and cooling block) within the established range. As can be seen, the maximum temperature achieved (25 °C) is always within the temperature limits (60 °C) in this range of temperatures. The variation of the DCD temperature with the environmental temperature is almost flat, so varying this temperature has no major effect on the DCD's temperature. The major contribution comes from the cooling block's temperature when, a variation of one degree in this element, transforms directly in the same degree of variation in the readout chips.

In Fig. 6.29, the maximum temperature achieved in the Switchers is plotted as a function of the environment and cooling block's temperatures. As in the DCD case, the maximum Switcher's temperature is always within the temperature limits in this range of values, but contrary to that case, the major influence in this element comes from the environmental's temperature; a decrease in one degree in the air temperature is directly translated into one degree less in the Switchers, without increasing its speed. Contrary, the variation of the Switchers temperature with the cooling block is almost flat and no variation is observed, while the temperature is kept below -10 °C. The maximum temperature is always achieved in the Switcher closer to the center of the ladder unless the cooling block's temperature is above -5 °C. In the latter case, the cooling block is not able to retain the heat produced in the end of the stave by the readout chips and this heat enters the sensitive area.

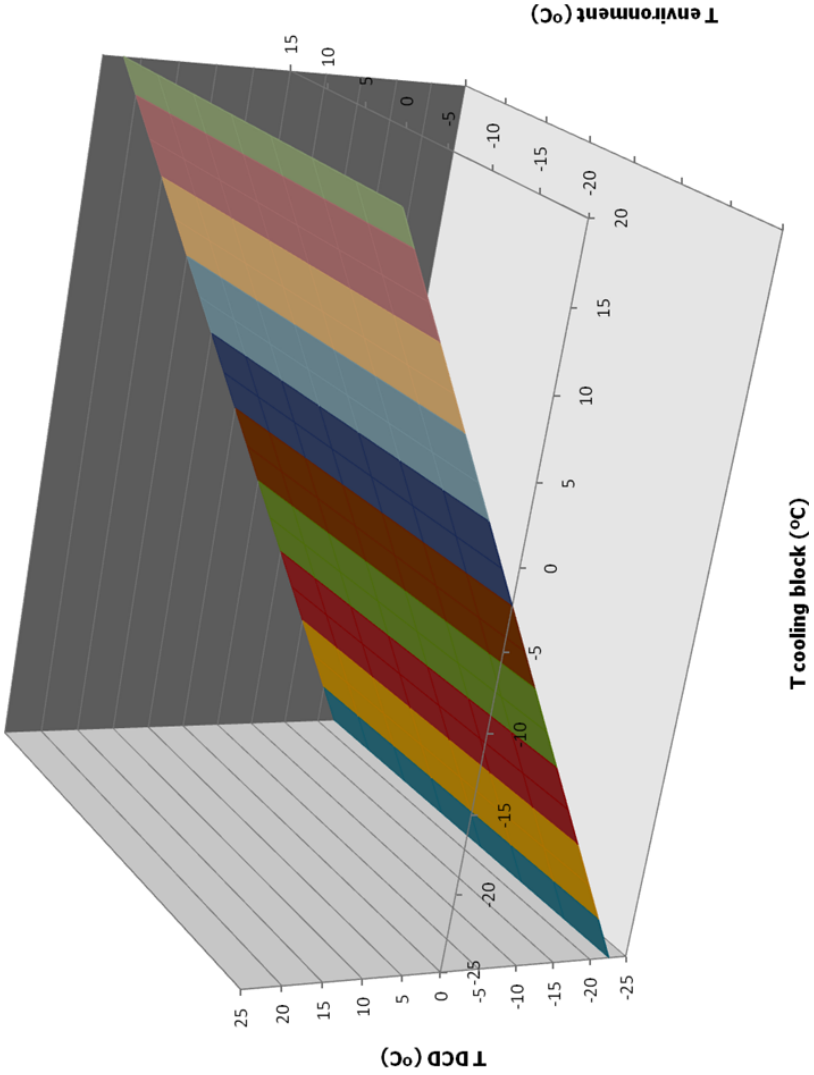

Figure 6.28: *The maximum temperature reached in the DCD readout chip placed at both ends of the stave are shown for a wide variation in the environment-cooling block temperatures parameter space. As can be seen, the temperatures are always within the established limits, in this range. The variation of the environmental temperature has no major impact on the DCD, while the major influence comes from the cooling block's temperature (as demonstrated in previous simulations).*

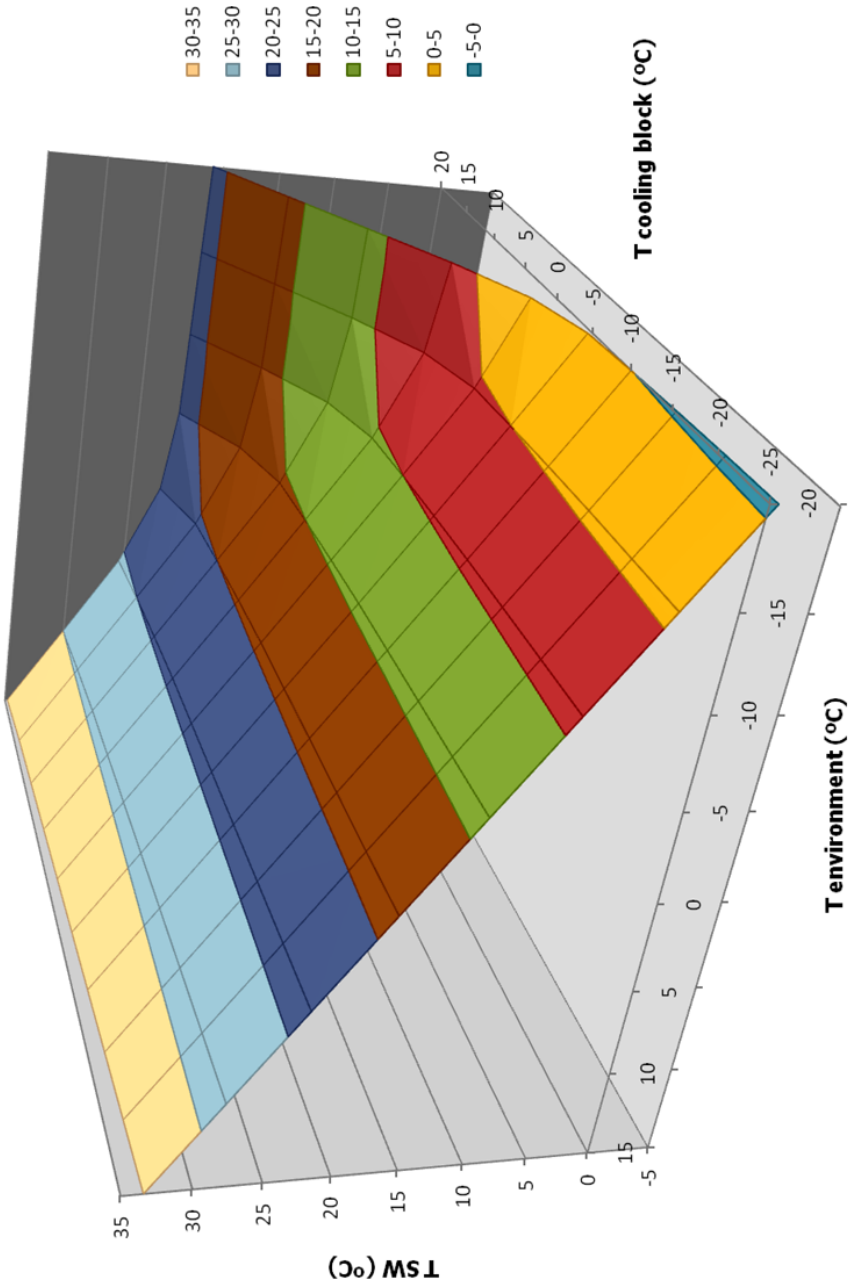

Figure 6.29: *The same study was done like in the Fig. 6.28 but the maximum temperature of the Switchers was studied instead of the DCD. Contrary to the DCD case, the major job in the center of the ladder (where the hottest Switcher is always found) is done by the forced convection.*

This feature is observed in the plot with a shoulder in a flat distribution and in this case, the hottest Switcher is the one close to the DCD.

Finally, in Fig. 6.30, the same study is reproduced but the maximum temperature of the Sensor is shown (instead of the Switchers). The behavior of the curve is the same as the one for the Switchers, but in this case, the upper sensor limit (30 °C) is reached when using environmental temperatures above 10 °C, and this region should be avoided. Once again, the cooling block has no major influence in the Sensor's temperature and its role is limited to prevent the heat produced in the end of stave to enter the sensitive region. The major influence comes from the environment's temperature and a decrease in this value is directly reflected in the Sensor's.

According to these simulations, whichever combinations for the environment and cooling block temperature give a result within the limits for all the components (except for a small environment strip regarding the Sensor), so these constraints do not allow the fixation of a working point for the system. A new indicator has to be introduced in order to decide the temperatures to be applied (Eq. 6.5):

$$\Delta T_{Sensor} = T_{MaxSensor} - T_{MinSensor} \tag{6.5}$$

The gradient temperature in the sensor should be minimized in order to obtain an uniform response of the sensor and to avoid thermal stresses because of the CTE mismatch between the different constituents inside the ladder (copper lines, aluminum layers, oxides, polysilicons). As can be seen in Fig. 6.31, the environment and cooling blocks temperatures are not free parameters anymore and only certain combinations them give as a result a minimal value of the gradient along the sensor. This relation has to be calculated for a defined geometry and power consumptions.

In Fig. 6.32, the relation between the environment and the cooling blocks temperature to achieve a minimal temperature gradient and a maximum ladder's temperature of around ∼15 °C is calculated for several different thicknesses, from 20 μm to 200 μm. It is clear that, although no great variation is found, both temperatures have different optimal relations depending on the thickness. Because of the main stopper is the environment temperature (it is not easy to cool down the air), this value was always fixed to -5 °C, while the cooling block temperature (the point where a wider temperature range can be achieved) was varied to minimize the ΔT. Although 20 μm is a thickness that can not be reached with the thinning technology and 200 μm is too much material (in terms of multiple Coulomb scattering), those points were simulated to study the behavior of the curve. With these sets of reasonable parameters, and although the thicker sensor, the better, the temperature are always below the limits and all of them could be used to operate the system.

According to this optimization procedure, a working point was found using the following temperatures $T_{Environment} = -5$ °C and $T_{CoolingBlock} = 8$ °C for a thickness of 75 μm; this new thickness value was chosen to increase the robustness

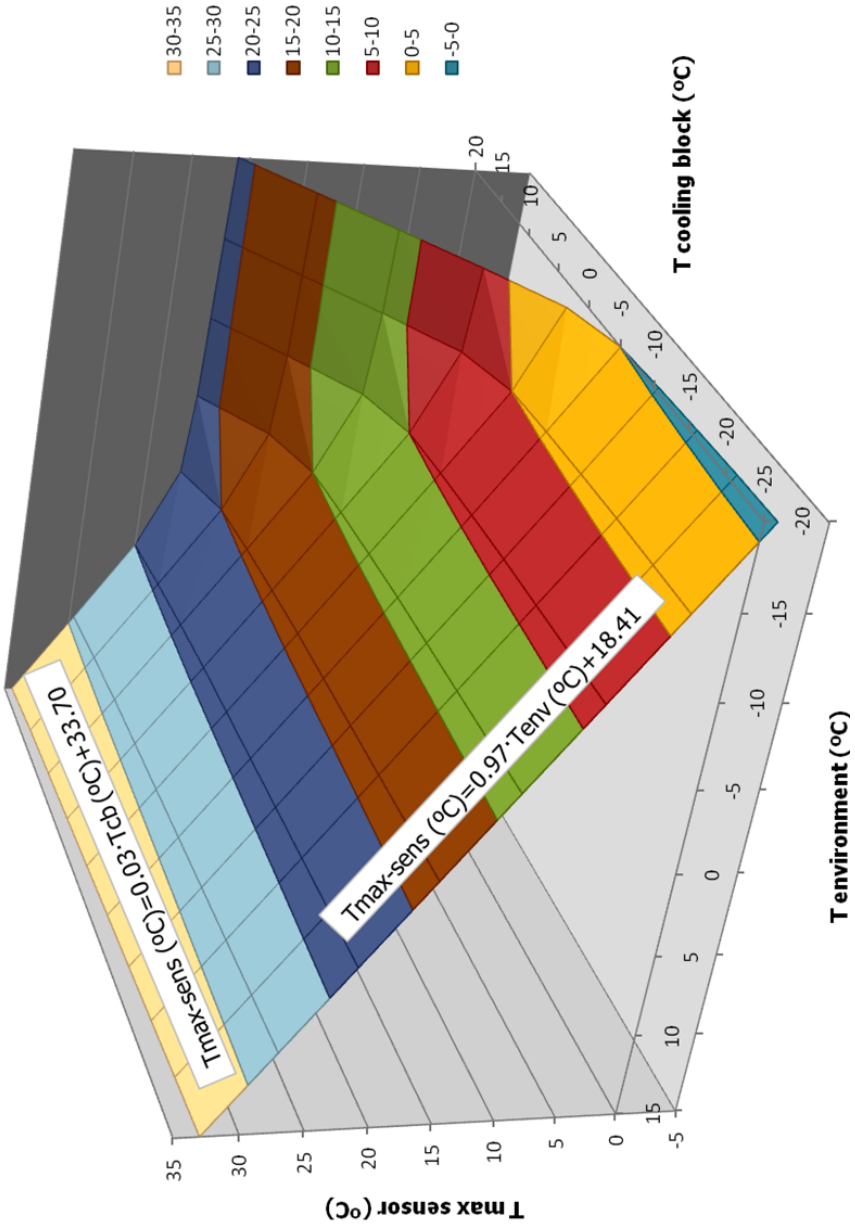

Figure 6.30: *The same study was done like in the Fig. 6.28 but the maximum temperature of the Sensor was studied instead of the DCD. The behavior is similar to the one obtained for the Switcher studies, and the major influence comes from the forced convection in the center of the ladder.*

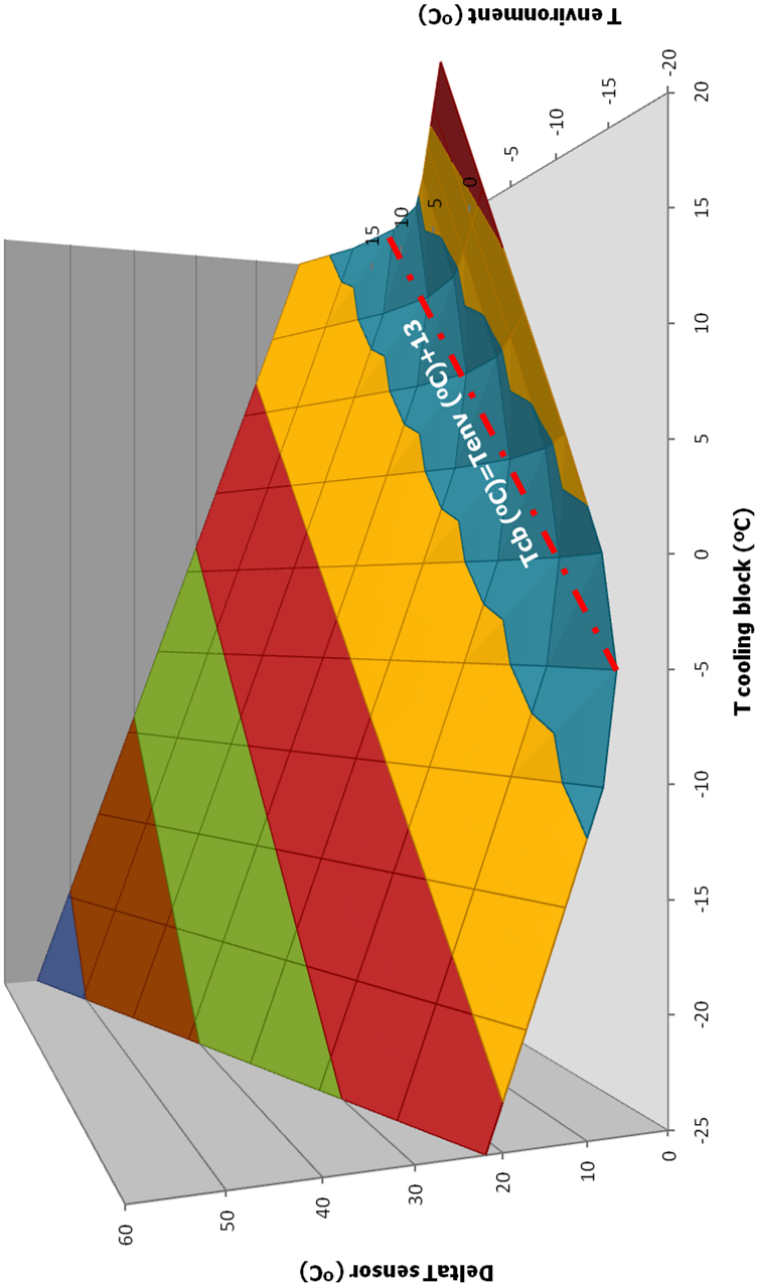

Figure 6.31: *Gradient temperature along the ladder as a function of the environment and cooling block temperatures. In order to keep the gradient minimal, a relation between both parameters is need. In this case, this relation is established for a sensor thickness of 50 μm, but this can change with a different geometry or power consumption.*

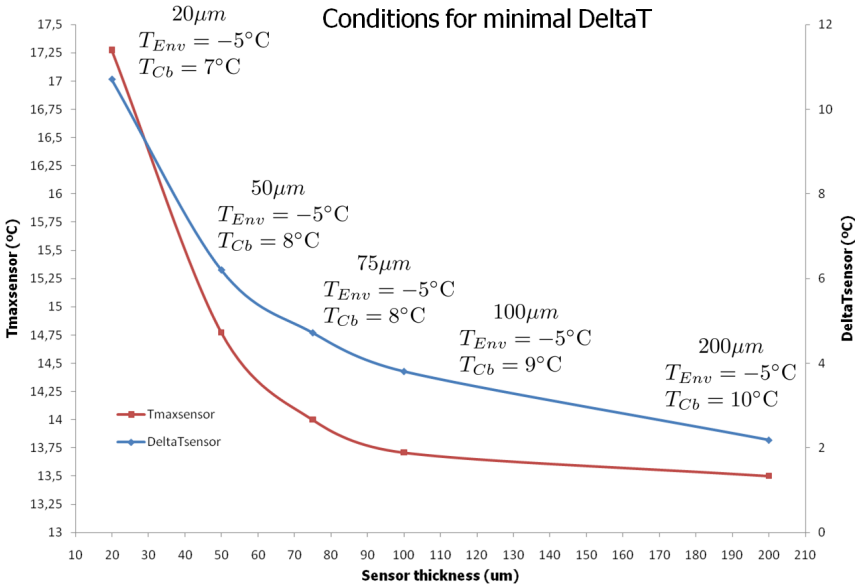

Figure 6.32: *Gradient and maximum temperature achieved in the ladder as a function of the sensor thickness. The environment was fix at a temperature of -5 °C and the cooling block was varied to satisfy the relation of minimal gradient and a maximum temperature around ∼15 °C.*

of the system in terms of signal to noise ratio after irradiation. The temperature distribution along the ladder while applying these environmental condition can be seen in Fig. 6.33. Under these conditions, a quite uniform gradient was found (ΔT=4.7 °C) while the maximum temperature in the ladder was ∼15 °C, within the required limits.

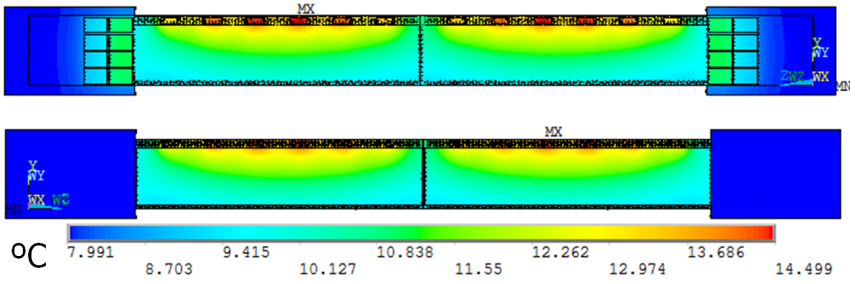

Figure 6.33: *Temperature distribution along the ladder (front and back sides in the upper and lower figures, respectively) while applying $T_{Environment} = -5$ °C and $T_{CoolingBlock} = 8$ °C, for a sensor thickness of 75 μm.*

6.7 Thermal enclosure

Analyzing the working conditions found in the previous section, the first observation is that those temperatures are below the dew point in the Belle experimental hall (estimated in ∼15 °C) and condensation will appear if the detector is operated in such conditions. To solve this problem, the inner detectors (PXD and SVD), that have to work at low temperatures must be isolated from the CDC inside a thermal enclosure (TE) structure. Although the thermal isolation would be the main task of this structure, the thermal enclosure would serve also to give mechanical protection to the detector while is assembled, can act as a moisture barrier and can be flushed with dry nitrogen to avoid condensation inside. The thermal enclosure can also act as a Faraday cage if covered with a metal layer and used as a common grounding point for the inner detectors (PXD and SVD). Nevertheless, apart from its great advantages, the thermal enclosure will be inserted in a crucial part in the detector tracking, between the last SVD layer and the CDC, so the minimum material budget is an issue.

As many groups in the collaboration have experience in the construction of the ATLAS detector at CERN (IFIC is one of them), the first solution was ATLAS-based, using the materials included in the OTE (Outer Thermal Enclosure) of the end-cap region of that detector [67]. The ATLAS thermal enclosure (Fig. 6.34 (*a*)) has a foam core, made of 8 mm of AIREX R82 foam [68]. This material is also used in aerospace science, and has very good isolating properties while being successfully tested from -194 °C to 160 °C. It presents a low moisture absorption and while being very light (with a low density of 60 kg/m^3), is thermoformable (shaped parts can be produced starting with a foam sheet and applying heat and pressure) and the thermal conductivity is very low (k=0.036 $W/m \cdot K$). In the ATLAS original design, the AIREX inner wall was covered with aluminised kapton (1 μm of Al and 24 μm of kapton) foil to reduce the radiative heat transfer through the surface, while the outer one was covered with a copper kapton foil (18 μm of Cu and 25 μm of kapton) that acts as an electrical shielding. On top of the copper kapton foil, on the outer surface, a heater was attached to keep the outer surface at a constant temperature. All layers were glued using 100 μm of Araldite 2011 epoxy [69], a radiation hard glue approved by the ATLAS Collaboration. Unfortunately, such structure can not be directly incorporated to the Belle-II thermal enclosure because the excess of material budget, thus a minimal version was prepared, getting rid of the heater and replacing the copper kapton by a second layer of aluminised kapton foil (called *Mini-Airex*) (Fig. 6.34 (*b*)). The material budget was then dramatically decreased in almost a 40% (Table 6.2) and also the complexity by not having to apply currents and voltage regulation to the heater.

To test the performance of the Mini-Airex configuration, a box was done using that configuration. While blowing cold air inside the box, the temperature through the upper box wall was measured by means of two Pt100 resistors. Fig. 6.35, shows the temperature in the outer surface as a function of the temperature inside. Although in the simulation the proposed working point involved an air temperature of -5 °C, for security reasons, a factor 2 can be included, so if an inner temperature

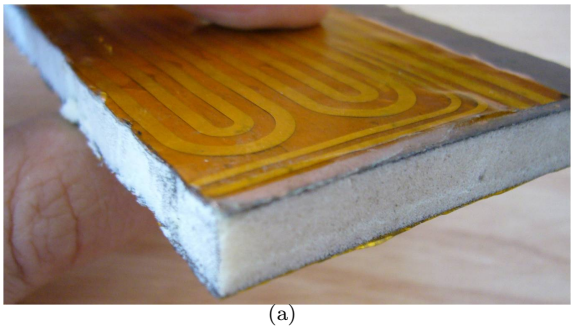

(a)

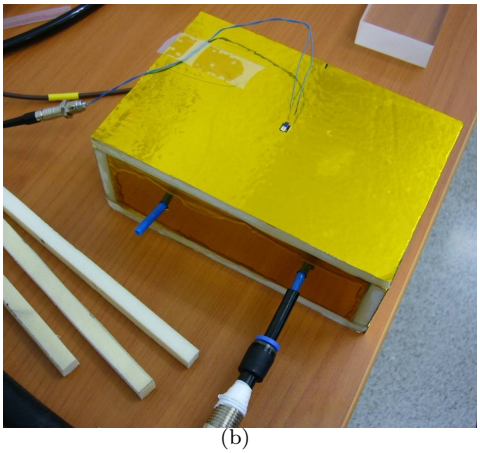

(b)

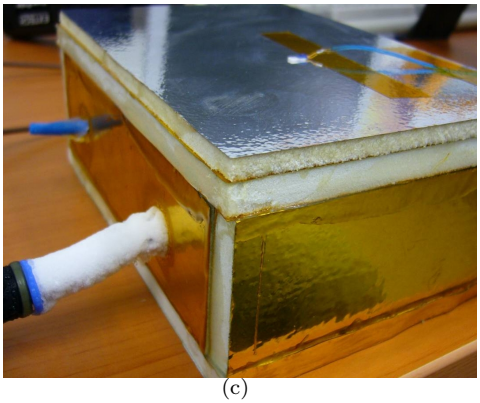

(c)

Figure 6.34: *Based on the ATLAS OTE (Outer Thermal Enclosure) (a), two new solutions were developed: The Mini-Airex (b), with much less material, and the Multilayer option, a simpler option although with the same amount of material budget.*

	ATLAS OTE	Mini-Airex	Multilayer
Kapton (%X_0)	0.017	0.017	0.025
Airex (%X_0)	0.2	0.2	0.34
Al (%X_0)	0.0002	0.00045	0.00067
Cu (%X_0)	0.13	0	0
Araldite (%X_0)	0.05	0.05	0.075
Total (%X_0)	0.4	0.27	0.4

Table 6.2: *Breakdown of the material budget contribution for the different TE configurations.*

of -10 °C is assumed, a temperature outside of 18.5 °C can be expected from the curve fit. Although an impressive temperature reduction was achieved, the fact that the CDC has to work at a temperature of 20 °C, forced to look for another better solution.

A *Multilayer* structure was then implemented (Fig. 6.34 (*c*)), just by the addition of a thinner (5 mm) Airex layer on top of the current Mini-Airex option. The thin layer was also covered with aluminised kapton on the outer surface, glued with Araldite 2011. By the addition of a second Airex layer in the Multilayer option, the high material budget of the ATLAS OTE was again recovered but, in this case, even with the same amount of material, the system is simpler because of the absence of the heater. The performance of the system, was tested as in the Mini-Airex case, attaching a third Pt100 sensor outside of the new thin layer. The temperatures obtained in the middle point (blue diamonds) as well as on the outer wall (red squares) are presented as a function of the inner temperature in Fig. 6.36.

In this case, assuming an inner temperature of -10 °C, from the linear fit can be calculated that the expected temperature outside will be 19.7 °C, pretty close to the requirements. Nevertheless, a more interesting feature was found by measuring the temperature in between the two Airex layers (Fig. 6.37).

In the Multilayer option, the middle point was at 9.2 °C (having -10 °C inside the box) where the temperature was 18.5 °C in the Mini-Airex choice. Considering that the only difference in that point was the addition of the second Airex layer, its clear that the isolation comes not really from the Airex (that certainly helps), but from the infinite warm air outside the system. Assuming this statement, the strategy to follow should be either to heat the outer surface of a thin Airex layer (instead of trying to insulate it with a thick one) or either to flush warm air in between the TE and the CDC.

Nevertheless, this assumptions could not be close to reality. Because of the most temperature sensitive part of the SVD (the new APV25 readout chips) will

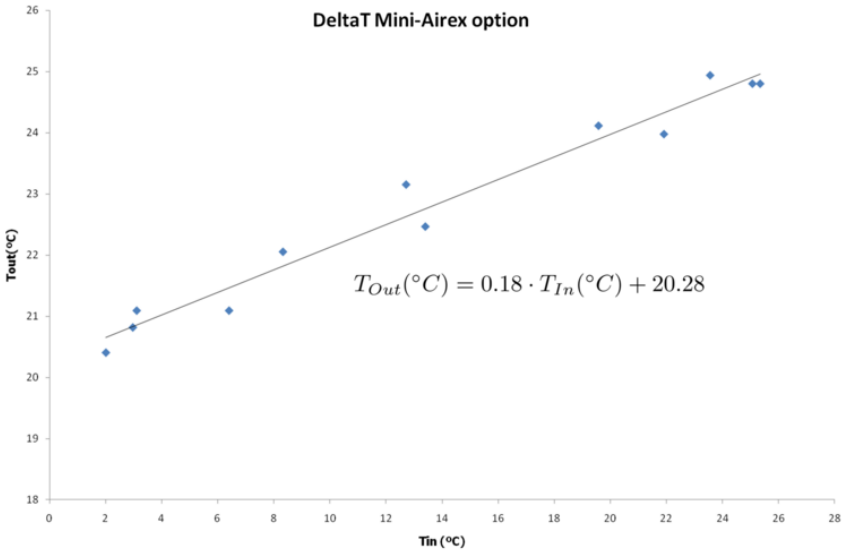

Figure 6.35: *The temperature in the outer wall of the Mini-Airex box as a function of the temperature inside. Both temperatures were measured using Pt100 sensors.*

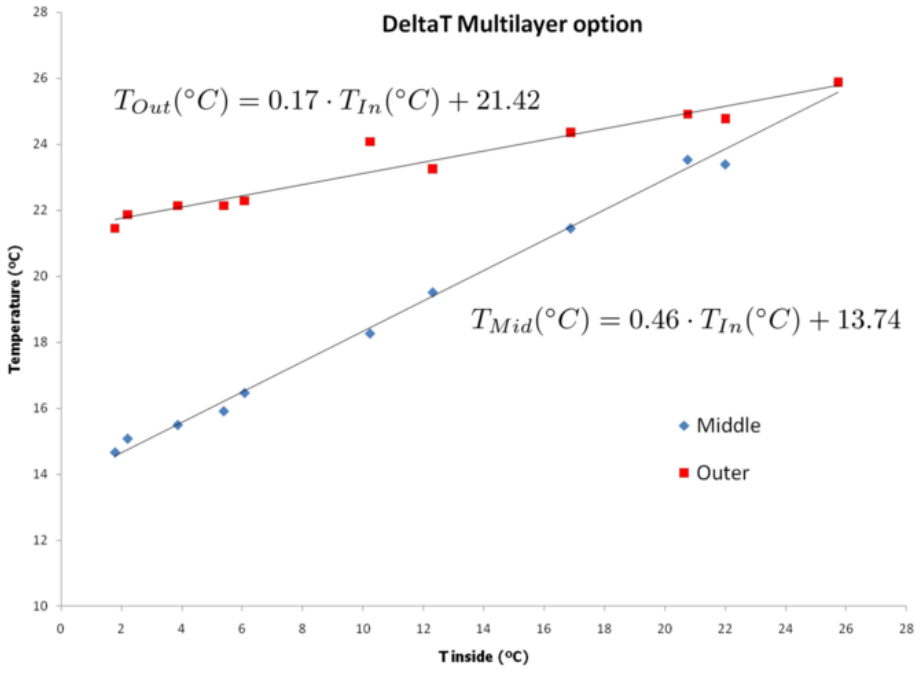

Figure 6.36: *The temperature in the middle (blue diamonds) and outer wall (red squares) of the Multilayer box as a function of the temperature inside.*

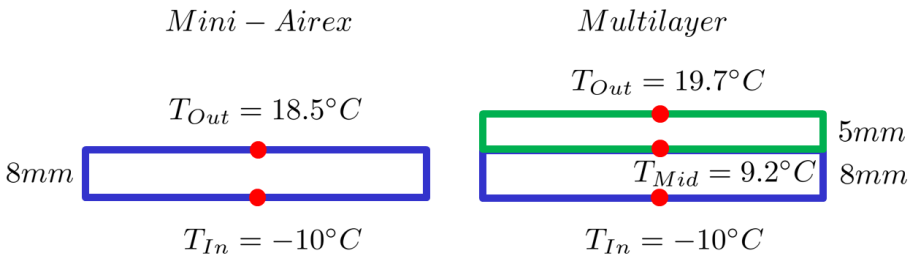

Figure 6.37: *Comparison between the results obtained with both options: Mini-Airex and Multilayer. Comparing the temperatures on the same points in both schemes, it is clear that the isolation comes not really from the Airex layer (that certainly helps), but from the infinite volume of warm air outside the TE.*

be cooled using CO_2, for cooling the sensor just a very small air flow at a moderate temperature is assumed that will be needed. In this cooling option, the cool air (at -10 °C) will enter the volume through dedicated channels in the PXD end-flanges and the SVD will live the the PXD *leaks*. In this case, the air will be warmer and warmer as it expands from in between the PXD ladders and such low temperature will never be achieved in the inner wall of the thermal enclosure, although this has to be demonstrated using a thermal mockup. A close to reality thermal solution could involve a carbon fiber shell to combine forward and backward support with a thin Airex layer and aluminised kapton attached to the cylinder.

6.8 Future plans

To check the validity of these simulations, a thermal mockup, recreating the full PXD detector, is being built at IFIC. This mockup will be contained inside a IR transparent cylinder (to be able to take images with the thermal camera) reproducing the volume defined by the PXD stand-alone or the PXD and SVD together (it is not yet decided whether the PXD will be cooled independently of the SVD or not). The support structures (Fig. 6.38) have the same design as the ones that will be used in the final detector but, for simplicity, will be chilled in a first stage just using mono-phase cooling (coolant from a commercial chiller). The cooling blocks will be cooled by circulating CO_2 through small capillaries inside the massive structures. These inner structures can not be produced using conventional machinery, so the production was done using 3D laser sintering. Because of the high pressures that implies working with CO_2, the material chosen is stainless steel.

These support structures will be attached to a beam pipe, made in aluminum. The beam pipe can be operated at the expected temperature in the final experiment (15 °C) and will be also cooled using the coolant from a chiller. This fact has to be taken into account because of the PXD will be operated at lower temperatures so, specially the inner layer, will receive heat in the shape of radiation.

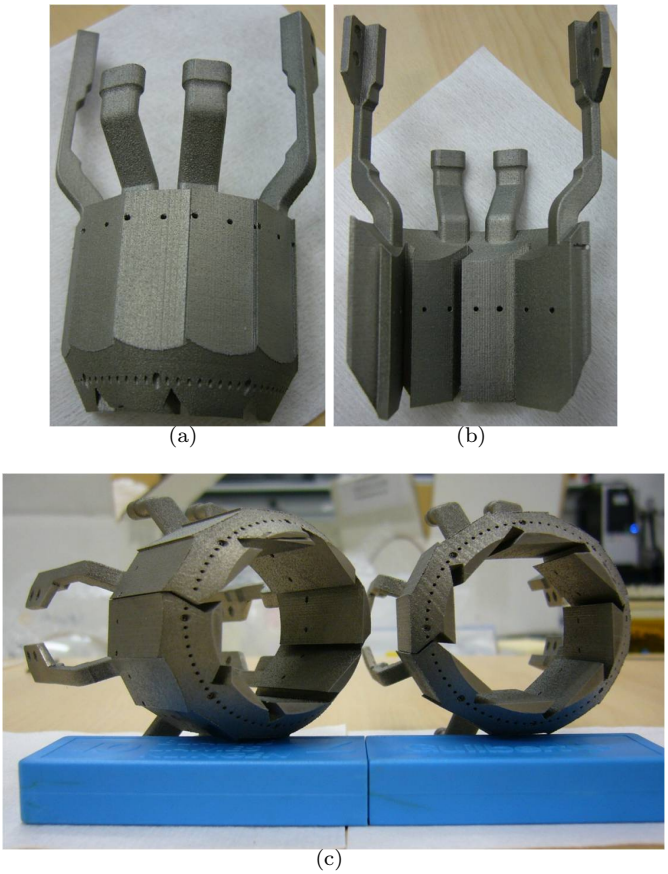

Figure 6.38: *The end of the staves will be cooled using massive structures outside the acceptance. CO_2 at a very low temperature will circulate through capillaries inside these structures. These complex cooling blocks can not be fabricated using conventional machinery so the pieces were fabricated in 3D laser sintering in external companies. The material chosen was stainless steel to cope with the high pressures that will appear in the CO_2 operation.*

The final Belle-II sensors are not available yet in the collaboration so, these structures will incorporate three mechanical ladders with integrated resistors on them (Fig 6.39), simulating the different elements in the detector (sensor, DCDs and Switchers). The rest of the detector will be populated with dummy ladders made in polycarbonate.

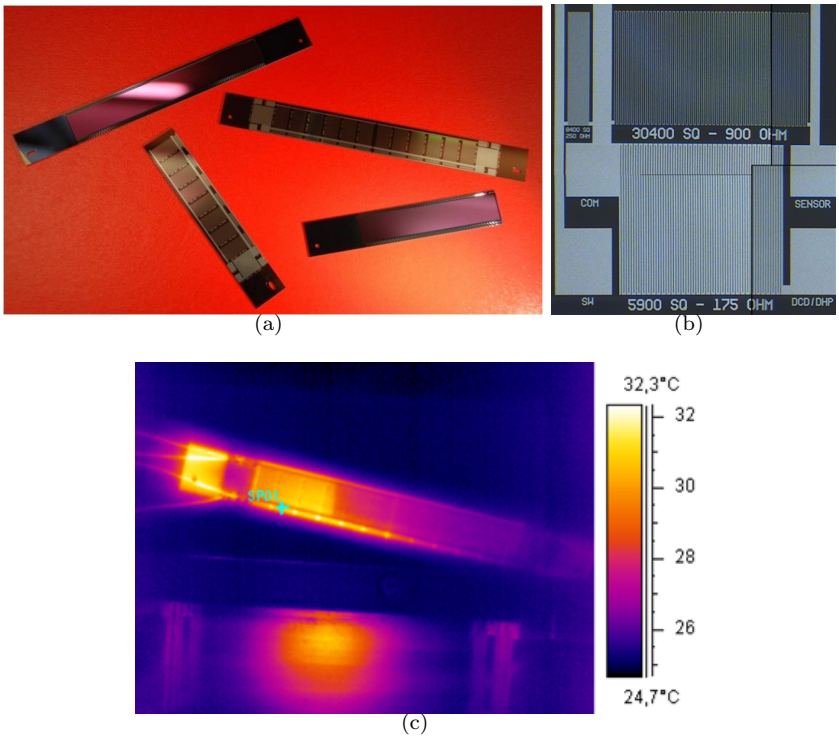

(a) (b) (c)

Figure 6.39: *The cooling blocks will be populated using mechanical samples (a) equipped with integrated resistors ((b) detailed view) to dissipate power on the different areas of the detector. (c) Thermal image of one of the samples showing the effect of having four powered Switchers in the lateral balcony.*

In Fig. 6.40, the close to final assembly is shown. This mechanical mockup will reveal if th chosen cooling concept is appropriate and will also serve to fine tune the thermal simulations.

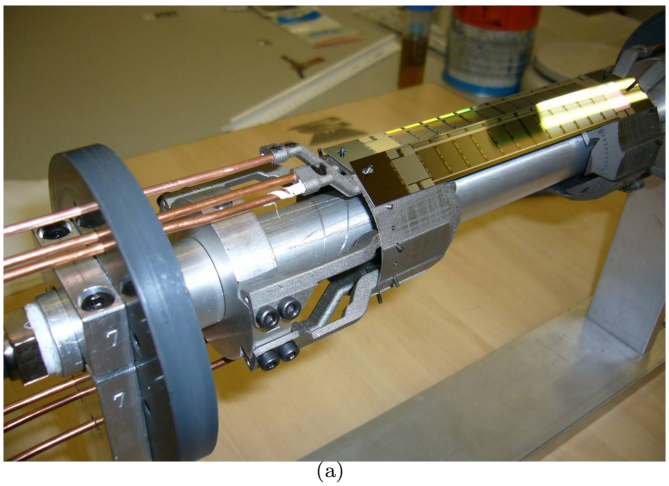

(a)

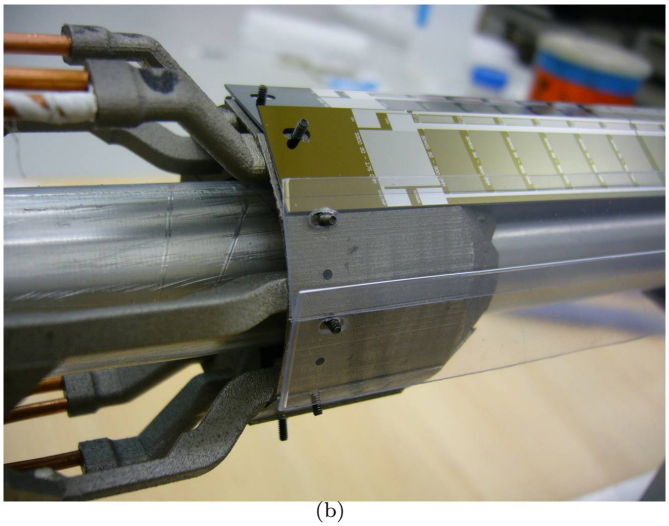

(b)

Figure 6.40: *The cooling mockup, that will reveal if the right cooling strategy was selected, is almost finished.*

Conclusions

High Energy Physics is entering in the most important phase since the Copernican revolution. The Standard Model, the most successful model ever created by the Human Kind enters into its crutial tests: The Large Hadron Collider will explore the energy region where the Higgs boson (if it exists) must appear and the mechanism by which the particles acquiere mass will be revealed.

The LHC will reach energies ever dreamt by the physics community and new machines, like ILC or SuperKEKB will complement the discoveries that the Large Hadron Collider will clearly make. The ILC will break the energy frontier of the lepton colliders and detectors like Belle-II in Japan will explore the new physics (breaking the luminosity frontier) using large amounts of data. The DEPFET technology, given its unique properties, is one of the principal candidates to cope with the challenging requirements imposed over the Vertex Detectors of the ILC detector concepts: high spatial resolution, low power consumption or very low material budget are intrinsic characteristics of this technology. In fact, the DEPFET technology is already the baseline to make the pixel detector of the Belle-II experiment in the new Super B Factory in KEK (Japan). Although the required spatial resolution is less challenging in this project rather than in the ILC, the material budget should be kept as reduced as possible preventing the use of active cooling in the sensitive volume of the tracker and vertex detectors. Given that SuperKEKB is a *DC* machine, we can not profit from any power cycle as ILC does and, air cooling should be envisaged.

The DEPFET technology was invented in the 80's. Detectors with high signal to noise ratio were extensively tested during several beam tests developed by the collaboration. A dedicated technique allows to build very thin sensors ($\sim 50\mu m$) embebed in a silicon rim, avoidind the necessity of any extra support material. Two different generations of sensors, with three clear mechanisms were tested, achieving an elevated charge collection together with a complete and fast clear. Although the sensor optimization depends on many parameters, an optimal working point can be identified, using radioactive sources and lasers in the laboratory. Complementary beam tests have shown the great performance of the sensors, with an intrinsic resolution of $\sim 1\mu m$. To extract the intrinsic resolution, a DEPFET telescope had to be built, not having in the market another device with such a high precission. The data analysis is done using standard codes developed by the ILC community. Finally, a cooling solution has been developed for the PXD detector of the Belle-II

experiment. This solution takes advantage of the special features of the detector and relies on massive structures outside the acceptance to cool the end of the staves while the center of the sensor is chilled using cold air. The cooling solution has been developed with no aditional material inside the acceptance.

Conclusiones

La Física de Partículas está apunto de entrar en su fase más crucial desde la revolución copernicana. El Modelo Estándard, la teoría más exitosa jamás creada por la humanidad, entra en un período crucial donde será finalmente contrastada: el Gran Colisionador Hadrónico (LHC) explorará la región de energía dónde se predice la existencia del bosón de Higgs (si realmente existe) y de esta manera, se revelará el mecanismo por el cual las partículas adquieren su masa. El LHC alcanzará energías jamás soñadas por la comunidad científica y nuevas máquinas, como el ILC o SuperKEKB, se encargarán de complementar los descubrimientos que, sin duda, realizará el Gran Colisionador Hadrónico. El ILC será una máquina que romperá la frontera de energía alcanzada por los anteriores colisionadores leptónicos, y detectores como Belle-II en Japón, estudiarán la nueva física utilizando grandes cantidades de datos, rompiendo la barrera de la alta luminosidad.

La tecnología DEPFET, debido a sus únicas características, es uno de los principales candidatos para ser usada en los Detectores de Vértices de los conceptos de detectores del ILC: gran resolución espacial, limitado consumo de potencia o escaso material, son propiedades intrínsecas de esta tecnología. De hecho, la tecnología DEPFET será utilizada para fabricar el detector de píxeles del experimento Belle-II en la nueva Súper Factoría de B en KEK (Japón). Aunque la resolución espacial exigida en este caso es menor que en el ILC, el material ha de ser reducido al mínimo y el consumo de potencia debe ser tan bajo que permita la refrigeración del sensor utilizando solamente aire en la zona activa de los detectores de vertices y trazas. Dado que SuperKEKB es una máquina *DC*, este detector no puede utilizar la estrategia seguida en el ILC de apagar el detector cuando no existen colisiones y, en este caso, la refrigeración por aire ha de ser cuidadosamente diseñada.

La tecnologa DEPFET se inventó en los años 80. En los últimos años se han producido sensores con una gran relación señal ruído que han sido sometidos a pruebas en haz, obteniendo resultados muy satisfactorios. Una técnica desarrollada especialmente para este tipo de detectores, permite crear sensores muy finos ($\sim 50\mu m$) directamente integrados en un bastidor de silicio, eliminando la necesidad de añadir material extra para su soporte.

Dos generaciones de sensores, con tres mecanismos diferentes de *borrado* han sido caracterizados, consiguiendo una gran recolección de carga conjuntamente

con un rápido *borrado*. Aunque la optimización del sensor depende de múltiples parámetros, se puede encontrar un punto óptimo de trabajo para el mismo, utilizando fuentes radioactivas y láseres en el laboratorio.

De una forma complementaria a los test en laboratorio, se han realizado pruebas en haz, que han demostrado unas excelentes prestaciones de los sensores, alcanzando una resolución intrínsica de $\sim 1\ \mu m$. Para poder conocer la resolución intrínsica, se ha construido tambiń un telescopio basado en la tecnología DEPFET, no habiendo en el mercado un dispositivo con una precisión tan elevada. El análisis de los datos se realiza mediante un código estándard desarrollado por la comunidad del ILC.

Finalmente, se ha desarrollado un mecanismo de refrigeración del detector de píxeles del experimento Belle-II. Esta solución utiliza las características especiales de dicho detector para situar masivas estructuras de refrigeración fuera de la aceptancia del experimento mientras que el centro del sensor es refrigerado mediante aire frío. Dicha propuesta ha sido desarrollada sin introducir ningún material extra dentro de la aceptancia del detector.

Bibliography

[1] D. Speiser, "Newton's Principia,"

[2] S. L. Glashow, "Partial Symmetries Of Weak Interactions," Nucl. Phys. **22** (1961) 579.

[3] S. Weinberg, "A Model Of Leptons," Phys. Rev. Lett. **19** (1967) 1264.

[4] A. Salam, "Weak And Electromagnetic Interactions," *In the Proceedings of 8th Nobel Symposium, Lerum, Sweden, 19-25 May 1968, pp 367-377.*

[5] P. W. Higgs, "BROKEN SYMMETRIES AND THE MASSES OF GAUGE BOSONS," Phys. Rev. Lett. **13** (1964) 508.

[6] L. Evans and P. Bryant, "Lhc Machine," JINST **3** (2008) S08001.

[7] *The Large Hadron Collider Technical Design Report.* CERN/AC/95-05, 1995.

[8] G. Guignard, "CLIC: A 3-TeV linear collider study," in *Proc. of the APS/DPF/DPB Summer Study on the Future of Particle Physics (Snowmass 2001)* ed. N. Graf, *In the Proceedings of APS / DPF / DPB Summer Study on the Future of Particle Physics (Snowmass 2001), Snowmass, Colorado, 30 Jun - 21 Jul 2001, pp E3050.*

[9] J. Brau *et al.*, "International Linear Collider reference design report. Vol 3: Accelerator."

[10] S. Hashimoto *et al.*, "Letter of intent for KEK Super B Factory,"

[11] J. Brau *et al.*, "International Linear Collider reference design report. Vol 2: Physics at the ILC."

[12] P. Fayet and S. Ferrara, "Supersymmetry," Phys. Rept. **32** (1977) 249.

[13] F. Richard, "Scenarios for ILC in 2010," arXiv:0707.3723 [hep-ph].

[14] T. Aushev *et al.*, "Physics at Super B Factory," arXiv:1002.5012 [hep-ex].

[15] N. Cabibbo, "Unitary Symmetry and Leptonic Decays," Phys. Rev. Lett. **10** (1963) 531.

[16] M. Kobayashi and T. Maskawa, "CP Violation In The Renormalizable Theory Of Weak Interaction," Prog. Theor. Phys. **49** (1973) 652.

[17] Y. Miyazaki [Belle Collaboration], "Search for a lepton flavor violation in tau decays at Belle experiment," PoS E **PS-HEP2009** (2009) 263.

[18] ATLAS Collaboration. *ATLAS Detector and Physics Performance Technical Design Report*. CERN/LHCC/99-14, 99-15, 1999.

[19] CMS Collaboration. *The Compact Muon Solenoid Technical Proposal*. CERN/LHCC/94-38, 1994.

[20] LHCb Collaboration. LHCb Technical Proposal. CERN/LHCC/98-4, 1998.

[21] ALICE Collaboration. *ALICE Technical Proposal*. CERN/LHCC/95-71, 1995.

[22] S. Bethke, "Experimental tests of asymptotic freedom," Prog. Part. Nucl. Phys. **58** (2007) 351 [arXiv:hep-ex/0606035].

[23] H. Schopper, "LEP: The lord of the collider rings at CERN 1980-2000: The making, operation and legacy of the world's largest scientific instrument," *Berlin, Germany: Springer (2009) 211 p*

[24] A. Abashian *et al.*, "The Belle Detector," Nucl. Instrum. Meth. A **479** (2002) 117.

[25] D. Boutigny *et al.* [BABAR Collaboration], "BaBar technical design report,"

[26] R. Blair *et al.* [CDF-II Collaboration], "The CDF-II detector: Technical design report,"

[27] M. Bona *et al.*, "SuperB: A High-Luminosity Asymmetric e^+e^- Super Flavor Factory. Conceptual Design Report," arXiv:0709.0451 [hep-ex].

[28] J. Treis *et al.*, "DEPMOSFET Active Pixel Sensor Prototypes for the XEUS Wide Field Imager," IEEE Trans. Nucl. Sci. **52** (2005) 1083.

[29] J. Ulrici *et al.*, "Imaging performance of a DEPFET pixel Bioscope system in Tritium autoradiography," Nucl. Instrum. Meth. A **547** (2005) 424.

[30] *http://ific.uv.es/ vos/ilc/ilcFastForward/ilcFastForward.html*

[31] K. Fujii, D. J. Miller and A. Soni, "Linear collider physics in the new millennium," *Singapore, Singapore: World Scientific (2005) 499 p*

[32] A. Vogel. *Beam-induced backgrounds in detectors at the ILC*. DESY-THESIS-2008-036.

[33] T. Abe *et al.* [ILD Concept Group - Linear Collider Collaboration], "The International Large Detector: Letter of Intent," arXiv:1006.3396 [hep-ex].

[34] H. Aihara *et al.*, "SiD Letter of Intent," arXiv:0911.0006 [physics.ins-det].

[35] M. A. Thomson, "Particle Flow Calorimetry and the PandoraPFA Algorithm," Nucl. Instrum. Meth. A **611** (2009) 25 [arXiv:0907.3577 [physics.ins-det]].

[36] T. Abe *et al.*, "Belle II Technical Design Report," arXiv:1011.0352 [physics.ins-det].

[37] C. J. S. Damerell, "CCD-based vertex detectors," Nucl. Instrum. Meth. A **541** (2005) 178.

[38] R. Turchetta *et al.*, "A monolithic active pixel sensor for charged particle tracking and imaging using standard VLSI CMOS technology," Nucl. Instrum. Meth. A **458** (2001) 677.

[39] J. Kemmer and G. Lutz, "New Detector Concepts," Nucl. Instrum. Meth. A **253** (1987) 365.

[40] E. Gatti and P. Rehak, "Semiconductor drift chamber - an application of a novel charge transport scheme," Nucl. Instrum. Meth. A **225** (1984) 608.

[41] H. G. Moser *et al.*, "DEPFET active pixel sensors," PoS **VERTEX2007** (2007) 022.

[42] C. Sandow *et al.*, "Clear-performance of linear DEPFET devices," Nucl. Instrum. Meth. A **568** (2006) 176.

[43] R. Kohrs. *Development and Charazterization of a DEPFET Pixel Prototype System for the ILC Vertex Detector*. PhD thesis, Univertität Bonn, 2008.

[44] I. Peric. *Design and Realization of Integrated Circuits for the Readout of Pixel Sensors in High-Energy Physics and Biomedical Imaging*. PhD thesis, Univertität Bonn, 2004.

[45] M. Trimpl and P. Fischer, "CURO: A current based readout ASIC for a DEPFET pixel based vertex detector at the ILC," *Prepared for 11th Workshop on Electronics for LHC and Future Experiments (LECC 2005), Heidelberg, Germany, 12-16 September 2005*

[46] H. G. Moser, L. Andricek, R. H. Richter and G. Liemann, "Thinned silicon detectors," PoS **VERTEX2007** (2007) 013.

[47] C. Kreidl, C. Kreidl and I. Peric, "Steering and readout chips for DEPFET sensor matrices," *In *Prague 2007, Electronics for particle physics* 28*

[48] H. Kruger [DEPFET Collaboration], "Front-end electronics for DEPFET pixel detectors at SuperBelle (BELLE II)," Nucl. Instrum. Meth. A **617** (2010) 337.

[49] D. Cussans. *Description of the JRA1 Trigger Logic Unit (TLU)*. EUDET-Memo-2007-02.

[50] A. Bulgheroni *et al.*. *EUTelescope: tracking software*. EUDET-Memo-2007-20.

[51] `http://www.eudet.org`

[52] F. Gaede, "Marlin and LCCD: Software tools for the ILC," Nucl. Instrum. Meth. A **559** (2006) 177.

[53] F. Gaede, T. Behnke, N. Graf and T. Johnson, "LCIO: A persistency framework for linear collider simulation studies," *In the Proceedings of 2003 Conference for Computing in High-Energy and Nuclear Physics (CHEP 03), La Jolla, California, 24-28 Mar 2003, pp TUKT001* [arXiv:physics/0306114].

[54] `http://ilcsoft.desy.de/gear/current/doc/html/index.html`

[55] `http://ilcsoft.desy.de/portal/software_packages/lccd/`

[56] `http://ilcsoft.desy.de/portal/software_packages/raida/`

[57] V. Blobel, "Software alignment for tracking detectors," Nucl. Instrum. Meth. A **566** (2006) 5.

[58] R. Turchetta, "Spatial Resolution Of Silicon Microstrip Detectors," Nucl. Instrum. Meth. A **335** (1993) 44.

[59] L. Andricek *et al.*, "Spatial resolution analysis of micron resolution silicon pixel detectors based on beam and laser tests," Nucl. Instrum. Meth. A **604** (2009) 385.

[60] Ch. Geisler. *DEPFET for ILC and Belle*. Diploma thesis, II. Physikalisches Institut Univertität Götingen, 2010.

[61] S. Hancock, F. James, J. Movchet, P. G. Rancoita and L. Van Rossum, "Energy Loss And Energy Straggling Of Protons And Pions In The Momentum Range 0.7-Gev/C To 115-Gev/C," Phys. Rev. A **28** (1983) 615.

[62] C. Marinas and M. Vos, "The Belle-II DEPFET Pixel Detector: A step forward in vertexing in the SuperKEKB Flavour Factory," Nucl. Instrum. Meth. A (2011), doi:10.1016/j.nima.2010.12.116.

[63] FLIR Thermacam SC500

[64] C. A. Heusch, H. G. Moser and A. Kholodenko, "Direct measurements of the thermal conductivity of various pyrolytic graphite samples (PG, TPG) used as thermal dissipation agents in detector applications," Nucl. Instrum. Meth. A **480** (2002) 463.

[65] Frank P. Incropera *et al.*, "Fundamentals of heat and mass transfer," ISBN-13: *978-0-471-45728-2.

[66] Th. Weiler, O. Brovchenko, S. Heindl and H. J. Simonis. *Belle II PXD Thermal Studies in Karlsruhe*. In Belle-II PXD/ DEPFET Meeting, 2010.

[67] A. Abdesselam *et al.*, "The integration and engineering of the ATLAS SemiConductor Tracker barrel," JINST **3** (2008) P10006.

[68] http://www.corematerials.3acomposites.com/airex-r82-us.html

[69] A. G. Kholodenko, H. G. Moser and V. N. Riadovikov, "The Thermal and Mechanical Properties of Glues for the ATLAS SCT ModuleAssembly," ATL-INDET-2000-007